

# Persistence Spheres: a Bi-continuous Linear Representation of Measures for Partial Optimal Transport

Matteo Pegoraro\*

March 17, 2026

## Abstract

We improve and extend persistence spheres, introduced in Pegoraro (2026). Persistence spheres map an integrable measure  $\mu$  on the upper half-plane, including persistence diagrams (PDs) as counting measures, to a function  $S(\mu) \in C(\mathbb{S}^2)$ , and the map is stable with respect to 1-Wasserstein partial transport distance  $\text{POT}_1$ . Moreover, to the best of our knowledge, persistence spheres are the first explicit representation used in topological machine learning for which continuity of the inverse on the image is established at every compactly supported target. Recent bounded-cardinality bi-Lipschitz embedding results in partial transport spaces, despite being powerful, are not given by the kind of explicit summary map considered here. Our construction is rooted in convex geometry: for positive measures, the defining ReLU integral is the support function of the lift zonoid. Building on Pegoraro (2026), we refine the definition to better match the  $\text{POT}_1$  deletion mechanism, encoding partial transport via a signed diagonal augmentation. In particular, for integrable  $\mu$ , the uniform norm between  $S(0)$  and  $S(\mu)$  depends only on the persistence of  $\mu$ , without any need of ad-hoc re-weightings, reflecting optimal transport to the diagonal at persistence cost. This yields a parameter-free representation at the level of measures (up to numerical discretization), while accommodating future extensions where  $\mu$  is a smoothed measure derived from PDs (e.g., persistence intensity functions (Wu et al., 2024)). Across clustering, regression, and classification tasks involving functional data, time series, graphs, meshes, and point clouds, the updated persistence spheres are competitive and often improve upon persistence images, persistence landscapes, persistence splines, and sliced Wasserstein kernel baselines.

**Keywords:** lift zonoid, persistence diagrams, vectorization, topological machine learning

## 1. Introduction

Topological Data Analysis (TDA) provides geometric descriptors designed to capture qualitative structure in data while being robust to noise and, in many contexts, insensitive to parametrization. Its flagship tool, *persistent homology*, tracks homological features across a scale parameter, recording when connected components, loops, and higher-dimensional cavities are created and later filled in. The resulting summaries are typically encoded as *persistence diagrams* (PDs) or barcodes, which have become standard objects for exploratory analysis and for building topologically informed learning pipelines (Edelsbrunner and Harer, 2010; Oudot, 2015).

**Distances and the non-linear geometry of diagrams.** From a statistical viewpoint, PDs are most naturally compared by Wasserstein-type distances defined through *partial optimal transport* (POT), where unmatched mass is optimally sent to the diagonal (Divol

---

\*. Institute of Computing, Faculty of Informatics, Università della Svizzera Italiana

and Lacombe, 2021). These metrics are central to stability results, but they endow the space of diagrams with a strongly non-linear geometry. As a consequence, even elementary operations, such as averaging, regression, or principal component analysis, do not admit straightforward analogues. For instance, averages can be formulated as Wasserstein barycenters (Mileyko et al., 2011), which can be costly to approximate and may be non-unique, complicating both computation and interpretation.

**Topological machine learning via vectorizations.** A large body of work therefore focuses on mapping PDs into linear spaces where classical statistical tools apply. This line of research underpins *topological machine learning* (Papamarkou et al., 2024), where vectorized topological features and differentiable topological objectives are used in predictive tasks and representation learning (Moor et al., 2020; Wayland et al., 2024). Existing approaches include explicit embeddings and feature maps, as well as kernel methods (Reininghaus et al., 2015; Kusano et al., 2018; Carriere et al., 2017). Among explicit embeddings, one finds constructions based on descriptive statistics (Asaad et al., 2022), algebraic or tropical coordinates (Kališnik, 2019; Monod et al., 2019; Di Fabio and Ferri, 2015), and functional representations such as landscapes, images, and related summaries (Bubenik, 2015; Adams et al., 2017; Biscio and Møller, 2019; Dong et al., 2024; Gotovac Dogaš and Mandarić, 2025), alongside other geometric encodings (Mitra and Virk, 2024). To the best of our knowledge, however, none of these explicit vectorizations comes with some continuity statement for the inverse map. By contrast, for kernel-induced Hilbert embeddings, the sliced Wasserstein construction yields such a bi-continuity statement on bounded-cardinality subclasses, as we recall below.

At the same time, strong *impossibility* results show that one cannot hope for a globally faithful linearization of the Wasserstein geometry of PDs. Following the synthesis in Mitra and Virk (2024), the picture can be summarized as follows: (i) the space of diagrams with finitely many points does not admit a bi-Lipschitz embedding into any Hilbert space (Mitra and Virk, 2021); (ii) even restricting to at most  $n$  points, no bi-Lipschitz embedding into any *finite-dimensional* Euclidean space exists (Carrière and Bauer, 2019); (iii) on such bounded-cardinality classes, a bi-continuous embedding into a Hilbert space can be achieved via the sliced Wasserstein construction (Carriere et al., 2017); (iv) on at most  $n$  points one can also obtain coarse embeddings into Hilbert spaces (Mitra and Virk, 2021, 2024); and (v) more recently, bi-Lipschitz embeddings into a Hilbert space have been obtained for diagrams with at most  $n$  points (Bate and Garcia Pulido, 2024). Notably, among these results, Carriere et al. (2017); Mitra and Virk (2024) provide explicit geometric constructions.

More precisely, Carriere et al. (2017) prove that the sliced Wasserstein distance itself is bi-Lipschitz equivalent to  $\text{POT}_1$  under a uniform bound on the number of points, while for the RKHS distance induced by the sliced Wasserstein kernel the comparison with  $\text{POT}_1$  is given through continuous control functions on the same bounded-cardinality classes.

**Persistence spheres and bi-continuity (Pegoraro, 2026).** In Pegoraro (2026) we introduced *persistence spheres*, a functional representation sending a persistence diagram to a real-valued function on  $\mathbb{S}^2$ , with two complementary guarantees: Lipschitz stability with respect to  $\text{POT}_1$  and continuity of the inverse on the image. In this sense, persistence spheres provide a form of geometric faithfulness which, to the best of our knowledge, is not available for other explicit representations of persistence diagrams currently used in topological machine learning. The construction is rooted in the lift-zonoid representation

of a measure: for a positive integrable measure  $\mu$ , the map

$$v \mapsto \int \text{ReLU}(\langle v, (1, p) \rangle) d\mu(p)$$

is the support function of the lift zonoid  $Z_\mu$  (Koshevoy and Mosler, 1998; Hendrych and Nagy, 2022).

**Comparison with Pegoraro (2026).** Relative to Pegoraro (2026), we strengthen the framework in four directions:

1. **POT coherence without re-weighting.** The refined definition matches the  $\text{POT}_1$  geometry of deletions: the uniform norm between  $S(0)$  and  $S(\mu)$  depends only on the persistence of  $\mu$ , reflecting that unmatched mass is optimally sent to the diagonal at cost equal to its persistence (see Remark 1). As a consequence, the representation can be defined directly at the level of measures, without introducing reweighting schemes or tuning parameters (beyond numerical choices such as the discretization grid used to evaluate the functions).
2. **A measure-theoretic formulation.** We work with integrable measures on the upper half-plane endowed with  $\text{POT}_1$  (Divol and Lacombe, 2021), covering classical PDs (as discrete measures) and extending seamlessly to smooth summaries such as *persistence intensity functions* (Wu et al., 2024). This unified setting is geared toward statistical modeling of persistence objects, allowing one to treat discrete diagrams and smoothed/estimated representations within a single geometry.
3. **A comparative analysis of topological summaries.** Beyond introducing the revised persistence-sphere map, we compare how several standard summaries, including persistence landscapes, persistence images, persistence splines, and sliced Wasserstein constructions, deform the underlying  $\text{POT}_1$  geometry. This highlights the specific geometric biases induced by different vectorizations and helps explain part of their empirical behavior in the supervised and unsupervised experiments.
4. **Improved empirical performance.** Comparing against full experimental suite of Pegoraro (2026) with the refined definition yields generally improved results across the same case studies, while avoiding any ad-hoc reweighting of persistence pairs.

**Outline.** After this introduction, Section 2 recalls the convex-analytic background on support functions and lift zonoids, and Section 3 develops the measure-theoretic setting, including integrable measures, partial optimal transport, and its comparison with ordinary optimal transport on cross-augmented measures. In Section 4 we review the classical lift-zonoid transform and its continuity properties, and in Section 5 we introduce the new signed lift-zonoid formulation of persistence spheres, prove injectivity, and analyze basic qualitative phenomena. The core bi-continuity theory is established in Section 6: we first prove uniform stability with respect to  $\text{POT}_1$ , then derive inverse continuity, including a local Hölder-type inverse bound on fixed compact sets. We then pass to Hilbert-valued formulations in Section 7, where we obtain  $L^2(\mathbb{S}^2)$  versions of the main continuity results and compare our regime with related Hilbert embeddings from the literature. Section 8 places the signed augmentation strategy in a broader perspective, discussing how it relates to other linear summaries and kernel constructions, while Section 9 studies how different summaries deform the  $\text{POT}_1$  geometry in simple model cases. Finally, the empirical part evaluates the revised construction on supervised benchmarks (Section 11) and unsupervised simulations (Section 10), before Section 12 concludes with implications, limitations, and directions for future work.

## 2. Convex Sets and Support Functions

We briefly review the notation and concepts from convex analysis and geometry that will be used throughout. Standard references include Rockafellar (1997); Salinetti and Wets (1979).

**Definition 1** Given convex sets  $A, B \subset \mathbb{R}^3$  and a scalar  $\lambda \geq 0$ , define

$$A \oplus B := \{a + b : a \in A, b \in B\}, \quad \lambda A := \{\lambda a : a \in A\}.$$

**Definition 2** Given a compact convex set  $A \subset \mathbb{R}^3$ , its support function is

$$h_A : \mathbb{R}^3 \rightarrow \mathbb{R}, \quad h_A(v) := \max_{a \in A} \langle v, a \rangle.$$

The restriction  $h_A|_{\mathbb{S}^2}$  determines  $h_A$  (hence  $A$ ), and Minkowski operations are linearized by support functions:

$$h_{\lambda_1 A \oplus \lambda_2 B} = \lambda_1 h_A + \lambda_2 h_B \quad (\lambda_1, \lambda_2 \geq 0).$$

**Definition 3** Given compact subsets  $A, B \subset Z$ , with  $(Z, d_Z)$  a metric space, their Hausdorff distance is

$$d_H(A, B) := \max \left\{ \sup_{a \in A} d_Z(a, B), \sup_{b \in B} d_Z(b, A) \right\}.$$

**Proposition 1** Let  $A, B \subset \mathbb{R}^3$  be nonempty compact convex sets. Then

$$d_H(A, B) = \|h_A - h_B\|_{L^\infty(\mathbb{S}^2)} = \sup_{v \in \mathbb{S}^2} |h_A(v) - h_B(v)|,$$

where  $d_H$  here denotes the Hausdorff distance induced by the Euclidean norm on  $\mathbb{R}^3$ . In particular, the map

$$A \mapsto h_A|_{\mathbb{S}^2}$$

is injective.

## 3. Integrable Measures and Partial Optimal Transport

For  $r \geq 0$ , denote

$$B_r := \{p \in \mathbb{R}^2 : \|p\|_2 \leq r\}, \quad B_r^c := \mathbb{R}^2 \setminus B_r.$$

We will work with *integrable* measures and *uniformly integrable* sequences; see, e.g., Hendrych and Nagy (2022).

**Definition 4** Let  $Z \subset \mathbb{R}^2$  be a Borel set. A positive Borel measure  $\mu$  on  $E$  is called integrable if it is finite and

$$\int_Z \|p\|_2 d\mu(p) < \infty.$$

If  $Z = X$ , we denote by  $\mathcal{M}$  the set of integrable positive Borel measures on  $X$ . A sequence of integrable measures  $\{\mu_n\}_{n \in \mathbb{N}}$  on  $Z$  is uniformly integrable if

$$\lim_{r \rightarrow \infty} \sup_{n \in \mathbb{N}} \int_{Z \cap B_r^c} \|p\|_2 d\mu_n(p) = 0.$$

Since  $\mathbb{R}^2$  is a locally compact Polish space, every finite Borel measure on  $\mathbb{R}^2$  is a Radon measure. In particular, every integrable measure (Definition 4) is Radon, hence the results of Divol and Lacombe (2021) apply throughout.

To compare measures we use weak and vague convergence; see, e.g., Kallenberg (1997).

**Definition 5** A sequence of integrable measures  $\{\mu_n\}_{n \in \mathbb{N}}$  converges weakly to  $\mu$ , written  $\mu_n \xrightarrow{w} \mu$ , if

$$\int_{\mathbb{R}^2} f d\mu_n \rightarrow \int_{\mathbb{R}^2} f d\mu \quad \text{for every continuous bounded } f : \mathbb{R}^2 \rightarrow \mathbb{R}.$$

It converges vaguely to  $\mu$ , written  $\mu_n \xrightarrow{v} \mu$ , if

$$\int_{\mathbb{R}^2} f d\mu_n \rightarrow \int_{\mathbb{R}^2} f d\mu \quad \text{for every continuous compactly supported } f : \mathbb{R}^2 \rightarrow \mathbb{R}.$$

### 3.1 Measures and persistence

We adopt a measure-theoretic perspective on persistence diagrams (PDs), following Divol and Lacombe (2021). Set

$$X := \mathbb{R}_{x < y}^2 = \{(x, y) \in \mathbb{R}^2 : x < y\}, \quad \Delta := \{(x, y) \in \mathbb{R}^2 : x = y\}, \quad \bar{X} := X \cup \Delta.$$

For  $p = (x, y) \in \mathbb{R}^2$ , let  $\pi_\Delta(p)$  be its projection onto  $\Delta$  in the  $\infty$ -norm:

$$\pi_\Delta(p) \in \arg \min_{z \in \Delta} \|p - z\|_\infty, \quad \text{so that} \quad \pi_\Delta(x, y) = (d(p), d(p)),$$

with  $d(p) := \frac{x+y}{2}$ . Moreover set

$$\text{Pers}(p) := \|p - \pi_\Delta(p)\|_\infty = \frac{y-x}{2} \quad (p \in X).$$

**Definition 6** Let  $\mu$  be a measure on  $X$  and let  $Z \subset X$  be measurable. We define

$$\text{Pers}_Z(\mu) := \int_Z \text{Pers}(p) d\mu(p) = \int_Z \|p - \pi_\Delta(p)\|_\infty d\mu(p) = \frac{1}{2} \int_Z (y - x) d\mu((x, y)).$$

When  $Z = X$ , we simply write  $\text{Pers}(\mu)$ .

Note that, for  $p = (x, y) \in X$ ,

$$\text{Pers}(p) = \frac{y-x}{2} \leq \frac{|y|+|x|}{2} = \frac{\|p\|_1}{2} \leq \frac{\sqrt{2}}{2} \|p\|_2.$$

Therefore, for any positive Borel measure  $\mu$  on  $X$ ,

$$\text{Pers}(\mu) = \int_X \text{Pers}(p) d\mu(p) \leq \frac{\sqrt{2}}{2} \int_X \|p\|_2 d\mu(p).$$

So, for every  $\mu \in \mathcal{M}$ , we have  $\text{Pers}(\mu) < \infty$ .

### 3.2 Optimal Transport and Partial optimal transport.

If  $T, S$  are measurable spaces,  $f : T \rightarrow S$  is measurable, and  $\eta$  is a (Borel) measure on  $T$ , the *pushforward*  $f_{\#}\eta$  is the measure on  $S$  defined by

$$(f_{\#}\eta)(A) := \eta(f^{-1}(A)) \quad \text{for every measurable } A \subset S.$$

For every nonnegative measurable function  $g : S \rightarrow [0, +\infty]$ , one has the identity

$$\int_S g(s) d(f_{\#}\eta)(s) = \int_T g(f(t)) d\eta(t). \quad (1)$$

For two (positive) measures  $\mu, \nu$  on the same measurable space, we write

$$\mu \leq \nu \iff \mu(A) \leq \nu(A) \quad \text{for every measurable } A \subset S.$$

**Partial Optimal Transport.** Let  $\pi_1, \pi_2$  be the canonical projections

$$\pi_1 : X \times X \rightarrow X, \quad (u, v) \mapsto u, \quad \pi_2 : X \times X \rightarrow X, \quad (u, v) \mapsto v.$$

A *partial transport plan* between  $\mu, \nu \in \mathcal{M}$  is a Borel measure  $\gamma$  on  $X \times X$  such that

$$(\pi_1)_{\#}\gamma \leq \mu, \quad (\pi_2)_{\#}\gamma \leq \nu.$$

Its cost is

$$\begin{aligned} \mathcal{C}(\gamma; \mu, \nu) &:= \int_{X \times X} \|p - q\|_{\infty} d\gamma(p, q) \\ &\quad + \int_X \|p - \pi_{\Delta}(p)\|_{\infty} d(\mu - (\pi_1)_{\#}\gamma)(p) \\ &\quad + \int_X \|q - \pi_{\Delta}(q)\|_{\infty} d(\nu - (\pi_2)_{\#}\gamma)(q). \end{aligned}$$

**Definition 7** For  $\mu, \nu \in \mathcal{M}$  we define the *partial optimal transport 1-Wasserstein distance*

$$\text{POT}_1(\mu, \nu) := \inf_{\gamma} \mathcal{C}(\gamma; \mu, \nu),$$

where the infimum ranges over all partial transport plans  $\gamma$  between  $\mu$  and  $\nu$ .

We recall a key convergence criterion for  $\text{POT}_1$  from Divol and Lacombe (2021).

**Theorem 1 (Convergence for  $\text{POT}_1$ )** Let  $\mu \in \mathcal{M}$  and let  $\{\mu_n\}_{n \in \mathbb{N}} \subset \mathcal{M}$ . Then

$$\text{POT}_1(\mu_n, \mu) \rightarrow 0 \iff \mu_n \xrightarrow{v} \mu \text{ and } \text{Pers}(\mu_n) \rightarrow \text{Pers}(\mu).$$

**Optimal Transport.** Let  $\tilde{\mu}, \tilde{\nu}$  be positive Borel measures on  $\bar{X}$  such that  $\tilde{\mu}(\bar{X}) = \tilde{\nu}(\bar{X})$ . Let  $\text{pr}_1, \text{pr}_2$  be the canonical projections

$$\text{pr}_1 : \bar{X} \times \bar{X} \rightarrow \bar{X}, \quad (u, v) \mapsto u, \quad \text{pr}_2 : \bar{X} \times \bar{X} \rightarrow \bar{X}, \quad (u, v) \mapsto v.$$

We denote by  $\Pi(\tilde{\mu}, \tilde{\nu})$  the set of *couplings* of  $\tilde{\mu}$  and  $\tilde{\nu}$ , i.e., the set of positive Borel measures  $\Gamma$  on  $\bar{X} \times \bar{X}$  such that

$$(\text{pr}_1)_{\#}\Gamma = \tilde{\mu}, \quad (\text{pr}_2)_{\#}\Gamma = \tilde{\nu}.$$

**Definition 8** *The 1-Wasserstein distance between  $\tilde{\mu}, \tilde{\nu}$  positive Borel measures on  $\overline{X}$  is*

$$\text{OT}_1(\tilde{\mu}, \tilde{\nu}) := \inf_{\Gamma \in \Pi(\tilde{\mu}, \tilde{\nu})} \int_{\overline{X} \times \overline{X}} \|u - v\|_\infty d\Gamma(u, v).$$

**Partial Optimal Transport vs Optimal Transport.**

A useful way to view  $\text{POT}_1$  is relating it to a standard  $\text{OT}_1$  problem after enlarging the space by the diagonal. In  $\text{POT}_1$ , any portion of mass that is left unmatched is “killed” by sending it to the diagonal, paying the persistence cost  $\|p - \pi_\Delta(p)\|_\infty = \text{Pers}(p)$ . This can be replicated by an ordinary transport plan if we add to each measure enough mass on the diagonal to serve as a sink (or source) for deletions. Concretely, if  $\mu$  must delete some mass while matching to  $\nu$ , we compensate by adding to  $\nu$  the corresponding diagonal projection  $(\pi_\Delta)_\# \mu$ , so that all mass is transported in the augmented space  $\overline{X} = X \cup \Delta$ . The resulting augmented measures have equal total mass and can be compared by the usual 1-Wasserstein distance on  $\overline{X}$ .

**Definition 9** *Let  $\mu, \nu \in \mathcal{M}$ . The cross-augmented measure of  $\mu$  by  $\nu$  is the positive Borel measure on  $\overline{X}$  defined by*

$$\mu \oplus_\Delta \nu := \mu + (\pi_\Delta)_\# \nu. \quad (2)$$

**Proposition 2** *If  $\mu, \nu \in \mathcal{M}$ , then  $\mu \oplus_\Delta \nu$  is an integrable measure on  $\overline{X}$ .*

**Proof** Using (1) with  $f = \pi_\Delta : X \rightarrow \Delta$  and  $g(z) = \|z\|_2$ , the inequality  $\|\pi_\Delta(p)\|_2 \leq \|p\|_2$  yields

$$\int_\Delta \|z\|_2 d(\pi_\Delta)_\# \nu(z) = \int_X \|\pi_\Delta(p)\|_2 d\nu(p) \leq \int_X \|p\|_2 d\nu(p) < \infty.$$

Therefore,

$$\int_{\overline{X}} \|u\|_2 d(\mu \oplus_\Delta \nu)(u) = \int_X \|p\|_2 d\mu(p) + \int_\Delta \|z\|_2 d(\pi_\Delta)_\# \nu(z) < \infty,$$

so  $\mu \oplus_\Delta \nu$  is integrable on  $\overline{X}$ . ■

The cross-augmentation construction yields an equivalence (up to universal constants) between  $\text{POT}_1$  on  $X$  and  $\text{OT}_1$  on  $\overline{X}$ . This is crucial because it allows us to treat partial matching and deletions using the classical optimal transport formalism: in particular we can invoke Kantorovich–Rubinstein duality and the large body of tools developed for  $\text{OT}_1$ . Many of the forward estimates in this paper ultimately rely on rewriting differences of Lipschitz sphere functions as integrals against cross-augmented positive measures, so that  $\text{OT}_1$  duality becomes available.

**Proposition 3** *For all  $\mu, \nu \in \mathcal{M}$ ,*

$$\text{POT}_1(\mu, \nu) \leq \text{OT}_1(\mu \oplus_\Delta \nu, \nu \oplus_\Delta \mu) \leq 2 \text{POT}_1(\mu, \nu).$$

**Proof First inequality.** Fix a coupling  $\Gamma \in \Pi(\mu \oplus_\Delta \nu, \nu \oplus_\Delta \mu)$  and decompose it by restriction to the four regions  $X \times X$ ,  $X \times \Delta$ ,  $\Delta \times X$ , and  $\Delta \times \Delta$ , namely

$$\Gamma_{AB} := \mathbf{1}_{A \times B} \Gamma, \quad A, B \in \{X, \Delta\}, \quad \text{so that} \quad \Gamma = \Gamma_{XX} + \Gamma_{X\Delta} + \Gamma_{\Delta X} + \Gamma_{\Delta\Delta}.$$

Set  $\gamma := \Gamma_{XX}$ . Since the first marginal of  $\Gamma$  equals  $\mu \oplus_\Delta \nu$  and the second equals  $\nu \oplus_\Delta \mu$ , we have

$$(\pi_1)_\# \gamma = (\pi_1)_\# \Gamma_{XX} \leq (\mu \oplus_\Delta \nu)|_X = \mu, \quad (\pi_2)_\# \gamma = (\pi_2)_\# \Gamma_{XX} \leq (\nu \oplus_\Delta \mu)|_X = \nu,$$

so  $\gamma$  is a partial transport plan between  $\mu$  and  $\nu$ . Moreover, by comparing the  $X$ -parts of the first and second marginals,

$$\mu - (\pi_1)_\# \gamma = (\pi_1)_\# \Gamma_{X\Delta}, \quad \nu - (\pi_2)_\# \gamma = (\pi_2)_\# \Gamma_{\Delta X}.$$

Hence, by definition of pushforward,

$$\int_X \|p - \pi_\Delta(p)\|_\infty d(\mu - (\pi_1)_\# \gamma)(p) = \int_{X \times \Delta} \|p - \pi_\Delta(p)\|_\infty d\Gamma_{X\Delta}(p, z).$$

Since for every  $(p, z) \in X \times \Delta$  one has

$$\|p - \pi_\Delta(p)\|_\infty = \inf_{w \in \Delta} \|p - w\|_\infty \leq \|p - z\|_\infty,$$

it follows that

$$\int_X \|p - \pi_\Delta(p)\|_\infty d(\mu - (\pi_1)_\# \gamma)(p) \leq \int_{X \times \Delta} \|p - z\|_\infty d\Gamma_{X\Delta}(p, z).$$

The same argument gives

$$\int_X \|q - \pi_\Delta(q)\|_\infty d(\nu - (\pi_2)_\# \gamma)(q) \leq \int_{\Delta \times X} \|z - q\|_\infty d\Gamma_{\Delta X}(z, q).$$

Thus, we obtain

$$\begin{aligned} \mathcal{C}(\gamma; \mu, \nu) &\leq \int_{X \times X} \|p - q\|_\infty d\Gamma_{XX}(p, q) + \int_{X \times \Delta} \|p - z\|_\infty d\Gamma_{X\Delta}(p, z) + \int_{\Delta \times X} \|z - q\|_\infty d\Gamma_{\Delta X}(z, q) \\ &\leq \int_{\overline{X} \times \overline{X}} \|u - v\|_\infty d\Gamma(u, v), \end{aligned}$$

where we drop the nonnegative contribution of  $\Gamma_{\Delta\Delta}$ . Taking the infimum over all couplings  $\Gamma$  yields

$$\text{POT}_1(\mu, \nu) \leq \text{OT}_1(\mu \oplus_\Delta \nu, \nu \oplus_\Delta \mu).$$

**Second inequality.** Let  $\gamma$  be any partial transport plan between  $\mu$  and  $\nu$ , and set

$$\mu' := (\pi_1)_\# \gamma, \quad \nu' := (\pi_2)_\# \gamma, \quad \xi := \mu - \mu', \quad \eta := \nu - \nu'.$$

Define a coupling  $\Gamma \in \Pi(\mu \oplus_\Delta \nu, \nu \oplus_\Delta \mu)$  by

$$\Gamma := \gamma + (\text{Id}, \pi_\Delta)_\# \xi + (\pi_\Delta, \text{Id})_\# \eta + (\pi_\Delta \circ \pi_2, \pi_\Delta \circ \pi_1)_\# \gamma,$$

where  $(\text{Id}, \pi_\Delta) : X \rightarrow X \times \Delta$ ,  $(\pi_\Delta, \text{Id}) : X \rightarrow \Delta \times X$  and  $(\pi_\Delta \circ \pi_2, \pi_\Delta \circ \pi_1) : X \times X \rightarrow \Delta \times \Delta$  are the indicated maps.

We compute the first marginal term by term. Using linearity of pushforward,

$$(\text{pr}_1)_\# \Gamma = (\text{pr}_1)_\# \gamma + (\text{pr}_1)_\# (\text{Id}, \pi_\Delta)_\# \xi + (\text{pr}_1)_\# (\pi_\Delta, \text{Id})_\# \eta + (\text{pr}_1)_\# (\pi_\Delta \circ \pi_2, \pi_\Delta \circ \pi_1)_\# \gamma.$$

Now:

- Since  $\mu' = (\pi_1)_\# \gamma$  and  $\text{pr}_1 = \pi_1$  on  $X \times X$ , we have

$$(\text{pr}_1)_\# \gamma = \mu'.$$

- For the second term,  $\text{pr}_1 \circ (\text{Id}, \pi_\Delta) = \text{Id}$  on  $X$ , hence

$$(\text{pr}_1)_\#(\text{Id}, \pi_\Delta)_\# \xi = \xi.$$

- For the third term,  $\text{pr}_1 \circ (\pi_\Delta, \text{Id}) = \pi_\Delta$  on  $X$ , hence

$$(\text{pr}_1)_\#(\pi_\Delta, \text{Id})_\# \eta = (\pi_\Delta)_\# \eta.$$

- For the last term,  $\text{pr}_1 \circ (\pi_\Delta \circ \pi_2, \pi_\Delta \circ \pi_1) = \pi_\Delta \circ \pi_2$  on  $X \times X$ , so

$$(\text{pr}_1)_\#(\pi_\Delta \circ \pi_2, \pi_\Delta \circ \pi_1)_\# \gamma = (\pi_\Delta \circ \pi_2)_\# \gamma = (\pi_\Delta)_\#(\pi_2)_\# \gamma = (\pi_\Delta)_\# \nu'.$$

Collecting terms gives

$$(\text{pr}_1)_\# \Gamma = \mu' + \xi + (\pi_\Delta)_\# \nu' + (\pi_\Delta)_\# \eta = (\mu' + \xi) + (\pi_\Delta)_\#(\nu' + \eta) = \mu + (\pi_\Delta)_\# \nu = \mu \oplus_\Delta \nu,$$

where we used  $\mu = \mu' + \xi$  and  $\nu = \nu' + \eta$  by definition of  $\xi, \eta$ .

Similarly  $(\text{pr}_2)_\# \Gamma = \nu \oplus_\Delta \mu$ , hence  $\Gamma$  is indeed a coupling of the cross-augmented measures.

For the transport cost, the first three terms contribute exactly

$$\int_{X \times X} \|p - q\|_\infty d\gamma(p, q) + \int_X \|p - \pi_\Delta(p)\|_\infty d\xi(p) + \int_X \|q - \pi_\Delta(q)\|_\infty d\eta(q).$$

For the last term, integrated on  $\Delta \times \Delta$ , we use that  $\pi_\Delta$  is 1-Lipschitz for  $\|\cdot\|_\infty$ , hence for  $(p, q) \in X \times X$ ,

$$\|\pi_\Delta(q) - \pi_\Delta(p)\|_\infty \leq \|q - p\|_\infty.$$

Therefore,

$$\int_{\Delta \times \Delta} \|u - v\|_\infty d[(\pi_\Delta \circ \pi_2, \pi_\Delta \circ \pi_1)_\# \gamma](u, v) \leq \int_{X \times X} \|p - q\|_\infty d\gamma(p, q).$$

Combining the bounds yields

$$\int_{\bar{X} \times \bar{X}} \|u - v\|_\infty d\Gamma(u, v) \leq 2\mathcal{C}(\gamma; \mu, \nu).$$

Taking the infimum over  $\Gamma$  on the left-hand side and then the infimum over partial plans  $\gamma$  on the right-hand side gives

$$\text{OT}_1(\mu \oplus_\Delta \nu, \nu \oplus_\Delta \mu) \leq 2 \text{POT}_1(\mu, \nu).$$

■

#### 4. Lift Zonoids

Our starting point is the classical lift-zonoid construction (Koshevoy and Mosler, 1998; Hendrych and Nagy, 2022). For an integrable positive measure  $\mu$  on  $\mathbb{R}^2$ , the map

$$v \longmapsto \int_{\mathbb{R}^2} \text{ReLU}(\langle v, (1, p) \rangle) d\mu(p)$$

is the support function of a compact convex set  $Z_\mu \subset \mathbb{R}^3$ , called the *lift zonoid* of  $\mu$ . This correspondence is one of the main geometric ingredients underlying the original persistence-sphere construction of Pegoraro (2026). In the present paper we will eventually need a linear extension of this ReLU integral to deal with diagonal augmentation, but we begin with the classical positive setting, where the convex-geometric picture is most transparent.

For  $p = (x, y) \in \mathbb{R}^2$  we write  $(1, p) := (1, x, y) \in \mathbb{R}^3$  and  $\text{ReLU}(t) := \max\{0, t\}$ .

**Definition 10 (Lift zonoid)** *Let  $\mu$  be an integrable measure on  $\mathbb{R}^2$ . The lift zonoid of  $\mu$  is the unique compact convex set  $Z_\mu \subset \mathbb{R}^3$  whose support function satisfies*

$$h_{Z_\mu}(v) = \int_{\mathbb{R}^2} \text{ReLU}(\langle v, (1, p) \rangle) d\mu(p), \quad v \in \mathbb{R}^3.$$

A key example, already exploited in Pegoraro (2026), is obtained when  $\mu$  is a discrete measure. In that case the lift-zonoid construction becomes completely explicit: each atom contributes a line segment in  $\mathbb{R}^3$ , and the lift zonoid is obtained by Minkowski summation of these segments. This gives a concrete geometric interpretation of the ReLU integral and is useful both for intuition and for later comparisons with persistence-diagram summaries. See also Figure 1.

**Example 1** *Let  $\mu = \sum_{i=1}^n c_i \delta_{p_i}$  with  $p_i \in \mathbb{R}^2$  and  $c_i > 0$ . Then*

$$Z_\mu = \bigoplus_{i=1}^n c_i [0, (1, p_i)] \subset \mathbb{R}^3,$$

and its support function is

$$h_{Z_\mu}(v) = \sum_{i=1}^n c_i \text{ReLU}(\langle v, (1, p_i) \rangle).$$

The lift-zonoid correspondence is especially powerful: the map  $\mu \mapsto Z_\mu$  is injective and enjoys sharp continuity properties. In particular, Hausdorff convergence of lift zonoids is equivalent to weak convergence together with uniform integrability of the underlying measures. This “bi-continuity” principle is one of the central mechanisms in Pegoraro (2026), since it allows one to pass back and forth between measures, support functions, and convex bodies.

**Proposition 4 (Convergence of Lift Zonoids)** *Let  $\mu$  be an integrable measure on  $\mathbb{R}^2$  and let  $\{\mu_n\}_{n \in \mathbb{N}}$  be a sequence of integrable measures. Then*

$$d_H(Z_{\mu_n}, Z_\mu) \rightarrow 0 \iff \mu_n \xrightarrow{w} \mu \text{ and } \{\mu_n\}_{n \in \mathbb{N}} \text{ is uniformly integrable.}$$

The construction developed in the next section is inspired by this classical picture, but adapted to the partial-transport geometry of persistence diagrams. There, the natural object is no longer a positive lift zonoid itself, but a linear ReLU transform applied to the signed augmentation that encodes transport to the diagonal.

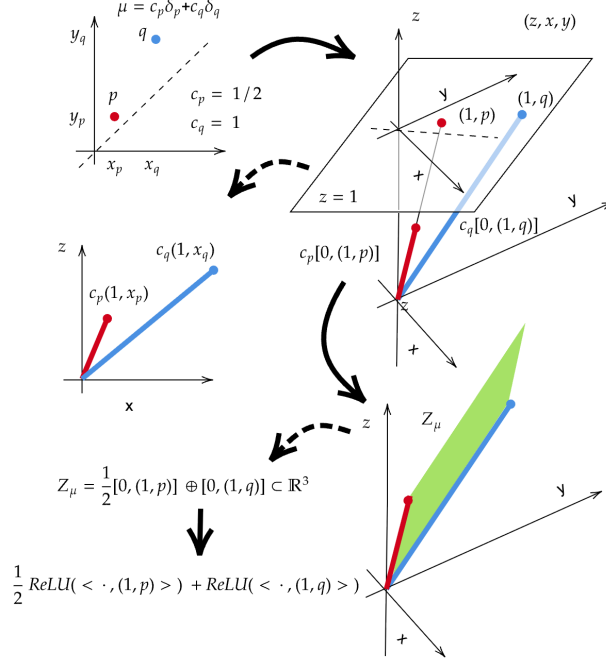


Figure 1: Example of the lift zonoid construction for a discrete measure  $\mu = \sum_i c_i \delta_{p_i}$ . Each atom contributes the segment  $c_i[0, (1, p_i)] \subset \mathbb{R}^3$ , and  $Z_\mu$  is obtained as their Minkowski sum.

## 5. Persistence Spheres via Signed Lift-Zonoid Transforms

We now introduce the linear transform underlying the new persistence-sphere construction. Motivated by Section 4, we keep the same ReLU integrand as in the lift-zonoid representation, but use it in a purely linear way so as to accommodate the diagonal augmentation naturally associated with  $\text{POT}_1$ .

**Definition 11 (Signed Lift-Zonoid Transform)** *Let  $\sigma$  be a finite signed Borel measure on  $\mathbb{R}^2$  such that*

$$\int_{\mathbb{R}^2} \|(1, p)\|_2 d|\sigma|(p) < \infty,$$

where  $|\sigma|$  denotes the total variation measure. The signed lift-zonoid transform of  $\sigma$  is the function

$$\Lambda(\sigma) : \mathbb{R}^3 \rightarrow \mathbb{R}, \quad \Lambda(\sigma)(v) := \int_{\mathbb{R}^2} \text{ReLU}(\langle v, (1, p) \rangle) d\sigma(p).$$

**Proposition 5** *For  $\sigma_1, \sigma_2$  satisfying Definition 11 and  $\lambda_1, \lambda_2 \in \mathbb{R}$ ,*

$$\Lambda(\lambda_1 \sigma_1 + \lambda_2 \sigma_2) = \lambda_1 \Lambda(\sigma_1) + \lambda_2 \Lambda(\sigma_2).$$

For positive integrable measures, this reduces exactly to the support-function representation of Definition 10. Thus the signed transform should be viewed as a linear extension of the classical lift-zonoid formula rather than as a different construction.

We define persistence spheres from measures on the upper half-plane  $X$  by augmenting each measure through its diagonal projection  $\pi_\Delta$ .

**Definition 12 (Augmented Measure)** Let  $\mu$  be a positive Borel measure on  $X$ . We define its augmented measure as the signed measure on  $\overline{X}$

$$\mu^{\text{aug}} := \mu - (\pi_\Delta)_\# \mu.$$

**Proposition 6** Let  $\mu \in \mathcal{M}$ . Then  $\mu^{\text{aug}}$  satisfies the integrability condition of Definition 11, and therefore  $\Lambda(\mu^{\text{aug}})$  is well defined.

**Proof** Using (1) with  $f = \pi_\Delta : X \rightarrow \Delta$  and  $g(z) = \|(1, z)\|_2$ , the inequality  $\|\pi_\Delta(p)\|_2 \leq \|p\|_2$  gives

$$\int_\Delta \|(1, z)\|_2 d(\pi_\Delta)_\# \mu(z) = \int_X \|(1, \pi_\Delta(p))\|_2 d\mu(p) \leq \int_X \|(1, p)\|_2 d\mu(p) < \infty.$$

Hence

$$\int_{\overline{X}} \|(1, u)\|_2 d|\mu^{\text{aug}}|(u) \leq \int_X \|(1, p)\|_2 d\mu(p) + \int_\Delta \|(1, z)\|_2 d(\pi_\Delta)_\# \mu(z) < \infty,$$

so  $\mu^{\text{aug}}$  satisfies Definition 11. ■

**Definition 13 (Persistence sphere)** For  $\mu \in \mathcal{M}$ , the persistence sphere of  $\mu$  is the restriction to  $\mathbb{S}^2$  of the signed lift-zonoid transform of its augmentation:

$$S(\mu) : \mathbb{S}^2 \rightarrow \mathbb{R}, \quad S(\mu) := (\Lambda(\mu^{\text{aug}}))|_{\mathbb{S}^2}.$$

We now relate differences of persistence spheres to cross-augmentation. Given  $\mu, \nu \in \mathcal{M}$ , recall  $\mu \oplus_\Delta \nu = \mu + (\pi_\Delta)_\# \nu$  from (2). A direct computation yields the identity of signed measures on  $\overline{X}$ ,

$$\mu^{\text{aug}} - \nu^{\text{aug}} = (\mu \oplus_\Delta \nu) - (\nu \oplus_\Delta \mu). \quad (3)$$

By linearity of  $\Lambda$  (Proposition 5), restricting to  $\mathbb{S}^2$  gives

$$S(\mu) - S(\nu) = \left( \Lambda(\mu \oplus_\Delta \nu) - \Lambda(\nu \oplus_\Delta \mu) \right) \Big|_{\mathbb{S}^2}. \quad (4)$$

Consequently, for any norm  $\|\cdot\|$  on a function space over  $\mathbb{S}^2$  (e.g.  $L^p(\mathbb{S}^2)$  or  $L^\infty(\mathbb{S}^2)$ ),

$$\|S(\mu) - S(\nu)\| = \left\| \left( \Lambda(\mu \oplus_\Delta \nu) - \Lambda(\nu \oplus_\Delta \mu) \right) \Big|_{\mathbb{S}^2} \right\|. \quad (5)$$

Note that the measures  $\mu \oplus_\Delta \nu$  and  $\nu \oplus_\Delta \mu$  are positive by construction. Moreover, they are integrable on  $\overline{X}$  by Proposition 2. Thus, although persistence spheres are defined through an augmented signed measure, their differences can be expressed in terms of positive cross-augmented measures, which will allow us to recover injectivity and continuity properties by comparison with the classical lift-zonoid setting.

The persistence-sphere construction here differs substantially from the one in Pegoraro (2026). There, one first reweights the diagram measure through a persistence-dependent scheme with additional dependence on  $\|p\|_2$ , and then applies the lift-zonoid transform, so that the resulting function is directly the support function of a lift zonoid. In contrast, we avoid reweighting altogether and encode deletions through diagonal augmentation, yielding a parameter-free definition at the level of measures (up to numerical evaluation choices).

As a first step, we obtain injectivity of the novel representation.

**Proposition 7** *Let  $\mu, \nu \in \mathcal{M}$ . If  $S(\mu) = S(\nu)$ , then  $\mu = \nu$ .*

**Proof** By Equation (5),  $S(\mu) = S(\nu)$  implies  $\Lambda(\mu \oplus_{\Delta} \nu) = \Lambda(\nu \oplus_{\Delta} \mu)$ , and injectivity of the lift-zonoid transform on integrable measures (Koshevoy and Mosler, 1998; Hendrych and Nagy, 2022), in turn, gives  $\mu \oplus_{\Delta} \nu = \nu \oplus_{\Delta} \mu$  as positive measures on  $\overline{X}$ . Thus,  $\mu - \nu = (\pi_{\Delta})_{\#}(\nu - \mu)$ . As the measures on the two sides of the equality have disjoint supports, they must be zero for every measurable set. ■

### 5.1 A Convenient Change of Coordinates

With the persistence-sphere map now in place, we next introduce a change of coordinates adapted to the structure of POT. This reformulation is not essential for the definition itself, but it simplifies the expressions appearing below and clarifies the geometric role of persistence.

We want to separate *diagonal* and *off-diagonal* variability. For  $v = (v_0, v_1, v_2) \in \mathbb{S}^2$  define

$$s(v) := v_1 + v_2, \quad t(v) := v_2 - v_1, \quad (6)$$

which represent, respectively, the components of  $(v_1, v_2)$  along  $(1, 1)$  (diagonal direction) and  $(-1, 1)$  (off-diagonal direction). For  $p = (x, y) \in X$  recall that

$$d(p) = \frac{x + y}{2}, \quad \text{Pers}(p) = \frac{y - x}{2}, \quad (7)$$

so that  $d$  is the coordinate along the diagonal and  $\text{Pers}$  is the distance to the diagonal (persistence). With this notation, the ReLU arguments appearing in the definition of persistence spheres decompose as

$$\langle v, (1, p) \rangle = v_0 + s(v) d(p) + t(v) \text{Pers}(p), \quad \langle v, (1, \pi_{\Delta}(p)) \rangle = v_0 + s(v) d(p). \quad (8)$$

In particular, the pointwise integrand in the definition of  $S$  is

$$\phi_v(p) := \text{ReLU}(v_0 + d(p) s(v) + \text{Pers}(p) t(v)) - \text{ReLU}(v_0 + d(p) s(v)). \quad (9)$$

Equation (8) will be used repeatedly in the upcoming proofs, since it makes explicit how directions  $v$  probe diagonal location ( $s(v)$ ) and how they probe persistence ( $t(v)$ ). It also makes transparent an important qualitative feature of persistence spheres: under large one-sided translations along the diagonal, the representation eventually forgets the exact  $d$ -location and retains only the persistence contribution, as the two  $d$ -contributions delete each other.

Lastly we recall that ReLU is 1-Lipschitz:

$$|\text{ReLU}(a) - \text{ReLU}(b)| \leq |a - b| \quad \forall a, b \in \mathbb{R}. \quad (10)$$

**Proposition 8 (Diagonal drifts)** *Let  $\{\mu_n\} \subset \mathcal{M}$  be a sequence of integrable measures and assume there exists  $M < \infty$  such that*

$$\sup_n \sup_{p \in \text{supp}(\mu_n)} \text{Pers}(p) \leq M. \quad (11)$$

**(A<sub>+</sub>) Drift to  $+\infty$  along the diagonal.** *Assume*

$$\forall R > 0, \quad \mu_n(\{d \leq R\}) \longrightarrow 0. \quad (12)$$

Then for every fixed  $v \in \mathbb{S}^2$  with  $s(v) \neq 0$ ,

$$S(\mu_n)(v) - \mathbf{1}_{\{s(v)>0\}} t(v) \text{Pers}(\mu_n) \longrightarrow 0. \quad (13)$$

In particular, if  $\text{Pers}(\mu_n) \rightarrow P \in [0, \infty)$ , then for every such  $v$ ,

$$S(\mu_n)(v) \longrightarrow \begin{cases} 0, & s(v) < 0, \\ t(v) P, & s(v) > 0. \end{cases}$$

**(A<sub>-</sub>) Drift to  $-\infty$  along the diagonal.** Assume

$$\forall R > 0, \quad \mu_n(\{d \geq -R\}) \longrightarrow 0. \quad (14)$$

Then for every fixed  $v \in \mathbb{S}^2$  with  $s(v) \neq 0$ ,

$$S(\mu_n)(v) - \mathbf{1}_{\{s(v)<0\}} t(v) \text{Pers}(\mu_n) \longrightarrow 0. \quad (15)$$

In particular, if  $\text{Pers}(\mu_n) \rightarrow P \in [0, \infty)$ , then for every such  $v$ ,

$$S(\mu_n)(v) \longrightarrow \begin{cases} t(v) P, & s(v) < 0, \\ 0, & s(v) > 0. \end{cases}$$

**Proof** We prove (A<sub>+</sub>); the proof of (A<sub>-</sub>) is analogous.

Fix  $v \in \mathbb{S}^2$  with  $s(v) \neq 0$ , and abbreviate

$$s := s(v), \quad t := t(v).$$

We choose

$$R_v := \frac{|v_0| + |t|M + 1}{|s|}$$

so that, whenever  $d(p) \geq R_v$ , one has

$$|s| d(p) \geq |v_0| + |t|M + 1.$$

Let now  $p \in X$  satisfy  $d(p) \geq R_v$  and suppose  $s > 0$ .

Recall that Equation (8),

$$\langle v, (1, \pi_\Delta(p)) \rangle = v_0 + s d(p), \quad \langle v, (1, p) \rangle = v_0 + s d(p) + t \text{Pers}(p).$$

Since  $d(p) \geq R_v$ , we have

$$s d(p) \geq s R_v = |v_0| + |t|M + 1.$$

Therefore

$$\langle v, (1, \pi_\Delta(p)) \rangle = v_0 + s d(p) \geq v_0 + s R_v \geq |t|M + 1 > 0,$$

and, using also  $\text{Pers}(p) \leq M$ ,

$$\langle v, (1, p) \rangle = v_0 + s d(p) + t \text{Pers}(p) \geq v_0 + s R_v - |t| \text{Pers}(p) \geq v_0 + s R_v - |t|M \geq 1 > 0.$$

Hence both ReLU arguments are positive and therefore

$$\phi_v(p) = \langle v, (1, p) \rangle - \langle v, (1, \pi_\Delta(p)) \rangle = t \text{Pers}(p).$$

If instead  $s < 0$ , then again using (11),

$$\langle v, (1, \pi_\Delta(p)) \rangle = v_0 + s d(p) \leq v_0 + s R_v < -|t|M - 1 < 0,$$

and

$$\langle v, (1, p) \rangle = v_0 + s d(p) + t \text{Pers}(p) \leq v_0 + s R_v + |t|M \leq -1 < 0.$$

Hence both ReLU arguments are negative and therefore

$$\phi_v(p) = 0.$$

Thus, for every  $p$  with  $d(p) \geq R_v$ ,

$$\phi_v(p) = \mathbf{1}_{\{s>0\}} t \text{Pers}(p).$$

It follows that

$$S(\mu_n)(v) - \mathbf{1}_{\{s>0\}} t \text{Pers}(\mu_n) = \int_{\{d < R_v\}} \left( \phi_v(p) - \mathbf{1}_{\{s>0\}} t \text{Pers}(p) \right) d\mu_n(p).$$

Using (9) and the 1-Lipschitz property of ReLU,

$$|\phi_v(p)| \leq |t| \text{Pers}(p) \leq |t|M,$$

hence

$$\left| \phi_v(p) - \mathbf{1}_{\{s>0\}} t \text{Pers}(p) \right| \leq 2|t|M \quad \text{for all } p \in X.$$

Therefore

$$\left| S(\mu_n)(v) - \mathbf{1}_{\{s>0\}} t \text{Pers}(\mu_n) \right| \leq 2|t|M \mu_n(\{d < R_v\}).$$

Since (12) holds for every  $R > 0$ , in particular for  $R = R_v$ , the right-hand side tends to 0. This proves (13). The final convergence statement follows immediately if  $\text{Pers}(\mu_n) \rightarrow P$ .

The proof of (A<sub>-</sub>) is identical, exchanging the roles of the two tails.  $\blacksquare$

Moreover, for every  $\mu$ , the persistence sphere  $S(\mu)$  satisfies a sign constraint on the region  $\{t(v) < 0\} = \{v_1 > v_2\}$ .

**Lemma 1 (A general sign constraint)** *Let  $\mu \in \mathcal{M}$ . Then for every  $v \in \mathbb{S}^2$  such that  $t(v) \leq 0$ ,*

$$S(\mu)(v) \leq 0.$$

**Proof** By Equation (9), if  $t(v) \leq 0$  then for every  $p \in X$  the first ReLU argument is bounded above by the second one. Hence

$$\phi_v(p) \leq 0 \quad \forall p \in X,$$

and therefore

$$S(\mu)(v) = \int_X \phi_v(p) d\mu(p) \leq 0. \quad \blacksquare$$

Proposition 8 makes precise a flattening phenomenon for persistence spheres under one-sided diagonal drift. Under a uniform bound on persistence, the sign of the ReLU arguments in Equation (8) stabilizes for every fixed direction with  $s(v) \neq 0$ , and the sphere

values eventually depend only on the total persistence. In this regime, differences purely in the diagonal coordinate  $d$  are asymptotically erased: once mass is translated far enough along  $(1, 1)$  in one direction, the representation retains only whether the chosen direction detects that tail, and, if so, through the scalar factor  $t(v) \text{Pers}(\mu_n)$ . The counting-measure case is made explicit in Corollary 1.

This should not be viewed as an isolated pathology of persistence spheres. Rather, some form of flattening or geometric compression appears to be unavoidable for every linearization of persistence diagrams: any passage to a linear space necessarily distorts part of the original partial-transport geometry. What is specific to persistence spheres is the particularly transparent form that this effect takes under diagonal drift, which can be described explicitly in terms of the coordinates  $s(v)$  and  $t(v)$ . We return to this broader theme in Section 9, where persistence spheres are compared with other standard summaries from this viewpoint.

By contrast, Lemma 1 is a general one-sided fact: directions with  $t(v) \leq 0$  always yield a nonpositive contribution, independently of any asymptotic regime.

A key observation is that the pointwise limits arising in Proposition 8 are discontinuous on  $\mathbb{S}^2$ : for drift to  $+\infty$ , the limiting function is

$$v \mapsto \mathbf{1}_{\{s(v) > 0\}} t(v) P,$$

and for drift to  $-\infty$  it is

$$v \mapsto \mathbf{1}_{\{s(v) < 0\}} t(v) P,$$

with jumps across the great circle  $\{s(v) = 0\}$ . Consequently, such diagonal-drift regimes cannot occur along a sequence for which persistence spheres converge uniformly on  $\mathbb{S}^2$ , since uniform limits of continuous functions are continuous. This observation helps explain why large one-sided diagonal drift must be excluded, or quantitatively controlled, in the uniform inverse-continuity arguments developed later.

**Corollary 1** *Let  $\{p_1, \dots, p_N\}$  be a finite set and  $\mu = \sum_{i=1}^N \delta_{p_i}$ . Define  $\mu_k := \sum_{i=1}^N \delta_{p_i + (k, k)}$ . Then for every  $v \in \mathbb{S}^2$  with  $s(v) \neq 0$ ,*

$$\lim_{k \rightarrow \infty} S(\mu_k)(v) = \begin{cases} 0, & s(v) < 0, \\ t(v) \text{Pers}(\mu), & s(v) > 0. \end{cases}$$

The next lemma quantifies, in a particularly simple one-point setting, how quickly the diagonal-coordinate variability is washed out by large translations along  $(1, 1)$ . More precisely, if two one-point diagrams differ only by a fixed offset in the  $d$ -direction and are both shifted by  $(k, k)$ , then the corresponding persistence spheres become eventually identical in each fixed direction  $v$ , and their uniform discrepancy decays at worst like  $O(1/k)$ . In this sense, the lemma provides a quantitative companion to the pointwise asymptotics of Proposition 8 and corollary 1.

**Lemma 2** *Fix  $p \in X$  and set  $d := d(p)$  and  $P := \text{Pers}(p) > 0$ . Let  $h > 0$  be fixed and, for  $k \geq 1$ , define*

$$\mu_k := \delta_{p + (k, k)}, \quad \nu_k := \delta_{p + (k+h, k+h)}.$$

*Then for every  $k \geq |d| + 2h$ ,*

$$\|S(\mu_k) - S(\nu_k)\|_\infty \leq \frac{2h(1 + \sqrt{2}P)}{k}. \quad (16)$$

**Proof** Fix  $v \in \mathbb{S}^2$  and abbreviate  $s := s(v)$  and  $t := t(v)$ . Set

$$K := tP, \quad a_k := v_0 + s(d+k), \quad F_K(a) := \text{ReLU}(a+K) - \text{ReLU}(a),$$

so that

$$S(\mu_k)(v) = F_K(a_k), \quad S(\nu_k)(v) = F_K(a_k + hs), \quad \Gamma_k(v) = F_K(a_k) - F_K(a_k + hs).$$

Since  $F_K$  is 1-Lipschitz,

$$|\Gamma_k(v)| \leq h|s|. \quad (17)$$

For (16), note that  $F_K$  has breakpoints at  $a = 0$  and  $a = -K$ , hence it is constant (with value either 0 or  $K$ ) outside the interval

$$J_K := [\min\{-K, 0\}, \max\{-K, 0\}] \subset [-|K|, |K|].$$

Therefore, if  $\Gamma_k(v) \neq 0$ , the segment  $[a_k, a_k + hs]$  intersects  $J_K$ , so there exists  $\lambda \in [0, 1]$  such that

$$z := a_k + \lambda hs \in J_K \subset [-|K|, |K|].$$

Hence

$$|a_k| \leq |a_k - z| + |z| \leq \lambda h|s| + |K| \leq h|s| + |K|,$$

and so

$$|a_k| \leq |K| + h|s|. \quad (18)$$

On the other hand,

$$|a_k| = |v_0 + s(d+k)| \geq |s| |d+k| - |v_0| \geq |s| (k - |d|) - 1.$$

Combining with (18) gives, whenever  $\Gamma_k(v) \neq 0$ ,

$$|s| (k - |d|) - 1 \leq |K| + h|s| \quad \implies \quad (k - |d| - h)|s| \leq 1 + |K|.$$

If  $k \geq |d| + 2h$ , then  $k - |d| - h \geq k/2$ , so

$$|s| \leq \frac{2(1 + |K|)}{k}.$$

Plugging into (17) yields

$$|\Gamma_k(v)| \leq h|s| \leq \frac{2h(1 + |K|)}{k}.$$

Finally,  $|K| = |t|P \leq \sqrt{2}P$  since  $|t(v)| \leq \|(v_1, v_2)\|_1 \leq \sqrt{2}$ , so

$$|\Gamma_k(v)| \leq \frac{2h(1 + \sqrt{2}P)}{k}.$$

■

## 6. Uniform Convergence Results

As suggested by Proposition 1, the most natural metric to employ to compare persistence spheres is the sup norm. Thus we start obtaining bi-continuity results relying on such norm, even if it does not meet our final goal of embedding measures in a Hilbert space.

## 6.1 Stability

In this section we establish the forward continuity direction (stability) of persistence spheres: closeness in  $\text{POT}_1$  implies uniform closeness of the associated sphere functions. The key point is that  $S(\mu)$  is built from a ReLU transform, so the difference  $S(\mu) - S(\nu)$  can be rewritten as the action of a fixed Lipschitz test family on two cross-augmented measures. This brings the problem into the scope of Kantorovich–Rubinstein duality for  $\text{OT}_1$ , and yields a global Lipschitz bound  $\|S(\mu) - S(\nu)\|_\infty \lesssim \text{POT}_1(\mu, \nu)$  (Theorem 2). We also emphasize that this choice of metric is essentially forced: as shown in Skraba and Turner (2020) in the broader setting of Wasserstein-stable linear representations of persistence diagrams, one cannot expect stability for linear operators on diagram measures with respect to other Wasserstein distances.

**Theorem 2 (POT<sub>1</sub> Convergence  $\Rightarrow$  Uniform Spheres)** *For all  $\mu, \nu \in \mathcal{M}$ ,*

$$\|S(\mu) - S(\nu)\|_\infty \leq 2\sqrt{2} \text{POT}_1(\mu, \nu).$$

**Proof** Recall the cross-augmentation identity (3):

$$\mu^{\text{aug}} - \nu^{\text{aug}} = (\mu \oplus_\Delta \nu) - (\nu \oplus_\Delta \mu),$$

hence by linearity of  $\Lambda$  (Proposition 5),

$$S(\mu) - S(\nu) = \left( \Lambda(\mu \oplus_\Delta \nu) - \Lambda(\nu \oplus_\Delta \mu) \right) \Big|_{\mathbb{S}^2}. \quad (19)$$

**Step 1: a Lipschitz test family.** For  $v \in \mathbb{S}^2$ , define  $\psi_v : \overline{X} \rightarrow \mathbb{R}$  by

$$\psi_v(u) := \text{ReLU}(\langle v, (1, u) \rangle).$$

Note that

$$\|(v_1, v_2)\|_1 \leq \sqrt{2} \quad \text{for all } v = (v_0, v_1, v_2) \in \mathbb{S}^2. \quad (20)$$

Then  $\psi_v$  is  $\sqrt{2}$ -Lipschitz on  $(\overline{X}, \|\cdot\|_\infty)$ . Indeed, using  $|\text{ReLU}(a) - \text{ReLU}(b)| \leq |a - b|$  and (20), for  $u, w \in \overline{X}$ ,

$$|\psi_v(u) - \psi_v(w)| \leq |\langle v, (1, u) \rangle - \langle v, (1, w) \rangle| = |\langle (v_1, v_2), u - w \rangle| \leq \|(v_1, v_2)\|_1 \|u - w\|_\infty \leq \sqrt{2} \|u - w\|_\infty.$$

**Step 2: Kantorovich–Rubinstein duality for  $\text{OT}_1$ .** Using the dual formulation of  $\text{OT}_1$  (Kantorovich–Rubinstein),

$$\text{OT}_1(\tilde{\mu}, \tilde{\nu}) = \sup_{\text{Lip}(f) \leq 1} \int_{\overline{X}} f d(\tilde{\mu} - \tilde{\nu}),$$

where  $\text{Lip}(f) \leq 1$  is with respect to  $\|\cdot\|_\infty$  on  $\overline{X}$ . Apply this with  $\tilde{\mu} = \mu \oplus_\Delta \nu$  and  $\tilde{\nu} = \nu \oplus_\Delta \mu$ . Since each  $\psi_v$  is  $\sqrt{2}$ -Lipschitz, we obtain for every  $v \in \mathbb{S}^2$ :

$$\begin{aligned} |\Lambda(\mu \oplus_\Delta \nu)(v) - \Lambda(\nu \oplus_\Delta \mu)(v)| &= \left| \int_{\overline{X}} \psi_v(u) d((\mu \oplus_\Delta \nu) - (\nu \oplus_\Delta \mu))(u) \right| \\ &\leq \sqrt{2} \text{OT}_1(\mu \oplus_\Delta \nu, \nu \oplus_\Delta \mu). \end{aligned}$$

Taking the supremum over  $v \in \mathbb{S}^2$  and using (19) gives

$$\|S(\mu) - S(\nu)\|_\infty \leq \sqrt{2} \text{OT}_1(\mu \oplus_\Delta \nu, \nu \oplus_\Delta \mu).$$

Finally, Proposition 3 yields

$$\text{OT}_1(\mu \oplus_\Delta \nu, \nu \oplus_\Delta \mu) \leq 2 \text{POT}_1(\mu, \nu),$$

which concludes the proof. ■

## 6.2 Inverse Continuity

The proof of inverse continuity is more delicate, holds only for convergence to compactly supported measures, and is organized into several steps. We begin by testing persistence spheres in suitable directions, which allows us to detect geometric regimes implied by uniform convergence. We then prove a local inverse estimate for measures supported on a fixed compact set. These ingredients are finally assembled to derive the global inverse-continuity result.

### 6.2.1 TEST DIRECTIONS

The inverse-continuity argument relies on a small set of directions  $v \in \mathbb{S}^2$  for which  $\phi_v$  has a simple form, so that  $S(\mu)(v)$  directly controls specific portions of  $\mu$ . We start with two basic estimates: one reads off total persistence from a single direction, and the other quantifies how much  $S(\eta)$  changes when  $\eta$  is truncated to a measurable subset. We then construct two families of directions: one detecting mass far out in the  $d$ -direction (Lemma 5), and one detecting both low- and high-persistence contributions (Lemma 6).

**Lemma 3 (Total Persistence)** *Let  $v_{\text{Pers}} = (0, -1/\sqrt{2}, 1/\sqrt{2}) \in \mathbb{S}^2$ . Then for every  $\mu \in \mathcal{M}$ ,*

$$S(\mu)(v_{\text{Pers}}) = \sqrt{2} \text{Pers}(\mu), \quad \text{hence} \quad \text{Pers}(\mu) = \frac{1}{\sqrt{2}} S(\mu)(v_{\text{Pers}}).$$

*Consequently, if  $\|S(\mu_n) - S(\mu)\|_\infty \rightarrow 0$ , then  $\text{Pers}(\mu_n) \rightarrow \text{Pers}(\mu)$  and  $\sup_n \text{Pers}(\mu_n) < \infty$ .*

**Proof** Let  $p = (x, y) \in X$ . For  $v_{\text{Pers}} = (0, -1/\sqrt{2}, 1/\sqrt{2})$  we have

$$s(v_{\text{Pers}}) = 0, \quad t(v_{\text{Pers}}) = \sqrt{2}.$$

Therefore, by Equation (8),

$$\langle v_{\text{Pers}}, (1, p) \rangle = \sqrt{2} \text{Pers}(p), \quad \langle v_{\text{Pers}}, (1, \pi_\Delta(p)) \rangle = 0.$$

Since  $\text{Pers}(p) > 0$  on  $X$ , both arguments of ReLU are nonnegative, hence Equation (9) yields

$$\phi_{v_{\text{Pers}}}(p) = \sqrt{2} \text{Pers}(p).$$

Integrating against  $\mu$  gives  $S(\mu)(v_{\text{Pers}}) = \sqrt{2} \text{Pers}(\mu)$ , and the remaining claims follow immediately.  $\blacksquare$

**Lemma 4 (Truncation)** *For any  $\eta \in \mathcal{M}$  and any measurable  $A \subset X$ ,*

$$\|S(\eta) - S(\eta|_A)\|_\infty \leq \sqrt{2} \int_{A^c} \text{Pers}(p) d\eta(p).$$

**Proof** Fix  $v \in \mathbb{S}^2$  and  $p \in X$ . By Equation (9) and the 1-Lipschitz property Equation (10),

$$|\phi_v(p)| \leq |\text{Pers}(p) t(v)| \leq |t(v)| \text{Pers}(p) \leq \|(v_1, v_2)\|_1 \text{Pers}(p) \leq \sqrt{2} \text{Pers}(p),$$

where we used  $|t(v)| = |v_2 - v_1| \leq |v_1| + |v_2| = \|(v_1, v_2)\|_1$  and Equation (20). Therefore,

$$|S(\eta)(v) - S(\eta|_A)(v)| = \left| \int_{A^c} \phi_v(p) d\eta(p) \right| \leq \sqrt{2} \int_{A^c} \text{Pers}(p) d\eta(p),$$

and taking the supremum over  $v \in \mathbb{S}^2$  gives the claim.  $\blacksquare$

**Remark 1** *A particularly simple instance of partial transport is transport to the null measure. Since the only partial plan from  $\eta|_A$  to 0 is the zero plan, all mass is left unmatched and therefore sent to the diagonal. Hence, for every  $\eta \in \mathcal{M}$  and every measurable  $A \subset X$ ,*

$$\text{POT}_1(\eta|_A, 0) = \int_A \text{Pers}(p) d\eta(p).$$

*In the same spirit, combining Lemma 3 with Lemma 4 yields an exact formula for the distance from the null persistence sphere:*

$$\|S(\mu) - S(0)\|_\infty = \sqrt{2} \text{Pers}(\mu), \quad \mu \in \mathcal{M}.$$

*Indeed, Lemma 3 gives the lower bound*

$$\|S(\mu)\|_\infty \geq S(\mu)(v_{\text{Pers}}) = \sqrt{2} \text{Pers}(\mu),$$

*while Lemma 4, applied with  $A = \emptyset$ , gives the matching upper bound*

$$\|S(\mu) - S(0)\|_\infty \leq \sqrt{2} \text{Pers}(\mu).$$

*Thus the uniform distance from  $S(0)$  is determined exactly by the total persistence of  $\mu$ .*

The next lemma constructs, for a compactly supported measure  $\mu$ , a direction  $v \in \mathbb{S}^2$  that kills the contribution of the fixed compact support  $\text{supp } \mu$  and isolates persistence mass escaping far away in the  $d$ -coordinate. Indeed, using Equation (8), we choose  $v_0 < 0$  and small positive coefficients  $s(v), t(v)$  so that both ReLU arguments are nonpositive on  $\text{supp } \mu$ , hence  $S(\mu)(v) = 0$ . On the other hand, once  $d(p)$  is large enough, the term  $v_0 + s(v)d(p)$  becomes positive; in that regime both ReLU arguments are active and their difference is exactly  $t(v) \text{Pers}(p)$ . The direction  $v$  thus suppresses the compact core and detects only persistence mass drifting to  $+\infty$  along the  $d$ -axis.

**Lemma 5 (Far Away)** *Let  $\mu \in \mathcal{M}$  have compact support in  $X$ . Choose  $R_0, M_0 > 0$  such that*

$$\text{supp } \mu \subset \{p \in X : |d(p)| \leq R_0 \text{ and } \text{Pers}(p) \leq M_0\}.$$

*Set*

$$s_0 := \frac{1}{2R_0}, \quad t_0 := \frac{1}{2M_0}, \quad \tilde{v} := \left( -1, \frac{s_0 - t_0}{2}, \frac{s_0 + t_0}{2} \right) \in \mathbb{R}^3, \quad v := \frac{\tilde{v}}{\|\tilde{v}\|_2} \in \mathbb{S}^2.$$

*Then:*

1.  $s(v) > 0$  and  $t(v) > 0$ .
2. For every  $p \in \text{supp } \mu$ ,

$$\langle v, (1, p) \rangle \leq 0 \quad \text{and} \quad \langle v, (1, \pi_\Delta(p)) \rangle < 0,$$

*hence  $S(\mu)(v) = 0$ .*

3. There exists  $R_*(\mu) > 0$  such that for every  $p \in X$  with  $d(p) \geq R_*$ ,

$$\phi_v(p) = \text{ReLU}(\langle v, (1, p) \rangle) - \text{ReLU}(\langle v, (1, \pi_\Delta(p)) \rangle) = \text{Pers}(p) t(v).$$

**Proof (1)** By construction,

$$s(\tilde{v}) = (\tilde{v})_1 + (\tilde{v})_2 = s_0 > 0, \quad t(\tilde{v}) = (\tilde{v})_2 - (\tilde{v})_1 = t_0 > 0.$$

Normalization by the positive scalar  $\|\tilde{v}\|_2$  preserves signs, hence  $s(v) > 0$  and  $t(v) > 0$ .

**(2)** Fix  $p \in \text{supp } \mu$ . Then  $|d(p)| \leq R_0$  and  $\text{Pers}(p) \leq M_0$ . Using Equation (8) with  $v = \tilde{v}$  gives

$$\langle \tilde{v}, (1, p) \rangle = -1 + d(p) s(\tilde{v}) + \text{Pers}(p) t(\tilde{v}), \quad \langle \tilde{v}, (1, \pi_\Delta(p)) \rangle = -1 + d(p) s(\tilde{v}).$$

Since  $s(\tilde{v}) = s_0$  and  $t(\tilde{v}) = t_0$ , we have

$$|d(p) s(\tilde{v})| \leq R_0 s_0 = \frac{1}{2}, \quad |\text{Pers}(p) t(\tilde{v})| \leq M_0 t_0 = \frac{1}{2},$$

hence

$$\langle \tilde{v}, (1, p) \rangle \leq -1 + \frac{1}{2} + \frac{1}{2} = 0, \quad \langle \tilde{v}, (1, \pi_\Delta(p)) \rangle \leq -1 + \frac{1}{2} = -\frac{1}{2} < 0.$$

After normalization the inequalities preserve sign, so the same bounds hold for  $v$ . In particular,  $\text{ReLU}(\langle v, (1, p) \rangle) = 0$  and  $\text{ReLU}(\langle v, (1, \pi_\Delta(p)) \rangle) = 0$  for all  $p \in \text{supp } \mu$ , hence  $\phi_v(p) = 0$  on  $\text{supp } \mu$  by Equation (9). Integrating against  $\mu$  yields  $S(\mu)(v) = 0$ .

**(3)** By Equation (8),

$$\langle v, (1, \pi_\Delta(p)) \rangle = v_0 + d(p) s(v).$$

Since  $s(v) > 0$  by (1), this quantity tends to  $+\infty$  as  $d(p) \rightarrow +\infty$ . Thus there exists  $R_*(\mu) > 0$  such that for all  $p$  with  $d(p) \geq R_*(\mu)$ ,

$$\langle v, (1, \pi_\Delta(p)) \rangle > 0.$$

Moreover,

$$\langle v, (1, p) \rangle = \langle v, (1, \pi_\Delta(p)) \rangle + \text{Pers}(p) t(v) \geq \langle v, (1, \pi_\Delta(p)) \rangle > 0,$$

since  $\text{Pers}(p) \geq 0$  and  $t(v) > 0$ . Hence on  $\{d \geq R_*(\mu)\}$  both ReLU arguments are positive, and therefore

$$\phi_v(p) = \langle v, (1, p) \rangle - \langle v, (1, \pi_\Delta(p)) \rangle = \text{Pers}(p) t(v).$$

■

**Remark 2** ( $d \rightarrow -\infty$ ) Define  $\mathcal{R} : \mathbb{R}^3 \rightarrow \mathbb{R}^3$  by

$$\mathcal{R}(v_0, v_1, v_2) := (v_0, -v_2, -v_1).$$

Then  $s(\mathcal{R}v) = -s(v)$  and  $t(\mathcal{R}v) = t(v)$ , and

$$\langle \mathcal{R}v, (1, p) \rangle = v_0 + (-d(p)) s(v) + \text{Pers}(p) t(v).$$

In particular, if  $v$  is given by Lemma 5, then  $\mathcal{R}v$  satisfies the analogue of Lemma 5(2)–(3) on the  $d \rightarrow -\infty$  side:  $S(\mu)(\mathcal{R}v) = 0$ , and there exists  $R'_*(\mu) > 0$  such that for  $d(p) \leq -R'_*$ ,

$$\phi_{\mathcal{R}v}(p) = \text{Pers}(p) t(v).$$

The next lemma introduces a second family of test directions, this time aimed at probing persistence levels independently of the diagonal coordinate. In contrast with the previous construction, we now impose  $s(v) = 0$ , so that the ReLU arguments no longer depend on  $d(p)$  and are controlled only by  $\text{Pers}(p)$ . By choosing the remaining parameters appropriately, one obtains directions  $v_\delta$  for which the integrand vanishes below a prescribed persistence threshold  $\delta$  and grows linearly above it, namely as

$$t_\delta(\text{Pers} - \delta)_+.$$

In this way, sphere evaluations in these directions isolate the contribution of the high-persistence tail, while suitable combinations also control the mass concentrated at low persistence.

**Lemma 6 (Low and High Persistence)** *For  $\delta \geq 0$  define*

$$t_\delta := \sqrt{\frac{2}{1 + 2\delta^2}}, \quad v_\delta := \left( -\delta t_\delta, -\frac{t_\delta}{2}, \frac{t_\delta}{2} \right) \in \mathbb{S}^2.$$

*Then for every  $\eta \in \mathcal{M}$  and every  $\delta \geq 0$ ,*

$$S(\eta)(v_\delta) = t_\delta \int_X (\text{Pers} - \delta)_+ d\eta, \quad (21)$$

$$\int_{\{\text{Pers} \geq 2\delta\}} \text{Pers} d\eta \leq 2 \int_X (\text{Pers} - \delta)_+ d\eta = \frac{2}{t_\delta} S(\eta)(v_\delta), \quad (22)$$

*and*

$$\int_{\{\text{Pers} < \delta\}} \text{Pers} d\eta \leq \int_X g_\delta(\text{Pers}) d\eta = \frac{1}{\sqrt{2}} S(\eta)(v_0) - 2 \frac{1}{t_\delta} S(\eta)(v_\delta) + \frac{1}{t_{2\delta}} S(\eta)(v_{2\delta}), \quad (23)$$

*where*

$$g_\delta(r) := r - 2(r - \delta)_+ + (r - 2\delta)_+, \quad r \geq 0.$$

**Proof** By construction

$$s(v_\delta) = v_{\delta,1} + v_{\delta,2} = 0, \quad t(v_\delta) = v_{\delta,2} - v_{\delta,1} = t_\delta > 0.$$

Hence for every  $p \in X$ ,

$$\langle v_\delta, (1, p) \rangle = v_{\delta,0} + t_\delta \text{Pers}(p), \quad \langle v_\delta, (1, \pi_\Delta(p)) \rangle = v_{\delta,0}.$$

Since  $v_{\delta,0} = -\delta t_\delta \leq 0$ , we have  $\text{ReLU}(v_{\delta,0}) = 0$ , and therefore Equation (9) yields

$$\phi_{v_\delta}(p) = \text{ReLU}(v_{\delta,0} + t_\delta \text{Pers}(p)) - \text{ReLU}(v_{\delta,0}) = \text{ReLU}(t_\delta(\text{Pers}(p) - \delta)) = t_\delta(\text{Pers}(p) - \delta)_+.$$

Integrating against  $\eta$  gives Equation (21). For  $\delta = 0$  one has  $v_0 = v_{\text{Pers}}$  and  $t_0 = \sqrt{2}$ , so Equation (21) reduces to  $S(\eta)(v_0) = \sqrt{2} \int_X \text{Pers} d\eta$ , consistent with Lemma 3.

For any  $r \geq 0$ ,

$$r \mathbf{1}_{\{r \geq 2\delta\}} \leq 2(r - \delta)_+.$$

Indeed, if  $r < 2\delta$  the left-hand side is 0, while if  $r \geq 2\delta$  then  $(r - \delta)_+ = r - \delta \geq r/2$ , i.e.  $r \leq 2(r - \delta)_+$ . Applying this inequality with  $r = \text{Pers}(p)$  and integrating yields

$$\int_{\{\text{Pers} \geq 2\delta\}} \text{Pers} d\eta \leq 2 \int_X (\text{Pers} - \delta)_+ d\eta,$$

and the final identity in Equation (22) follows from Equation (21).

Define

$$g_\delta(r) := r - 2(r - \delta)_+ + (r - 2\delta)_+, \quad r \geq 0.$$

A direct check gives

$$g_\delta(r) = \begin{cases} r, & 0 \leq r \leq \delta, \\ 2\delta - r, & \delta \leq r \leq 2\delta, \\ 0, & r \geq 2\delta, \end{cases} \quad \text{hence} \quad g_\delta(r) \geq r \mathbf{1}_{\{r < \delta\}}.$$

Therefore,

$$\int_{\{\text{Pers} < \delta\}} \text{Pers} \, d\eta \leq \int_X g_\delta(\text{Pers}) \, d\eta.$$

Finally, expanding  $g_\delta$  and using Equation (21) with parameters 0,  $\delta$ , and  $2\delta$  yields

$$\begin{aligned} \int_X g_\delta(\text{Pers}) \, d\eta &= \int_X \text{Pers} \, d\eta - 2 \int_X (\text{Pers} - \delta)_+ \, d\eta + \int_X (\text{Pers} - 2\delta)_+ \, d\eta \\ &= \frac{1}{\sqrt{2}} S(\eta)(v_0) - 2 \frac{1}{t_\delta} S(\eta)(v_\delta) + \frac{1}{t_{2\delta}} S(\eta)(v_{2\delta}), \end{aligned}$$

where we also used Lemma 3 to rewrite  $\int_X \text{Pers} \, d\eta = \frac{1}{\sqrt{2}} S(\eta)(v_0)$ . This proves Equation (23).  $\blacksquare$

### 6.2.2 VANISHING OF THE TAILS

We now combine the test directions above with the assumption  $\|S(\mu_n) - S(\mu)\|_\infty \rightarrow 0$ , where  $\mu$  has compact support in  $X$ . The goal is to show that  $\mu_n$  cannot carry a persistent amount of mass either far away in the  $d$ -direction, or very near the diagonal, or at very large persistence.

**Lemma 7 (Far-away persistence vanishes)** *Assume  $\|S(\mu_n) - S(\mu)\|_\infty \rightarrow 0$ , where  $\mu$  has compact support in  $X$ . Then there exists  $R_\mu > 0$ , depending only on  $\mu$ , such that for every  $R \geq R_\mu$ ,*

$$\limsup_{n \rightarrow \infty} \int_{\{|d| \geq R\}} \text{Pers} \, d\mu_n = 0.$$

In fact, for every such  $R$ ,

$$\limsup_{n \rightarrow \infty} \int_{\{d \geq R\}} \text{Pers} \, d\mu_n = 0, \quad \limsup_{n \rightarrow \infty} \int_{\{d \leq -R\}} \text{Pers} \, d\mu_n = 0.$$

**Proof** Choose  $R_0, M_0 > 0$  such that

$$\text{supp } \mu \subset \{|d| \leq R_0, \text{Pers} \leq M_0\}.$$

Let  $v \in \mathbb{S}^2$  be the direction given by Lemma 5, and let  $R_+ := R_*(\mu)$  be the threshold from Lemma 5(3). Then  $S(\mu)(v) = 0$ , hence by uniform convergence

$$S(\mu_n)(v) \rightarrow 0.$$

Moreover, for every  $p \in X$ ,

$$\phi_v(p) = \text{ReLU}(v_0 + s(v)d(p) + t(v) \text{Pers}(p)) - \text{ReLU}(v_0 + s(v)d(p)) \geq 0,$$

since  $t(v) > 0$  and  $\text{Pers}(p) \geq 0$ .

Fix any  $R \geq R_+$ . Since  $\{d \geq R\} \subset \{d \geq R_+\}$ , Lemma 5(3) gives

$$\phi_v(p) = t(v) \text{Pers}(p) \quad \text{for all } p \in \{d \geq R\}.$$

Therefore

$$S(\mu_n)(v) = \int_X \phi_v d\mu_n \geq \int_{\{d \geq R\}} \phi_v d\mu_n = t(v) \int_{\{d \geq R\}} \text{Pers} d\mu_n.$$

Taking lim sup and using  $S(\mu_n)(v) \rightarrow 0$ , we obtain

$$\limsup_{n \rightarrow \infty} \int_{\{d \geq R\}} \text{Pers} d\mu_n = 0 \quad \forall R \geq R_+.$$

Now apply the same argument to the reflected direction  $\mathcal{R}v$  from Remark 2. Let  $R_- > 0$  be the corresponding threshold. Then for every  $R \geq R_-$ ,

$$\limsup_{n \rightarrow \infty} \int_{\{d \leq -R\}} \text{Pers} d\mu_n = 0.$$

Finally, set

$$R_\mu := \max\{R_+, R_-\}.$$

Then for every  $R \geq R_\mu$ ,

$$\int_{\{|d| \geq R\}} \text{Pers} d\mu_n = \int_{\{d \geq R\}} \text{Pers} d\mu_n + \int_{\{d \leq -R\}} \text{Pers} d\mu_n,$$

and taking lim sup yields

$$\limsup_{n \rightarrow \infty} \int_{\{|d| \geq R\}} \text{Pers} d\mu_n = 0.$$

■

**Lemma 8 (Low Persistence Vanishes)** *Assume  $\|S(\mu_n) - S(\mu)\|_\infty \rightarrow 0$ , where  $\mu$  has compact support in  $X$ . Let  $\delta > 0$  be such that  $\mu(\{\text{Pers} \leq 2\delta\}) = 0$ . Then*

$$\int_{\{\text{Pers} < \delta\}} \text{Pers} d\mu_n \rightarrow 0.$$

**Proof** By Lemma 6, for every  $n$ ,

$$0 \leq \int_{\{\text{Pers} < \delta\}} \text{Pers} d\mu_n \leq \int_X g_\delta(\text{Pers}) d\mu_n = \frac{1}{\sqrt{2}} S(\mu_n)(v_0) - 2 \frac{1}{t_\delta} S(\mu_n)(v_\delta) + \frac{1}{t_{2\delta}} S(\mu_n)(v_{2\delta}).$$

Since  $\mu(\{\text{Pers} \leq 2\delta\}) = 0$ , we have  $g_\delta(\text{Pers}) = 0$   $\mu$ -a.e., and therefore

$$\int_X g_\delta(\text{Pers}) d\mu = 0.$$

Uniform convergence implies pointwise convergence at the fixed directions  $v_0, v_\delta, v_{2\delta}$ , so the right-hand side converges to

$$\frac{1}{\sqrt{2}} S(\mu)(v_0) - 2 \frac{1}{t_\delta} S(\mu)(v_\delta) + \frac{1}{t_{2\delta}} S(\mu)(v_{2\delta}) = \int_X g_\delta(\text{Pers}) d\mu = 0.$$

Hence,  $\int_{\{\text{Pers} < \delta\}} \text{Pers} d\mu_n \rightarrow 0$ .

■

**Lemma 9 (High Persistence Vanishes)** *Assume  $\|S(\mu_n) - S(\mu)\|_\infty \rightarrow 0$ , where  $\mu$  has compact support in  $X$ . Let*

$$M_\mu := \sup\{\text{Pers}(p) : p \in \text{supp } \mu\} < \infty.$$

*Then for every  $M > 2M_\mu$ ,*

$$\limsup_{n \rightarrow \infty} \int_{\{\text{Pers} \geq M\}} \text{Pers } d\mu_n = 0.$$

**Proof** Set  $\delta := M_\mu$  and consider the direction  $v_\delta$  from Lemma 6. Since  $\text{Pers} \leq \delta$  on  $\text{supp } \mu$ , we have  $(\text{Pers} - \delta)_+ = 0$   $\mu$ -a.e., hence by Equation (21),

$$S(\mu)(v_\delta) = 0.$$

Uniform convergence gives  $S(\mu_n)(v_\delta) \rightarrow 0$ , and therefore

$$\int_X (\text{Pers} - \delta)_+ d\mu_n = \frac{1}{t_\delta} S(\mu_n)(v_\delta) \rightarrow 0.$$

By Equation (22),

$$\int_{\{\text{Pers} \geq 2\delta\}} \text{Pers } d\mu_n \leq 2 \int_X (\text{Pers} - \delta)_+ d\mu_n \rightarrow 0.$$

If  $M > 2M_\mu = 2\delta$ , then  $\{\text{Pers} \geq M\} \subset \{\text{Pers} \geq 2\delta\}$ , so the claim follows.  $\blacksquare$

### 6.2.3 A QUANTITATIVE INVERSE ESTIMATE ON COMPACT SETS

We now restrict to measures supported in a fixed compact set  $K \subset X$ . In this regime, one can obtain an explicit Hölder-type inverse estimate: the  $\text{POT}_1$  distance is controlled by a power of the sphere discrepancy. This is the quantitative compact-core input that will be used in the global inverse-continuity argument below.

To derive such a rate we use recent approximation results for shallow ReLU networks, in particular the Sobolev-to-variation-space embedding proved in Mao et al. (2024). Related approximation results in the uniform norm also appear in Siegel (2025). Indeed, by construction, differences of persistence spheres can be written as differences of integrated ReLU ridge functions. Since  $\text{POT}_1$  is controlled by an  $\text{OT}_1$  distance between the corresponding cross-augmented measures, Kantorovich–Rubinstein duality reduces the problem to testing the signed measure against 1-Lipschitz functions. We then approximate arbitrary Lipschitz test functions on a compact set by ReLU ridge combinations, which turns the sphere discrepancy  $\|S(\mu) - S(\nu)\|_\infty$  into an explicit upper bound on  $\text{POT}_1(\mu, \nu)$ .

**Theorem 3 (Local Hölder Bound)** *Let  $K \subset X$  be compact and set*

$$\delta_K := \inf\{\|p - z\|_\infty : p \in K, z \in \Delta\} > 0, \quad \overline{K} := K \cup \pi_\Delta(K) \subset \overline{X}.$$

*For  $\mu, \nu \in \mathcal{M}$  supported in  $K$ , define*

$$M := \text{Pers}(\mu) + \text{Pers}(\nu), \quad \varepsilon := \|S(\mu) - S(\nu)\|_\infty.$$

*Then there exists a constant  $C_K < \infty$ , depending only on  $K$ , such that*

$$\text{POT}_1(\mu, \nu) \leq C_K M^{3/5} \varepsilon^{2/5}.$$

*Moreover, an admissible explicit choice of  $C_K$  is constructed in the proof.*

**Proof Step 0: reduction to OT<sub>1</sub>.**

Let

$$\eta := \mu^{\text{aug}} - \nu^{\text{aug}},$$

which is a finite signed measure supported in  $\overline{K}$ . By (3) and Proposition 3,

$$\eta = (\mu \oplus_{\Delta} \nu) - (\nu \oplus_{\Delta} \mu), \quad \text{POT}_1(\mu, \nu) \leq \text{OT}_1(\mu \oplus_{\Delta} \nu, \nu \oplus_{\Delta} \mu).$$

By Kantorovich–Rubinstein duality for OT<sub>1</sub>,

$$\text{OT}_1(\mu \oplus_{\Delta} \nu, \nu \oplus_{\Delta} \mu) = \sup_{\text{Lip}(f) \leq 1} \int_{\overline{X}} f d\eta, \quad (24)$$

where the Lipschitz constant is computed with respect to  $\|\cdot\|_{\infty}$  on  $\overline{X}$ .

**Step 1: mollification.**

Fix  $f$  with  $\text{Lip}(f) \leq 1$  (with respect to  $\|\cdot\|_{\infty}$  on  $\overline{X}$ ). Since  $\eta$  is supported in  $\overline{K}$ , only the values of  $f$  on  $\overline{K}$  matter. By the McShane extension theorem (McShane, 1934),  $f|_{\overline{K}}$  admits an extension (still denoted by  $f$ ) to a 1-Lipschitz function on  $\mathbb{R}^2$  (w.r.t.  $\|\cdot\|_{\infty}$ ).

Set

$$R_K := 1 + \sup_{u \in \overline{K}} \|u\|_2, \quad \mathring{B}_{R_K} = \{p \in \mathbb{R}^2 : \|p\|_2 < R_K\} \subset \mathbb{R}^2.$$

Then  $\overline{K} \subset \mathring{B}_{R_K}$ , and  $\mathring{B}_{R_K}$  is a bounded open Lipschitz domain. For brevity, we write

$$W^{5/2}(L^2(B_{R_K})) := W^{5/2,2}(\mathring{B}_{R_K}),$$

with its usual fractional Sobolev norm; see, e.g., Bergh and Löfström (2012).

Let  $\rho \in C_c^{\infty}(\mathbb{R}^2)$  be a standard mollifier,  $\rho \geq 0$ ,  $\int \rho = 1$ , and set

$$\rho_r(x) = r^{-2} \rho(x/r), \quad f_r = \rho_r * f.$$

Then  $f_r \in C^{\infty}(\mathbb{R}^2)$  and, for every  $x \in \overline{K}$ ,

$$|f_r(x) - f(x)| = \left| \int_{\mathbb{R}^2} \rho_r(y) (f(x-y) - f(x)) dy \right| \leq \int_{\mathbb{R}^2} \rho_r(y) \|y\|_{\infty} dy = r \int_{\mathbb{R}^2} \rho(z) \|z\|_{\infty} dz,$$

so that

$$\|f - f_r\|_{L^{\infty}(\overline{K})} \leq c_{\text{moll}} r, \quad c_{\text{moll}} := \int_{\mathbb{R}^2} \rho(z) \|z\|_{\infty} dz. \quad (25)$$

Since  $f$  is 1-Lipschitz with respect to  $\|\cdot\|_{\infty}$ , Rademacher's theorem implies that  $f$  is differentiable a.e., and at every differentiability point one has

$$\|\nabla f(x)\|_1 \leq 1.$$

In particular,

$$\|\partial_i f\|_{L^{\infty}(\mathbb{R}^2)} \leq 1, \quad i = 1, 2.$$

For a multi-index  $\alpha \in \mathbb{N}^2$  with  $|\alpha| = m \geq 1$ , choose  $i \in \{1, 2\}$  with  $\alpha_i \geq 1$  and set  $\beta := \alpha - e_i$  (so  $|\beta| = m - 1$ ). By commutation of convolution with weak derivatives and integration by parts (Evans, 2010),

$$D^{\alpha} f_r = D^{\alpha}(\rho_r * f) = (D^{\alpha} \rho_r) * f = (D^{\beta} \rho_r) * (\partial_i f).$$

Hence, using the  $L^1$ – $L^{\infty}$  Young inequality,

$$\|D^{\alpha} f_r\|_{L^{\infty}(\mathbb{R}^2)} \leq \|D^{\beta} \rho_r\|_{L^1(\mathbb{R}^2)} \|\partial_i f\|_{L^{\infty}(\mathbb{R}^2)} \leq \|D^{\beta} \rho_r\|_{L^1(\mathbb{R}^2)},$$

and therefore

$$\|D^\alpha f_r\|_{L^2(B_{R_K})} \leq |B_{R_K}|^{1/2} \|D^\alpha f_r\|_{L^\infty(\mathbb{R}^2)} \leq |B_{R_K}|^{1/2} \|D^\beta \rho_r\|_{L^1(\mathbb{R}^2)}. \quad (26)$$

By scaling, for every  $|\beta| = m - 1$ ,

$$\|D^\beta \rho_r\|_{L^1(\mathbb{R}^2)} = r^{-(m-1)} \|D^\beta \rho\|_{L^1(\mathbb{R}^2)}.$$

Combining with (26) yields, for each  $|\alpha| = m$ ,

$$\|D^\alpha f_r\|_{L^2(B_{R_K})} \leq C_{K,\rho,m} r^{-(m-1)},$$

with  $C_{K,\rho,m} := |B_{R_K}|^{1/2} \max_{|\beta|=m-1} \|D^\beta \rho\|_{L^1}$ . Summing over the finitely many  $|\alpha| = m$  gives

$$\|D^m f_r\|_{L^2(B_{R_K})} \leq C'_{K,\rho,m} r^{-(m-1)}, \quad \text{where } \|D^m h\|_{L^2(B_{R_K})}^2 := \sum_{|\alpha|=m} \|D^\alpha h\|_{L^2(B_{R_K})}^2. \quad (27)$$

For integer orders  $n \in \mathbb{N}$ , we write

$$\|f\|_{W^{n,2}(B_{R_K})}^2 = \sum_{|\alpha| \leq n} \|D^\alpha f\|_{L^2(B_{R_K})}^2.$$

Applying the derivative bounds above then yields constants  $C_{K,\rho}^{(2)}, C_{K,\rho}^{(3)} < \infty$  such that

$$\|f_r\|_{W^{2,2}(B_{R_K})} \leq C_{K,\rho}^{(2)} r^{-1}, \quad \|f_r\|_{W^{3,2}(B_{R_K})} \leq C_{K,\rho}^{(3)} r^{-2}.$$

Finally, by real interpolation of Sobolev spaces on the bounded Lipschitz domain  $\hat{B}_{R_K}$ ,

$$\|u\|_{W^{2+\theta,2}(B_{R_K})} \leq C_{B_{R_K}} \|u\|_{W^{2,2}(B_{R_K})}^{1-\theta} \|u\|_{W^{3,2}(B_{R_K})}^\theta, \quad 0 < \theta < 1,$$

see e.g. Bergh and Löfström (2012). With  $\theta = \frac{1}{2}$  this gives

$$\|u\|_{W^{5/2,2}(B_{R_K})} \leq C_{B_{R_K}} \|u\|_{W^{2,2}(B_{R_K})}^{1/2} \|u\|_{W^{3,2}(B_{R_K})}^{1/2}.$$

Applying this to  $u = f_r$  yields

$$\|f_r\|_{W^{5/2,2}(B_{R_K})} \leq C_{B_{R_K}} \|f_r\|_{W^{2,2}(B_{R_K})}^{1/2} \|f_r\|_{W^{3,2}(B_{R_K})}^{1/2} \leq c'_{\text{moll},K} r^{-3/2},$$

for a suitable constant  $c'_{\text{moll},K} < \infty$  depending only on  $K$  and the mollifier. Combining this with (25), we obtain

$$\|f - f_r\|_{L^\infty(\bar{K})} \leq c_{\text{moll}} r, \quad \|f_r\|_{W^{5/2}(L^2(B_{R_K}))} \leq c'_{\text{moll},K} r^{-3/2}. \quad (28)$$

## Step 2: ReLU approximation via normalization to the unit ball.

Let

$$B_1 = \{p \in \mathbb{R}^2 : \|p\|_2 \leq 1\}, \quad \mathcal{P}_1 := \left\{x \mapsto \text{ReLU}(\omega \cdot x + b) : \omega \in \mathbb{S}^1, b \in [-1, 1]\right\}.$$

Recall that

$$\|g\|_{K_1(\mathcal{P}_1)} := \inf \left\{ \|\alpha\|_{\text{TV}} : g(x) = \int_{\mathbb{S}^1 \times [-1, 1]} \text{ReLU}(\omega \cdot x + b) d\alpha(\omega, b) \quad \forall x \in B_1 \right\},$$

where  $\alpha$  ranges over finite signed Borel measures on  $\mathbb{S}^1 \times [-1, 1]$ , and  $\|\alpha\|_{\text{TV}} = |\alpha|(\mathbb{S}^1 \times [-1, 1])$  is the total variation norm.

By Mao et al. (2024, Thm. 1), specialized to  $(d, k) = (2, 1)$ , there exists a constant  $A_0 < \infty$  such that

$$\|g\|_{K_1(\mathcal{P}_1)} \leq A_0 \|g\|_{W^{5/2,2}(B_1)} \quad \text{for all } g \in W^{5/2,2}(B_1). \quad (29)$$

For  $h \in W^{3,2}(B_{R_K})$ , define

$$\tilde{h}(x) := h(R_K x), \quad x \in B_1.$$

Since  $B_{R_K} = R_K B_1$ , this is the pullback by the isotropic dilation  $x \mapsto R_K x$ . Then, for each integer  $m = 0, 1, 2, 3$ ,

$$\|D^m \tilde{h}\|_{L^2(B_1)} = R_K^{m-2} \|D^m h\|_{L^2(B_{R_K})}.$$

Hence there exist constants  $C_K^{(2)}, C_K^{(3)} < \infty$ , depending only on  $R_K$ , such that

$$\|\tilde{h}\|_{W^{2,2}(B_1)} \leq C_K^{(2)} \|h\|_{W^{2,2}(B_{R_K})}, \quad \|\tilde{h}\|_{W^{3,2}(B_1)} \leq C_K^{(3)} \|h\|_{W^{3,2}(B_{R_K})}.$$

Interpolating on the fixed domain  $B_1$ , we obtain

$$\|\tilde{h}\|_{W^{5/2,2}(B_1)} \leq C_{\text{sc},K} \|h\|_{W^{5/2,2}(B_{R_K})}, \quad (30)$$

for some constant  $C_{\text{sc},K} < \infty$  depending only on  $R_K$ .

Now suppose

$$\tilde{h}(x) = \int_{\mathbb{S}^1 \times [-1,1]} \text{ReLU}(\omega \cdot x + b) d\alpha(\omega, b), \quad x \in B_1.$$

Then for  $u \in B_{R_K}$ ,

$$\begin{aligned} h(u) &= \tilde{h}(u/R_K) \\ &= \int_{\mathbb{S}^1 \times [-1,1]} \text{ReLU}\left(\omega \cdot \frac{u}{R_K} + b\right) d\alpha(\omega, b) \\ &= \int_{\mathbb{S}^1 \times [-1,1]} \frac{1}{R_K} \text{ReLU}(\omega \cdot u + R_K b) d\alpha(\omega, b). \end{aligned}$$

Since the dilation is isotropic, the direction parameter  $\omega \in \mathbb{S}^1$  is unchanged, while the bias interval rescales from  $[-1, 1]$  to  $[-R_K, R_K]$ . Define

$$\mathcal{P} := \left\{ u \mapsto \text{ReLU}(\omega \cdot u + b) : \omega \in \mathbb{S}^1, b \in [-R_K, R_K] \right\},$$

and

$$T_K : \mathbb{S}^1 \times [-1, 1] \rightarrow \mathbb{S}^1 \times [-R_K, R_K], \quad T_K(\omega, b) := (\omega, R_K b).$$

If we set

$$\beta := \frac{1}{R_K} (T_K)_\# \alpha,$$

then

$$h(u) = \int_{\mathbb{S}^1 \times [-R_K, R_K]} \text{ReLU}(\omega \cdot u + b) d\beta(\omega, b) \quad \forall u \in B_{R_K}.$$

Since  $T_K$  is a homeomorphism, total variation is preserved by pushforward:

$$\|(T_K)_\# \alpha\|_{\text{TV}} = \|\alpha\|_{\text{TV}}.$$

Therefore

$$\|\beta\|_{\text{TV}} = \frac{1}{R_K} \|\alpha\|_{\text{TV}}, \quad \text{and hence} \quad \|h\|_{K_1(\mathcal{P})} \leq \frac{1}{R_K} \|\tilde{h}\|_{K_1(\mathcal{P}_1)}.$$

Combining this with (29) and (30) yields

$$\|h\|_{K_1(\mathcal{P})} \leq A_K \|h\|_{W^{5/2,2}(B_{R_K})}, \quad A_K := \frac{A_0 C_{\text{sc},K}}{R_K}. \quad (31)$$

Applying this to  $h = f_r$  and using (28), we obtain

$$\|f_r\|_{K_1(\mathcal{P})} \leq A_K \|f_r\|_{W^{5/2,2}(B_{R_K})} \leq A_K c'_{\text{moll},K} r^{-3/2}. \quad (32)$$

By the definition of  $\|f_r\|_{K_1(\mathcal{P})}$ , for every  $\varepsilon' > 0$  there exists a finite signed measure  $\beta_{r,\varepsilon'}$  on  $\mathbb{S}^1 \times [-R_K, R_K]$  such that

$$f_r(u) = \int_{\mathbb{S}^1 \times [-R_K, R_K]} \text{ReLU}(\omega \cdot u + b) d\beta_{r,\varepsilon'}(\omega, b) \quad \forall u \in B_{R_K},$$

and

$$\|\beta_{r,\varepsilon'}\|_{\text{TV}} \leq \|f_r\|_{K_1(\mathcal{P})} + \varepsilon'.$$

The map

$$(\omega, b, u) \mapsto \text{ReLU}(\omega \cdot u + b)$$

is continuous, hence bounded, on the compact set  $\mathbb{S}^1 \times [-R_K, R_K] \times \overline{K}$ . Since both  $\eta$  and  $\beta_{r,\varepsilon'}$  are finite signed measures, this integrand belongs to  $L^1(|\beta_{r,\varepsilon'}| \otimes |\eta|)$ . Thus Fubini's theorem applies and gives

$$\int_{\overline{K}} f_r d\eta = \int_{\mathbb{S}^1 \times [-R_K, R_K]} \left( \int_{\overline{K}} \text{ReLU}(\omega \cdot u + b) d\eta(u) \right) d\beta_{r,\varepsilon'}(\omega, b).$$

Hence

$$\left| \int_{\overline{K}} f_r d\eta \right| \leq \|\beta_{r,\varepsilon'}\|_{\text{TV}} \cdot \sup_{\omega \in \mathbb{S}^1, |b| \leq R_K} \left| \int_{\overline{K}} \text{ReLU}(\omega \cdot u + b) d\eta(u) \right|.$$

Letting  $\varepsilon' \downarrow 0$  gives

$$\left| \int_{\overline{K}} f_r d\eta \right| \leq \|f_r\|_{K_1(\mathcal{P})} \cdot \sup_{\omega \in \mathbb{S}^1, |b| \leq R_K} \left| \int_{\overline{K}} \text{ReLU}(\omega \cdot u + b) d\eta(u) \right|. \quad (33)$$

### Step 3: smooth part.

For each  $(\omega, b) \in \mathbb{S}^1 \times [-R_K, R_K]$ , set

$$v := \frac{(b, \omega)}{\sqrt{b^2 + \|\omega\|_2^2}} = \frac{(b, \omega)}{\sqrt{b^2 + 1}} \in \mathbb{S}^2.$$

Then for every  $u \in \mathbb{R}^2$ ,

$$\text{ReLU}(\omega \cdot u + b) = \sqrt{b^2 + 1} \text{ReLU}(\langle v, (1, u) \rangle).$$

Therefore

$$\sup_{\omega \in \mathbb{S}^1, |b| \leq R_K} \left| \int_{\bar{K}} \text{ReLU}(\omega \cdot u + b) d\eta(u) \right| \leq \sqrt{1 + R_K^2} \sup_{v \in \mathbb{S}^2} \left| \int_{\bar{K}} \text{ReLU}(\langle v, (1, u) \rangle) d\eta(u) \right|.$$

Since  $\eta = \mu^{\text{aug}} - \nu^{\text{aug}}$  and so by construction,

$$\int_{\bar{K}} \text{ReLU}(\langle v, (1, u) \rangle) d\eta(u) = S(\mu)(v) - S(\nu)(v),$$

and thus the last supremum equals  $\varepsilon$ . Combining this with (33) and (32), we obtain

$$\left| \int_{\bar{K}} f_r d\eta \right| \leq \sqrt{1 + R_K^2} A_K c'_{\text{moll},K} r^{-3/2} \varepsilon. \quad (34)$$

**Step 4: mollification error.**

By (28),

$$\left| \int_{\bar{K}} (f - f_r) d\eta \right| \leq \|f - f_r\|_{L^\infty(\bar{K})} \|\eta\|_{\text{TV}} \leq c_{\text{moll}} r \|\eta\|_{\text{TV}}.$$

Since  $\mu, \nu$  are supported in  $K$  and  $\text{Pers}(p) \geq \delta_K$  on  $K$ , we have

$$\mu(K) \leq \delta_K^{-1} \text{Pers}(\mu), \quad \nu(K) \leq \delta_K^{-1} \text{Pers}(\nu).$$

Moreover,

$$\|\eta\|_{\text{TV}} \leq \|\mu^{\text{aug}}\|_{\text{TV}} + \|\nu^{\text{aug}}\|_{\text{TV}} \leq 2\mu(K) + 2\nu(K),$$

because  $\mu^{\text{aug}} = \mu - (\pi_\Delta)_\# \mu$  and similarly for  $\nu^{\text{aug}}$ . Hence

$$\|\eta\|_{\text{TV}} \leq \frac{2}{\delta_K} (\text{Pers}(\mu) + \text{Pers}(\nu)) = \frac{2}{\delta_K} M,$$

and therefore

$$\left| \int_{\bar{K}} (f - f_r) d\eta \right| \leq \frac{2}{\delta_K} c_{\text{moll}} r M. \quad (35)$$

**Step 5: optimize in the mollification scale.**

Combining (34) and (35), we find

$$\left| \int_{\bar{K}} f d\eta \right| \leq \underbrace{\sqrt{1 + R_K^2} A_K c'_{\text{moll},K}}_{=:\kappa_K} r^{-3/2} \varepsilon + \underbrace{\frac{2}{\delta_K} c_{\text{moll}} r M}_{=:\lambda_K}.$$

We now optimize over  $r > 0$ . A direct minimization shows that for every fixed  $\kappa, \lambda > 0$ ,

$$\inf_{r>0} (\kappa r^{-3/2} + \lambda r) = C_{\text{opt}} \kappa^{2/5} \lambda^{3/5}, \quad C_{\text{opt}} := \frac{5}{2} \left(\frac{3}{2}\right)^{-3/5}. \quad (36)$$

Applying this with  $\kappa = \kappa_K \varepsilon$  and  $\lambda = \lambda_K M$ , we obtain

$$\left| \int_{\bar{K}} f d\eta \right| \leq C_{\text{opt}} \left( \sqrt{1 + R_K^2} A_K c'_{\text{moll},K} \right)^{2/5} \left( \frac{2}{\delta_K} c_{\text{moll}} \right)^{3/5} M^{3/5} \varepsilon^{2/5}.$$

Taking the supremum over all 1-Lipschitz  $f$  in (24) gives

$$\text{OT}_1(\mu \oplus_\Delta \nu, \nu \oplus_\Delta \mu) \leq C_K M^{3/5} \varepsilon^{2/5},$$

with

$$C_K = C_{\text{opt}} \left( \sqrt{1 + R_K^2} A_K c'_{\text{moll},K} \right)^{2/5} \left( \frac{2}{\delta_K} c_{\text{moll}} \right)^{3/5}.$$

Finally,

$$\text{POT}_1(\mu, \nu) \leq \text{OT}_1(\mu \oplus_{\Delta} \nu, \nu \oplus_{\Delta} \mu),$$

so the thesis follows. ■

**Remark 3** *Tracing the proof shows that one may take*

$$C_K = C_{\text{opt}} \left( \sqrt{1 + R_K^2} A_K c'_{\text{moll},K} \right)^{2/5} \left( \frac{2}{\delta_K} c_{\text{moll}} \right)^{3/5}, \quad (37)$$

where

$$R_K := 1 + \sup_{u \in \bar{K}} \|u\|_2, \quad B_{R_K} := \{p \in \mathbb{R}^2 : \|p\|_2 \leq R_K\}, \quad C_{\text{opt}} := \frac{5}{2} \left( \frac{3}{2} \right)^{-3/5}.$$

Here  $c_{\text{moll}}$  is the constant from (25), and  $c'_{\text{moll},K}$  is any constant such that

$$\|f_r\|_{W^{5/2,2}(B_{R_K})} \leq c'_{\text{moll},K} r^{-3/2}$$

for the standard mollification of a 1-Lipschitz function  $f$  on  $\mathbb{R}^2$ . Moreover,

$$A_K = \frac{A_0 C_{\text{sc},K}}{R_K},$$

where  $A_0$  is the unit-ball constant in (29) and  $C_{\text{sc},K}$  is the scaling constant from (30). In particular, once the mollifier is fixed, all quantities entering (37) depend only on  $K$ .

#### 6.2.4 MAIN INVERSE-CONTINUITY RESULT

We can now complete the inverse-continuity proof. The vanishing lemmas show that, under uniform convergence of persistence spheres toward a compactly supported target  $\mu$ , the persistence mass of  $\mu_n$  outside a suitable compact core becomes negligible. Once restricted to such a fixed compact core, the local Hölder estimate above gives quantitative control of  $\text{POT}_1$  in terms of the residual sphere discrepancy. This yields the desired global convergence.

**Theorem 4 (Uniform Spheres  $\Rightarrow$   $\text{POT}_1$  Convergence)** *Let  $\mu \in \mathcal{M}$  have compact support in  $X$ , and let  $\{\mu_n\} \subset \mathcal{M}$ . If  $\|S(\mu_n) - S(\mu)\|_{\infty} \rightarrow 0$ , then  $\text{POT}_1(\mu_n, \mu) \rightarrow 0$ .*

**Proof Step 1: choose a fixed compact core.** Since  $\text{supp } \mu \subset X$  is compact, there exist

$$\delta_{\mu} := \inf_{p \in \text{supp } \mu} \text{Pers}(p) > 0, \quad M_{\mu} := \sup_{p \in \text{supp } \mu} \text{Pers}(p) < \infty, \quad R_{\mu} := \sup_{p \in \text{supp } \mu} |d(p)| < \infty.$$

Choose

$$0 < \delta < \frac{\delta_{\mu}}{2}, \quad M > 2M_{\mu}.$$

Then

$$\mu(\{\text{Pers} \leq 2\delta\}) = 0, \quad \text{supp } \mu \subset \{|d| \leq R_{\mu}, \delta \leq \text{Pers} \leq M_{\mu}\}.$$

By the strengthened form of Lemma 7, there exists  $R > R_\mu$ , depending only on  $\mu$ , such that

$$\limsup_{n \rightarrow \infty} \int_{\{|d| \geq R\}} \text{Pers} \, d\mu_n = 0.$$

Moreover, by Lemma 8,

$$\int_{\{\text{Pers} < \delta\}} \text{Pers} \, d\mu_n \rightarrow 0,$$

and by Lemma 9,

$$\limsup_{n \rightarrow \infty} \int_{\{\text{Pers} \geq M\}} \text{Pers} \, d\mu_n = 0.$$

Set

$$K := K_{R,\delta,M} := \{p \in X : |d(p)| \leq R, \delta \leq \text{Pers}(p) \leq M\}.$$

Then  $K$  is compact,  $\text{supp} \, \mu \subset K$ , and

$$\limsup_{n \rightarrow \infty} \int_{K^c} \text{Pers} \, d\mu_n = 0. \quad (38)$$

**Step 2: convergence on the fixed compact core.** Set

$$\nu_n := \mu_n|_K.$$

Then  $\nu_n$  and  $\mu$  are both supported in the fixed compact set  $K$ .

By Lemma 4 and (38),

$$\limsup_{n \rightarrow \infty} \|S(\mu_n) - S(\nu_n)\|_\infty \leq \sqrt{2} \limsup_{n \rightarrow \infty} \int_{K^c} \text{Pers} \, d\mu_n = 0.$$

Since  $\|S(\mu_n) - S(\mu)\|_\infty \rightarrow 0$ , it follows that

$$\|S(\nu_n) - S(\mu)\|_\infty \rightarrow 0. \quad (39)$$

Now apply Theorem 3 on the fixed compact set  $K$ . Since

$$\text{Pers}(\nu_n) \leq \text{Pers}(\mu_n),$$

and Lemma 3 gives  $\text{Pers}(\mu_n) \rightarrow \text{Pers}(\mu)$ , there exists  $C_{\text{Pers}} < \infty$  such that

$$\sup_n (\text{Pers}(\nu_n) + \text{Pers}(\mu)) \leq C_{\text{Pers}}.$$

Hence, for all  $n$ ,

$$\text{POT}_1(\nu_n, \mu) \leq C_K (\text{Pers}(\nu_n) + \text{Pers}(\mu))^{3/5} \|S(\nu_n) - S(\mu)\|_\infty^{2/5} \leq C_K C_{\text{Pers}}^{3/5} \|S(\nu_n) - S(\mu)\|_\infty^{2/5}.$$

Using (39), we conclude that

$$\text{POT}_1(\nu_n, \mu) \rightarrow 0. \quad (40)$$

**Step 3: lift back to the full measures.** By the triangle inequality,

$$\text{POT}_1(\mu_n, \mu) \leq \text{POT}_1(\mu_n, \nu_n) + \text{POT}_1(\nu_n, \mu).$$

For the first term, match  $\nu_n$  to itself and leave  $\mu_n - \nu_n = \mu_n|_{K^c}$  unmatched. By Remark 1,

$$\text{POT}_1(\mu_n, \nu_n) \leq \text{POT}_1(\mu_n|_{K^c}, 0) = \int_{K^c} \text{Pers} \, d\mu_n.$$

Therefore, by (38),

$$\limsup_{n \rightarrow \infty} \text{POT}_1(\mu_n, \nu_n) \leq \limsup_{n \rightarrow \infty} \int_{K^c} \text{Pers } d\mu_n = 0,$$

hence

$$\text{POT}_1(\mu_n, \nu_n) \rightarrow 0. \quad (41)$$

Combining (40) and (41), we obtain

$$\text{POT}_1(\mu_n, \mu) \rightarrow 0.$$

■

**Corollary 5 (Counting Measures)** *Assume  $\mu_n = \sum_{i=1}^{N_n} \delta_{p_{n,i}}$  and  $\mu = \sum_{i=1}^N \delta_{p_i}$ . If  $\|S(\mu_n) - S(\mu)\|_\infty \rightarrow 0$ , then  $\text{POT}_1(\mu_n, \mu) \rightarrow 0$ .*

## 7. Hilbert Space Results

In addition to the bi-continuity statement proved above, we collect convergence results that are particularly relevant in applications.

In practice, persistence spheres are used as elements of the Hilbert space  $L^2(\mathbb{S}^2)$  to exploit inner products, PCA-type decompositions, and gradient-based learning pipelines. However, our main stability and inverse-continuity results are naturally formulated in the uniform norm on  $\mathbb{S}^2$ . The aim of this section is to relate these two viewpoints. We first show that, under a uniform Lipschitz bound on the sphere,  $L^2$  and uniform convergence are equivalent. We then introduce a growth-controlled class of measures for which this regularity follows from explicit moment bounds on the associated augmented measures.

### 7.1 Uniform vs $L^2$ Convergence on the Sphere

We begin with a general comparison between the uniform and  $L^2$  topologies on  $\mathbb{S}^2$ . Uniform convergence always implies  $L^2$  convergence, while the converse holds for equi-Lipschitz families. Applied to persistence spheres, this shows that once a uniform Lipschitz bound is available, the Hilbert-space viewpoint in  $L^2(\mathbb{S}^2)$  is fully compatible with the sup-norm framework used in the stability and inverse-continuity results above.

**Proposition 9 (Uniform vs.  $L^2$ )** *Let  $h_n, h \in C(\mathbb{S}^2)$ . Then*

$$\|h_n - h\|_{L^2(\mathbb{S}^2)} \leq |\mathbb{S}^2|^{1/2} \|h_n - h\|_\infty = (4\pi)^{1/2} \|h_n - h\|_\infty,$$

*so  $\|h_n - h\|_\infty \rightarrow 0$  implies  $\|h_n - h\|_{L^2(\mathbb{S}^2)} \rightarrow 0$ .*

*Conversely, assume that  $g_n := h_n - h$  is  $L$ -Lipschitz on  $\mathbb{S}^2$  (for the Euclidean metric inherited from  $\mathbb{R}^3$ ), with a constant  $L$  independent of  $n$ . Then for every  $n$ ,*

$$\|g_n\|_\infty \leq 2 \max \left\{ \pi^{-1/4} L^{1/2} \|g_n\|_{L^2(\mathbb{S}^2)}^{1/2}, \pi^{-1/2} \|g_n\|_{L^2(\mathbb{S}^2)} \right\}. \quad (42)$$

*In particular, under a uniform Lipschitz bound,  $L^2$  and uniform convergence are equivalent.*

**Proof** The first inequality follows immediately from

$$\|g\|_{L^2(\mathbb{S}^2)} \leq |\mathbb{S}^2|^{1/2} \|g\|_\infty.$$

For the converse, fix  $n$  and write  $g := g_n$ ,  $M := \|g\|_\infty$ . Choose  $x \in \mathbb{S}^2$  such that  $|g(x)| = M$ , and let  $\sigma$  denote the surface measure on  $\mathbb{S}^2$ . For  $r \in (0, 2)$ , set

$$B(x, r) := \{y \in \mathbb{S}^2 : \|y - x\|_2 \leq r\}.$$

Since  $g$  is  $L$ -Lipschitz, for every  $y \in B(x, r)$  one has

$$|g(y)| \geq |g(x)| - L\|y - x\|_2 \geq M - Lr.$$

Hence

$$|g(y)| \geq (M - Lr)_+ \quad \forall y \in B(x, r),$$

and therefore

$$\|g\|_{L^2(\mathbb{S}^2)}^2 = \int_{\mathbb{S}^2} |g|^2 d\sigma \geq \int_{B(x, r)} |g(y)|^2 d\sigma(y) \geq \sigma(B(x, r)) (M - Lr)_+^2. \quad (43)$$

We now compute  $\sigma(B(x, r))$ . Writing  $y$  in polar angle  $\theta$  from  $x$ , so that  $\cos \theta = \langle x, y \rangle$ , one has

$$\|y - x\|_2^2 = \|x\|_2^2 + \|y\|_2^2 - 2\langle x, y \rangle = 2 - 2\cos \theta = 4\sin^2(\theta/2).$$

Thus  $\|y - x\|_2 \leq r$  is equivalent to  $\theta \leq 2 \arcsin(r/2)$ . The area of a spherical cap of angular radius  $\theta$  is

$$\sigma(B(x, r)) = 2\pi(1 - \cos \theta).$$

With  $\theta = 2 \arcsin(r/2)$ , using  $\cos(2\alpha) = 1 - 2\sin^2 \alpha$ , we get

$$\cos \theta = \cos(2 \arcsin(r/2)) = 1 - \frac{r^2}{2},$$

hence

$$\sigma(B(x, r)) = 2\pi \left(1 - \left(1 - \frac{r^2}{2}\right)\right) = \pi r^2 \quad \text{for all } 0 < r < 2.$$

Substituting into (43), we obtain

$$\|g\|_{L^2(\mathbb{S}^2)} \geq \sqrt{\pi} r (M - Lr)_+ \quad \forall r \in (0, 2).$$

**Case 1:**  $M \leq 2L$ . Choose  $r = M/(2L) \in (0, 1] \subset (0, 2)$ . Then  $M - Lr = M/2$ , so

$$\|g\|_{L^2(\mathbb{S}^2)} \geq \sqrt{\pi} \frac{M}{2L} \cdot \frac{M}{2} = \frac{\sqrt{\pi}}{4L} M^2.$$

Therefore

$$M \leq 2\pi^{-1/4} L^{1/2} \|g\|_{L^2(\mathbb{S}^2)}^{1/2}.$$

**Case 2:**  $M > 2L$ . Choose  $r = 1 \in (0, 2)$ . Then

$$M - Lr = M - L > \frac{M}{2},$$

hence

$$\|g\|_{L^2(\mathbb{S}^2)} \geq \sqrt{\pi} \cdot 1 \cdot \frac{M}{2},$$

and so

$$M \leq 2\pi^{-1/2} \|g\|_{L^2(\mathbb{S}^2)}.$$

Combining the two cases proves (42). ■

The previous proposition shows that passing from  $L^2$  convergence to uniform convergence on  $\mathbb{S}^2$  reduces to controlling the Lipschitz constants of the sphere functions. For persistence spheres, this regularity is naturally linked to quantitative bounds on the underlying measures. We now introduce a class tailored to this purpose, and then show that on this class  $L^2$  convergence of persistence spheres upgrades to uniform convergence.

In the compact-support regime treated in Section 6.2.3, one can go further and obtain explicit inverse estimates in  $\text{POT}_1$  from sup-norm discrepancies of the associated sphere functions. The results below should be viewed as a Hilbert-space counterpart to that compact-core theory.

## 7.2 A growth-controlled class $\mathcal{M}(\mathcal{A}, \mathcal{B})$

As explained by Proposition 9, the main obstacle to upgrading  $L^2$  convergence to uniform convergence is the possible lack of a *uniform* Lipschitz bound on the differences  $S(\mu_n) - S(\mu)$ . To obtain such control, we work with measures whose local first moment and persistence-weighted far field are quantitatively bounded. Since the argument proceeds by truncating to large compact cores and then applying Proposition 9 on each core, we also impose a compatibility condition ensuring that the truncation error decays fast enough relative to the growth of the local Lipschitz constants.

**Definition 14** *Let  $\mathcal{A}, \mathcal{B}$  be positive Borel measures on  $\mathbb{R}^2$ . We say that the pair  $(\mathcal{A}, \mathcal{B})$  is compatible if:*

- $\mathcal{A}$  is a Radon measure;
- $\mathcal{B}$  is a finite measure;
- 

$$\frac{\mathcal{A}(B_R) \mathcal{B}(\mathbb{R}^2 \setminus B_{R-1})}{R} \xrightarrow{R \rightarrow \infty} 0, \quad (44)$$

where  $B_R = \{p \in \mathbb{R}^2 : \|p\|_2 \leq R\}$ .

Given a compatible pair  $(\mathcal{A}, \mathcal{B})$ , we define  $\mathcal{M}(\mathcal{A}, \mathcal{B})$  as the set of integrable measures  $\mu$  on  $X$  such that for every Borel set  $U \subset \mathbb{R}^2$ ,

$$\int_{U \cap X} \|(1, p)\|_2 d\mu(p) \leq \mathcal{A}(U), \quad (45)$$

$$\int_{U \cap X} \|(1, p)\|_2 \text{Pers}(p) d\mu(p) \leq \mathcal{B}(U). \quad (46)$$

**Remark 4** *Condition (45) gives a local control of the first moment: on each bounded region, the weighted mass  $\int \|(1, p)\|_2 d\mu$  is uniformly bounded by  $\mathcal{A}$ . Condition (46) controls the persistence-weighted far field: since  $\mathcal{B}(\mathbb{R}^2) < \infty$ , the measure  $\|(1, p)\|_2 \text{Pers}(p) \mu(dp)$  has uniformly bounded total mass.*

*The compatibility condition (44) says, roughly speaking, that  $\mathcal{A}(B_R)$  is not allowed to grow too fast compared with the rate at which the tail  $\mathcal{B}(\mathbb{R}^2 \setminus B_{R-1})$  decays.*

**Example 2** *A simple polynomial example is obtained by taking  $\mathcal{A}$  and  $\mathcal{B}$  absolutely continuous with respect to Lebesgue measure, with densities*

$$\rho_{\mathcal{A}}(p) = (1 + \|p\|_2)^\alpha, \quad \rho_{\mathcal{B}}(p) = (1 + \|p\|_2)^{-\beta}, \quad p \in \mathbb{R}^2,$$

for fixed  $\alpha \geq 0$  and  $\beta > \alpha + 3$ . Then

$$\mathcal{A}(B_R) = \int_{B_R} (1 + \|p\|_2)^\alpha dp = 2\pi \int_0^R (1+r)^\alpha r dr \lesssim R^{\alpha+2},$$

and

$$\mathcal{B}(\mathbb{R}^2 \setminus B_{R-1}) = \int_{\|p\|_2 \geq R-1} (1 + \|p\|_2)^{-\beta} dp = 2\pi \int_{R-1}^\infty (1+r)^{-\beta} r dr \lesssim R^{2-\beta}.$$

Therefore

$$\frac{\mathcal{A}(B_R) \mathcal{B}(\mathbb{R}^2 \setminus B_{R-1})}{R} \lesssim R^{\alpha+2} R^{2-\beta} R^{-1} = R^{\alpha+3-\beta} \longrightarrow 0.$$

Hence  $(\mathcal{A}, \mathcal{B})$  is compatible.

In particular, any faster decay for  $\rho_{\mathcal{B}}$ , for instance

$$\rho_{\mathcal{B}}(p) = e^{-\|p\|_2},$$

also yields a compatible pair.

We now show that  $L^2$  convergence implies uniform convergence on  $\mathcal{M}(\mathcal{A}, \mathcal{B})$ .

For  $R > 0$ , set

$$K_R := \{p \in X : \|(1, p)\|_2 \leq R\}, \quad K_R^\Delta := K_R \cup \pi_\Delta(K_R) \subset \bar{X}.$$

The first ingredient is a uniform *truncation* estimate, obtained by combining the truncation lemma

$$\|S(\eta) - S(\eta|_A)\|_\infty \leq \sqrt{2} \int_{A^c} \text{Pers } d\eta$$

with the mixed moment control (46).

**Lemma 10 (Uniform Truncation on  $\mathcal{M}(\mathcal{A}, \mathcal{B})$ )** *Let  $\mu \in \mathcal{M}(\mathcal{A}, \mathcal{B})$  and  $R \geq 1$ . Then*

$$\|S(\mu) - S(\mu|_{K_R})\|_\infty \leq \frac{\sqrt{2}}{R} \mathcal{B}(\mathbb{R}^2 \setminus B_{R-1}), \quad (47)$$

where  $B_{R-1} := \{p \in \mathbb{R}^2 : \|p\|_2 \leq R-1\}$ . In particular, the right-hand side tends to 0 as  $R \rightarrow \infty$ , uniformly over  $\mu \in \mathcal{M}(\mathcal{A}, \mathcal{B})$ .

**Proof** Since  $R \geq 1$ , we have the implication  $\|(1, p)\|_2 \geq R \Rightarrow \|p\|_2 \geq R-1$ , hence

$$K_R^c \subset \mathbb{R}^2 \setminus B_{R-1}.$$

Moreover, since on  $K_R^c$  we have  $\|(1, p)\|_2 \geq R$ , and

$$\text{Pers}(p) \leq \frac{1}{R} \|(1, p)\|_2 \text{Pers}(p).$$

Therefore

$$\int_{K_R^c} \text{Pers } d\mu \leq \frac{1}{R} \int_{K_R^c} \|(1, p)\|_2 \text{Pers}(p) d\mu(p) \leq \frac{1}{R} \mathcal{B}(\mathbb{R}^2 \setminus B_{R-1}),$$

by (46) with  $U = \mathbb{R}^2 \setminus B_{R-1}$ . The truncation lemma then gives (47).  $\blacksquare$

Next, on the truncated core  $K_R$  one has a uniform Lipschitz control in  $v$ , depending only on  $\mathcal{A}(B_R)$ .

**Lemma 11 (Local Uniform Lipschitz Control)** Fix  $R \geq 1$ . There exists a constant  $L_R < \infty$ , depending only on  $\mathcal{A}(B_R)$ , such that for every  $\mu \in \mathcal{M}(\mathcal{A}, \mathcal{B})$ ,

$$\text{Lip}_{\mathbb{S}^2}(S(\mu|_{K_R})) \leq L_R.$$

One may take, for instance,

$$L_R := 2\mathcal{A}(B_R).$$

**Proof** Let  $\nu := \mu|_{K_R}$ . Using that ReLU is 1-Lipschitz and the definition of  $S$ , for  $v, w \in \mathbb{S}^2$ ,

$$\begin{aligned} |S(\nu)(v) - S(\nu)(w)| &\leq \int_{\bar{X}} |\text{ReLU}(\langle v, (1, u) \rangle) - \text{ReLU}(\langle w, (1, u) \rangle)| d|\nu^{\text{aug}}|(u) \\ &\leq \int_{\bar{X}} |\langle v - w, (1, u) \rangle| d|\nu^{\text{aug}}|(u) \\ &\leq \|v - w\|_2 \int_{\bar{X}} \|(1, u)\|_2 d|\nu^{\text{aug}}|(u). \end{aligned}$$

Moreover,  $|\nu^{\text{aug}}| = \nu + (\pi_\Delta)_\# \nu$ , and  $\|(1, \pi_\Delta(p))\|_2 \leq \|(1, p)\|_2$ , hence

$$\int_{\bar{X}} \|(1, u)\|_2 d|\nu^{\text{aug}}|(u) \leq 2 \int_{K_R} \|(1, p)\|_2 d\mu(p) \leq 2\mathcal{A}(B_R),$$

by (45) with  $U = B_R$ . This yields the stated Lipschitz bound.  $\blacksquare$

Putting the truncation and core Lipschitz bounds together yields the desired upgrade from  $L^2$  to uniform convergence.

**Theorem 6 ( $L^2 \Rightarrow L^\infty$  on  $\mathcal{M}(\mathcal{A}, \mathcal{B})$ )** Let  $\mu_n, \mu \in \mathcal{M}(\mathcal{A}, \mathcal{B})$  and assume

$$\|S(\mu_n) - S(\mu)\|_{L^2(\mathbb{S}^2)} \rightarrow 0.$$

Then

$$\|S(\mu_n) - S(\mu)\|_\infty \rightarrow 0.$$

**Proof** For  $R \geq 1$ , define the compact core

$$K_R := \{p \in X : \|(1, p)\|_2 \leq R\},$$

the truncated measures

$$\nu_n := \mu_n|_{K_R}, \quad \nu := \mu|_{K_R},$$

and the truncation defect

$$\tau_R := \frac{\sqrt{2}}{R} \mathcal{B}(\mathbb{R}^2 \setminus B_{R-1}).$$

By Lemma 10, for every  $\eta \in \mathcal{M}(\mathcal{A}, \mathcal{B})$ ,

$$\|S(\eta) - S(\eta|_{K_R})\|_\infty \leq \tau_R. \tag{48}$$

Since  $\mathcal{B}$  is finite,  $\tau_R \rightarrow 0$  as  $R \rightarrow \infty$ .

Fix  $R \geq 1$ . By Lemma 11, each of  $S(\nu_n)$  and  $S(\nu)$  is  $L_R$ -Lipschitz on  $\mathbb{S}^2$ , where

$$L_R := 2\mathcal{A}(B_R).$$

Hence the differences

$$h_n := S(\nu_n) - S(\nu)$$

are  $2L_R$ -Lipschitz on  $\mathbb{S}^2$ .

We now estimate  $\|h_n\|_{L^2(\mathbb{S}^2)}$  for every fixed  $R$ . Indeed, by the triangle inequality,

$$\|h_n\|_{L^2(\mathbb{S}^2)} \leq \|S(\nu_n) - S(\mu_n)\|_{L^2(\mathbb{S}^2)} + \|S(\mu_n) - S(\mu)\|_{L^2(\mathbb{S}^2)} + \|S(\mu) - S(\nu)\|_{L^2(\mathbb{S}^2)}.$$

Applying the first part of Proposition 9 to the first and third terms, and using (48), we obtain

$$\|S(\nu_n) - S(\mu_n)\|_{L^2(\mathbb{S}^2)} \leq (4\pi)^{1/2}\tau_R, \quad \|S(\mu) - S(\nu)\|_{L^2(\mathbb{S}^2)} \leq (4\pi)^{1/2}\tau_R.$$

Therefore, using  $\|S(\mu) - S(\nu)\|_{L^2(\mathbb{S}^2)} \rightarrow 0$ ,

$$\limsup_{n \rightarrow \infty} \|h_n\|_{L^2(\mathbb{S}^2)} \leq 2(4\pi)^{1/2}\tau_R.$$

Now apply the converse part of Proposition 9 to the  $2L_R$ -Lipschitz functions  $h_n$ :

$$\|h_n\|_\infty \leq 2 \max \left\{ \pi^{-1/4}(2L_R)^{1/2} \|h_n\|_{L^2(\mathbb{S}^2)}^{1/2}, \pi^{-1/2} \|h_n\|_{L^2(\mathbb{S}^2)} \right\}.$$

Passing to the limsup gives

$$\begin{aligned} \limsup_{n \rightarrow \infty} \|h_n\|_\infty &\leq 2 \max \left\{ \pi^{-1/4}(2L_R)^{1/2} (2(4\pi)^{1/2}\tau_R)^{1/2}, \pi^{-1/2} 2(4\pi)^{1/2}\tau_R \right\} \\ &= \max \left\{ 4\sqrt{2L_R\tau_R}, 8\tau_R \right\}. \end{aligned} \quad (49)$$

On the other hand, by the triangle inequality and (48),

$$\|S(\mu_n) - S(\mu)\|_\infty \leq \|S(\mu_n) - S(\nu_n)\|_\infty + \|h_n\|_\infty + \|S(\nu) - S(\mu)\|_\infty \leq 2\tau_R + \|h_n\|_\infty.$$

Hence, using (49),

$$\limsup_{n \rightarrow \infty} \|S(\mu_n) - S(\mu)\|_\infty \leq 2\tau_R + \max \left\{ 4\sqrt{2L_R\tau_R}, 8\tau_R \right\}. \quad (50)$$

It remains to let  $R \rightarrow \infty$ . Since  $\tau_R \rightarrow 0$ , the pure  $\tau_R$ -terms vanish. Moreover,

$$L_R\tau_R = 2\mathcal{A}(B_R) \cdot \frac{\sqrt{2}}{R} \mathcal{B}(\mathbb{R}^2 \setminus B_{R-1}),$$

which tends to 0 by the compatibility condition (44). Therefore the right-hand side of (50) tends to 0, and thus

$$\limsup_{n \rightarrow \infty} \|S(\mu_n) - S(\mu)\|_\infty = 0.$$

Hence

$$\|S(\mu_n) - S(\mu)\|_\infty \rightarrow 0. \quad \blacksquare$$

Theorem 6 ensures that, on the class  $\mathcal{M}(\mathcal{A}, \mathcal{B})$ , working in the Hilbert space  $L^2(\mathbb{S}^2)$  is consistent with the uniform-norm theory developed for persistence spheres:  $L^2$  control of sphere errors automatically yields uniform control.

In particular, whenever the reference measure  $\mu$  is compactly supported in  $X$ , Theorem 4 can now be invoked from an  $L^2$  premise.

**Corollary 2 (From  $L^2$  sphere convergence to POT<sub>1</sub> convergence)** *Let  $\mu \in \mathcal{M}(\mathcal{A}, \mathcal{B})$  have compact support in  $X$ , and let  $\mu_n \in \mathcal{M}(\mathcal{A}, \mathcal{B})$ . If  $\|S(\mu_n) - S(\mu)\|_{L^2(\mathbb{S}^2)} \rightarrow 0$ , then  $\text{POT}_1(\mu_n, \mu) \rightarrow 0$ .*

**Definition 15** *Let  $\mathcal{A}, \mathcal{B}$  be as in Definition 14. We define*

$$\mathcal{M}_c(\mathcal{A}, \mathcal{B}) \subset \mathcal{M}(\mathcal{A}, \mathcal{B}),$$

*as the set of measures in  $\mathcal{M}(\mathcal{A}, \mathcal{B})$  whose support is compact in  $X$ .*

**Corollary 7 (Bi-Continuous Embedding)** *Fix  $\mathcal{A}, \mathcal{B}$  as in Definition 14. The persistence-sphere map*

$$S : (\mathcal{M}_c(\mathcal{A}, \mathcal{B}), \text{POT}_1) \longrightarrow (L^2(\mathbb{S}^2), \|\cdot\|_{L^2}), \quad \mu \longmapsto S(\mu),$$

*is injective and bi-continuous onto its image. More precisely:*

1. *for all  $\mu, \nu \in \mathcal{M}_c(\mathcal{A}, \mathcal{B})$ ,*

$$\|S(\mu) - S(\nu)\|_{L^2(\mathbb{S}^2)} \leq (4\pi)^{1/2} \|S(\mu) - S(\nu)\|_\infty \leq 4\sqrt{2\pi} \text{POT}_1(\mu, \nu).$$

2. *if  $\mu_n, \mu \in \mathcal{M}_c(\mathcal{A}, \mathcal{B})$  and  $\|S(\mu_n) - S(\mu)\|_{L^2(\mathbb{S}^2)} \rightarrow 0$ , then  $\text{POT}_1(\mu_n, \mu) \rightarrow 0$ .*

## 8. Discussion: Linear Summaries, Augmentation, and Related Embeddings

### 8.1 Augmentation Strategy

The signed diagonal augmentation used to define persistence spheres can be viewed more broadly as a way to make *linear* summaries of persistence diagrams compatible with the deletion-to-diagonal mechanism of POT<sub>1</sub>, without prescribing ad hoc vanishing weights near the diagonal.

Let  $\Phi$  be a linear integral summary of the form

$$\Phi(\tilde{\mu}) = \int_{\bar{X}} \varphi(\cdot, p) d\tilde{\mu}(p),$$

defined for positive Borel measures  $\tilde{\mu}$  on  $\bar{X}$ , with values in a normed linear space  $(\mathbb{F}, \|\cdot\|_{\mathbb{F}})$ . Many standard constructions fit this template, including persistence images/surfaces and several kernel-based mean embeddings, provided the feature map extends naturally from  $X$  to  $\bar{X} = X \cup \Delta$ .

For a measure  $\mu$  on  $X$ , we consider its signed diagonal augmentation

$$\mu^{\text{aug}} = \mu - (\pi_\Delta)_\# \mu.$$

Then, by linearity and the cross-augmentation identity Equation (3),

$$\Phi(\mu^{\text{aug}}) - \Phi(\nu^{\text{aug}}) = \Phi(\mu \oplus_\Delta \nu) - \Phi(\nu \oplus_\Delta \mu).$$

Thus differences of *signed* augmented features can be rewritten as differences of the same feature map evaluated on *positive* cross-augmented measures. This is the key structural point: once deletions are encoded at the level of measures, comparisons reduce to ordinary optimal transport on  $\bar{X}$ .

Assume now that the feature family is uniformly Lipschitz in the measure variable, namely that there exists  $L < \infty$  such that

$$\|\varphi(\cdot, p) - \varphi(\cdot, q)\|_{\mathbb{F}} \leq L \|p - q\|_{\infty} \quad \forall p, q \in \overline{X}.$$

Then  $\Phi$  is  $L$ -Lipschitz with respect to  $\text{OT}_1$  on positive measures of equal mass. Indeed, if  $\tilde{\mu}, \tilde{\nu}$  are such measures and  $\Gamma \in \Pi(\tilde{\mu}, \tilde{\nu})$  is any coupling, then

$$\begin{aligned} \|\Phi(\tilde{\mu}) - \Phi(\tilde{\nu})\|_{\mathbb{F}} &= \left\| \int_{\overline{X} \times \overline{X}} (\varphi(\cdot, p) - \varphi(\cdot, q)) d\Gamma(p, q) \right\|_{\mathbb{F}} \\ &\leq \int_{\overline{X} \times \overline{X}} \|\varphi(\cdot, p) - \varphi(\cdot, q)\|_{\mathbb{F}} d\Gamma(p, q) \\ &\leq L \int_{\overline{X} \times \overline{X}} \|p - q\|_{\infty} d\Gamma(p, q). \end{aligned}$$

Taking the infimum over  $\Gamma$  gives

$$\|\Phi(\tilde{\mu}) - \Phi(\tilde{\nu})\|_{\mathbb{F}} \leq L \text{OT}_1(\tilde{\mu}, \tilde{\nu}).$$

Applying this with  $\tilde{\mu} = \mu \oplus_{\Delta} \nu$  and  $\tilde{\nu} = \nu \oplus_{\Delta} \mu$ , and using Proposition 3, yields

$$\|\Phi(\mu^{\text{aug}}) - \Phi(\nu^{\text{aug}})\|_{\mathbb{F}} \leq L \text{OT}_1(\mu \oplus_{\Delta} \nu, \nu \oplus_{\Delta} \mu) \leq 2L \text{POT}_1(\mu, \nu).$$

Hence, once the deletion mechanism is built into the representation through diagonal augmentation, no additional diagonal weighting is needed to obtain  $\text{POT}_1$ -stability for linear integral summaries. Note that this also matches the general role of  $\text{POT}_1$  for linear representations emphasized in Skraba and Turner (2020).

Stability, however, is only one side of the problem. To obtain inverse continuity, the feature family  $\{\varphi(\cdot, p)\}_{p \in \overline{X}}$  must also be rich enough to approximate 1-Lipschitz test functions on compact subsets of  $\overline{X}$ . When such an approximation property is available, the same duality-and-approximation mechanism used in Theorem 3 can in principle be adapted to derive local inverse bounds on compact cores. Persistence spheres realize this strategy through ReLU ridge features, for which recent approximation theory provides explicit rates. In this sense, the augmentation principle is more general than persistence spheres themselves: it suggests a systematic route for designing parameter-free,  $\text{POT}_1$ -coherent linear summaries of persistence diagrams.

## 8.2 Comparison with classical summaries of persistence diagrams

The augmentation principle discussed above places persistence spheres within a broader picture of representations for persistence diagrams. A natural comparison is with widely used summaries such as persistence images, persistence landscapes, sliced Wasserstein kernels, and persistence splines (Bubenik, 2015; Adams et al., 2017; Carriere et al., 2017; Dong et al., 2024). These constructions are all useful in practice, but they differ markedly in how they interact with the underlying transport geometry of diagrams.

Another point is important for interpreting our Hilbert-space results. Most known positive Hilbert embeddings of persistence diagrams are established on classes defined by structural restrictions, most often a uniform bound on cardinality. By contrast, the class  $\mathcal{M}_c(\mathcal{A}, \mathcal{B})$  from Definition 15 is designed for a different regime: it allows cardinality to diverge, provided the extra mass concentrates near the diagonal in a quantified way. After reviewing the main classical summaries, we return to this distinction and later complement it in Section 9 with a qualitative comparison of the geometric distortions induced by different representations.

**Persistence images.** Persistence images (Adams et al., 2017) are obtained by first associating to a persistence diagram a *persistence surface*, namely a weighted sum of smoothing kernels centered at the diagram points, and then discretizing this surface on a fixed grid. The persistence surface is a function-valued summary, whereas the discretized image is a vector in a finite-dimensional Euclidean space, hence in a Hilbert space. Under suitable regularity assumptions on the weighting function, in particular its vanishing on the diagonal, and on the smoothing kernel, Adams et al. prove  $\text{POT}_1$ -type stability for both levels of the construction: the persistence surface is stable in sup norm, and the persistence image is stable after discretization (Adams et al., 2017).

What is Hilbert-valued, however, is the discretized representation, not the persistence surface itself. Thus persistence images yield a stable Hilbert-valued summary only once the grid has been fixed. In particular, they do not provide a canonical, resolution-free Hilbert embedding of the space of persistence diagrams, but rather a family of finite-dimensional Euclidean embeddings indexed by the chosen discretization. As we discuss later in Section 9, this linearization also introduces a characteristic geometric bias, driven by kernel smoothing and by the chosen weighting scheme.

**Persistence landscapes.** Persistence landscapes (Bubenik, 2015) associate to each diagram a sequence of tent-like functions and therefore naturally take values in spaces such as  $L^p(\mathbb{N} \times \mathbb{R})$ . In particular, for  $p = 2$  they live in a Hilbert space, which is one of the main reasons for their statistical appeal. The original theory establishes several stability and limit results. In particular, it proves  $L^\infty$ -stability, i.e. sup-norm stability with respect to the bottleneck distance. For finite  $q$ , however, the available bounds are more delicate: they are formulated either in terms of persistence-weighted transport quantities or under additional assumptions, such as bounded total persistence of the underlying diagrams. Thus the original paper does not provide a global Lipschitz statement for the map

$$D \longmapsto \lambda(D)$$

from arbitrary persistence diagrams endowed with  $W_p$  ( $1 \leq p < \infty$ ) into  $L^q$  for finite  $q$ . Indeed, Skraba and Turner (2020) show that for all finite  $p, q$ , the landscape map is in general not even Hölder continuous from persistence diagrams endowed with  $W_p$  to persistence landscapes endowed with the  $L^q$  norm. Thus, although persistence landscapes have a very natural functional-analytic structure, they do not define a globally stable Hilbert embedding in the same metric sense as persistence images or the present construction. This lack of metric faithfulness is closely related to the deformation phenomena examined later in Section 9, where landscapes exhibit a pronounced bias toward high-persistence features.

**Sliced Wasserstein kernels.** Sliced Wasserstein kernels (Carriere et al., 2017) take a different route from the explicit vectorizations discussed above. Rather than assigning coordinates directly to a persistence diagram, they define a positive definite kernel through a sliced optimal transport construction, thereby inducing an implicit embedding into a reproducing kernel Hilbert space. As already noted in the introduction, this is one of the few available constructions that comes with a proved continuity statement for the inverse map on its image, albeit only on bounded-cardinality subclasses.

More precisely, on classes of diagrams with uniformly bounded cardinality, Carriere et al. (2017) show that the sliced Wasserstein distance is quantitatively comparable to the intrinsic  $\text{POT}_1$  geometry. On the same classes, the RKHS distance induced by the kernel admits two-sided control in terms of  $\text{POT}_1$ , via continuous comparison functions; see also the discussion in the introduction. Thus sliced Wasserstein kernels provide a geometrically

faithful Hilbert embedding on bounded-cardinality subclasses. The mechanism, however, is different from ours: their metric control relies on a uniform bound on the number of off-diagonal points, whereas our bi-continuity results are driven instead by  $\text{POT}_1$ -adapted control of tail-to-diagonal mass.

**Positioning of persistence spheres.** Taken together, the summaries discussed above illustrate different compromises between stability, target-space structure, and metric faithfulness. Persistence images and persistence splines provide explicit finite-dimensional Euclidean, hence Hilbert-valued, representations with  $\text{POT}_1$ -type stability. Persistence landscapes also admit a Hilbert-valued realization, but for finite  $L^q$  norms they are not globally Hölder stable under finite- $p$  transport geometries. Sliced Wasserstein kernels are more tightly connected to the intrinsic transport structure, but their strongest embedding guarantees currently rely on bounded-cardinality assumptions (Adams et al., 2017; Dong et al., 2024; Bubenik, 2015; Skraba and Turner, 2020; Carriere et al., 2017).

In this picture, persistence spheres stand out in two respects. On the one hand, they admit a rather general inverse-continuity statement at the level of the uniform norm on  $\mathbb{S}^2$ : for finite measures with compact support, uniform convergence of persistence spheres implies  $\text{POT}_1$ -convergence of the underlying measures. On the other hand, on the more structured growth-controlled class  $\mathcal{M}_c(\mathcal{A}, \mathcal{B})$ , they also yield a Hilbert-valued bi-continuous embedding via Theorem 7.

The class  $\mathcal{M}_c(\mathcal{A}, \mathcal{B})$  itself lies in a different regime from the bounded-cardinality framework that appears in most existing embedding results. Indeed, most bi-Lipschitz, bi-continuous, or coarse embeddings are established under a uniform bound on the number of off-diagonal points, as in Carriere et al. (2017); Mitra and Virk (2024); Bate and Garcia Pulido (2024). By contrast,  $\mathcal{M}_c(\mathcal{A}, \mathcal{B})$  imposes no bound on total mass. For counting measures, it allows the number of points to diverge, provided the additional mass concentrates near the diagonal in a quantified way through the mixed moment bound

$$\int_X \|(1, p)\|_2 \text{Pers}(p) d\mu(p) \leq \mathcal{B}(\mathbb{R}^2),$$

together with the local first-moment control encoded by  $\mathcal{A}$  and the compatibility condition linking the growth of  $\mathcal{A}(B_R)$  to the decay of  $\mathcal{B}(\mathbb{R}^2 \setminus B_{R-1})$ . This is precisely the type of behavior expected in noisy settings, where finer sampling may generate many additional low-persistence features.

A bounded-cardinality assumption and membership in a fixed class  $\mathcal{M}_c(\mathcal{A}, \mathcal{B})$  capture genuinely different regimes. The former does not, by itself, impose any common growth control: even a sequence of one-point diagrams may drift arbitrarily far in the diagonal direction. By contrast,  $\mathcal{M}_c(\mathcal{A}, \mathcal{B})$  is designed to allow increasing cardinality, provided the additional mass accumulates near the diagonal in a controlled way. Accordingly, the mechanism behind Theorem 7 is not a hard cap on the number of points, but a  $\text{POT}_1$ -adapted control of tail-to-diagonal mass.

## 9. Deforming the Wasserstein Geometry

In this section we study, at a qualitative level, how different topological summaries reshape the geometry induced by  $\text{POT}_1$  on persistence diagrams. We do not pursue a formal distortion analysis in the embedding-theoretic sense. Rather, we use the softer expression *deformation of the  $\text{POT}_1$  geometry* to describe how pairwise distances change after mapping diagrams into a Hilbert-valued summary.

Some deformation is unavoidable:  $\text{POT}_1$  does not admit globally bi-Lipschitz Hilbert embeddings in full generality. The relevant question is therefore not whether a summary preserves the geometry exactly, but which geometric biases it introduces and whether these are mild or useful for the task at hand.

We focus on three illustrative cases. First, we compare the revised persistence-sphere definition with the original weighted version from Pegoraro (2026), isolating the role of signed diagonal augmentation. Second, we revisit persistence landscapes in a one-point setting, where their bias toward high persistence becomes explicit. Third, we analyze Gaussian persistence images, which exhibit both a kernel-dependent saturation of pairwise distances and a nontrivial distortion of deletion costs.

### 9.1 Comparison with Pegoraro (2026)

We start with a minimal synthetic example aimed at isolating the effect of the signed diagonal augmentation in the revised definition. The example serves two purposes: it illustrates the improved alignment with the  $\text{POT}_1$  geometry under diagonal translations, and it provides an empirical check of the decay behavior predicted by Corollary 1 and lemma 2.

For  $k \geq 0$ , let

$$p_k := (0, 1) + (k, k), \quad q_k := p_k + \frac{1}{\sqrt{2}}(1, 1),$$

and define the one-point diagrams

$$D_k := \{p_k\}, \quad D'_k := \{q_k\}.$$

Equivalently, in measure form, let  $\mu_k := \delta_{p_k}$  and  $\nu_k := \delta_{q_k}$ . We monitor two quantities:

1. the diagonal-shift discrepancy

$$\|S(\mu_k) - S(\nu_k)\|_{L^2(\mathbb{S}^2)},$$

measuring how strongly a pure  $(1, 1)$ -offset is detected as both points drift along the diagonal; and

2. the deletion cost

$$\|S(\mu_k) - S(0)\|_{L^2(\mathbb{S}^2)} = \|S(\mu_k)\|_{L^2(\mathbb{S}^2)},$$

measuring how the cost of sending  $p_k$  to the diagonal is encoded by the representation.

We compare these curves with the original weighted construction of Pegoraro (2026), using the weighting scheme

$$\lambda(p) := \frac{y - x}{2\|(1, p)\|_2}, \quad \omega_K(p) = \frac{2}{\pi} \arctan\left(\frac{\lambda(p)}{K}\right),$$

for different values of  $K$ . This is a natural benchmark: among the weighting schemes considered in Pegoraro (2026),  $\omega_K$  gave the best practical behavior, and in retrospect this is not surprising, since it qualitatively mimics the diagonal-deletion attenuation that the new definition now encodes intrinsically.

The results are shown in Figure 2. In Figure 2a, all methods exhibit decay of  $\|S(\mu_k) - S(\nu_k)\|_{L^2}$  as  $k \rightarrow \infty$ , but for different reasons. For the updated persistence spheres, the decay is intrinsic and reflects Corollary 1: far along the diagonal, differences in the  $d$ -coordinate are progressively washed out, and the comparison reduces pointwise in  $v$  to

the total persistence weighted by  $t(v)$ . For the older construction, instead, the decay is enforced by the reweighting itself: for every fixed  $K > 0$ , the factor  $\omega_K$  tends to 0 along each diagonal line

$$\ell_q := \left\{ q + s \frac{1}{\sqrt{2}}(1, 1) : s \in \mathbb{R} \right\},$$

so points translated in the direction  $\frac{1}{\sqrt{2}}(1, 1)$  are eventually progressively downweighted.

The deletion plot in Figure 2b makes the main difference even clearer. In the revised definition, Remark 1 shows that comparison with 0 in the sup norm depends only on persistence mass, hence is insensitive to diagonal translations. Since

$$\text{Pers}(p_k) = \text{Pers}(p_0) \quad \text{for all } k,$$

the deletion cost in the new persistence spheres is therefore essentially constant in  $k$ ; the small variability visible for small  $k$  in the figure comes from averaging the directional factor  $t(v)$  through the  $L^2$ -norm. In the weighted construction of Pegoraro (2026), the same qualitative behavior is obtained only indirectly. As  $p_k$  moves away from the origin, the geometric contribution first grows, and only later is this compensated by the decay of  $\omega_K(p_k)$ , producing for both values of  $K$  a more pronounced transient regime and a stabilization that depends on  $K$ .

Overall, Figure 2 shows that the augmentation-based formulation induces a milder deformation of the  $\text{POT}_1$  geometry than the original weighted definition and that the updated persistence spheres recover the same desirable behavior in a parameter-free and geometrically intrinsic way.

## 9.2 Persistence Landscapes

Consider a one-point persistence diagram

$$D = \{p\}, \quad p = (x, y).$$

Its persistence landscape  $\text{PL}(D)$  consists, in this case, of a single tent function centered at  $(x + y)/2$ , with base length  $2 \text{Pers}(p)$  and height  $\text{Pers}(p)$ . Hence the area under this tent is

$$\int_{\mathbb{R}} \text{PL}(D)(t) dt = \text{Pers}(p)^2.$$

Now move the point along the anti-diagonal direction

$$u = \frac{1}{\sqrt{2}}(-1, 1), \quad p_k = p + k u,$$

for  $k \geq 0$ , and define

$$D_k := \{p_k\}.$$

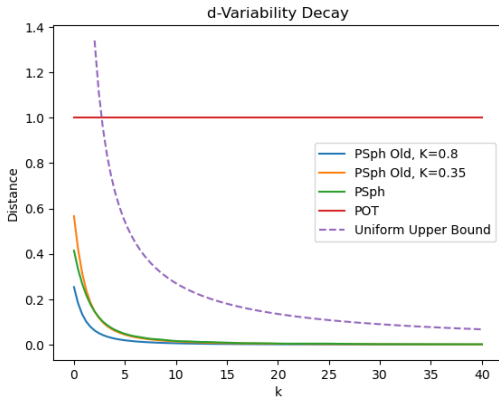
Then

$$\text{Pers}(p_k) = \text{Pers}(p) + \frac{k}{\sqrt{2}},$$

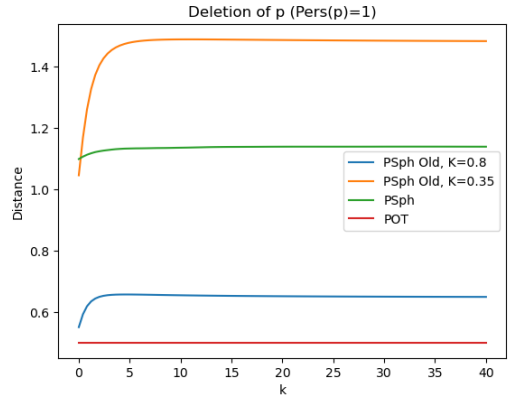
so the area under the corresponding tent becomes

$$\int_{\mathbb{R}} \text{PL}(D_k)(t) dt = \left( \text{Pers}(p) + \frac{k}{\sqrt{2}} \right)^2.$$

Thus the contribution of this single persistence pair grows quadratically in  $k$ .



(a) **Diagonal-shift discrepancy.** The quantity  $\|S(\mu_k) - S(\nu_k)\|_{L^2(\mathbb{S}^2)}$  as a function of  $k$ , for the updated persistence spheres and for the definition of Pegoraro (2026) using  $\omega_K$  with  $K \in \{0.35, 0.8\}$ . For reference we also plot  $\text{POT}_1(\mu_k, \nu_k)$  and the uniform upper bound from Lemma 2: the latter controls  $\|S(\mu_k) - S(\nu_k)\|_\infty$ , whereas the plotted curves average the discrepancy over  $\mathbb{S}^2$  via the  $L^2$  norm.



(b) **Deletion cost.** The quantity  $\|S(\mu_k)\|_{L^2(\mathbb{S}^2)} = \|S(\mu_k) - S(0)\|_{L^2(\mathbb{S}^2)}$  as a function of  $k$ , compared across the updated persistence spheres, the construction of Pegoraro (2026) with  $\omega_K$  ( $K \in \{0.35, 0.08\}$ ), and the deletion cost  $\text{POT}_1(\mu_k, 0) = \text{Pers}(p_0)$ , constant in  $k$ .

Figure 2: One-point diagrams drifting along  $(1, 1)$ . Left: attenuation of a pure diagonal offset between  $D_k$  and  $D'_k$ . Right: behavior of the deletion-to-diagonal cost for  $D_k$ . The updated definition matches the  $\text{POT}_1$  geometry by construction, whereas in Pegoraro (2026) both effects are mediated by the decay of the reweighting  $\omega_K$  along diagonal lines.

A related effect is visible already when comparing two moving one-point diagrams. Let

$$D_k := \{p_k\}, \quad D'_k := \{q_k\},$$

where

$$p = (0, 2), \quad q = (1, 3), \quad q_k = q + k u.$$

Since both points move in the same anti-diagonal direction, their persistence increases at the same linear rate, and a direct computation shows that the distance between the associated landscapes grows linearly in  $k$ ; see Figure 3a. Even in this elementary setting, the landscape geometry reacts strongly to changes that increase persistence.

These computations make explicit the main geometric bias of persistence landscapes: they amplify variability at high persistence. In particular, moving a point in a direction that increases persistence can have a much larger effect on the landscape norm than one would expect from the underlying transport displacement alone.

This behavior is consistent with the general instability results of Skraba and Turner (2020): for every  $q \in [1, \infty)$ , the persistence-landscape map from persistence diagrams endowed with  $W_p$  to  $L^q$  is not Hölder continuous. Their counterexample uses two one-point diagrams,

$$D = \{(0, a)\}, \quad D' = \{(0, a - r)\},$$

with  $r \ll a$ , for which  $W_p(D, D') = r$  while

$$\|\text{PL}(D) - \text{PL}(D')\|_{L^q} \gtrsim r (a/2 - r)^{1/q}.$$

This cannot be bounded uniformly by  $Cr^\alpha$ , and formalizes the same high-persistence amplification seen in the elementary example above.

From the viewpoint adopted here, persistence landscapes deform the  $\text{POT}_1$  geometry by overweighting changes involving highly persistent points. As a result, distances in landscape space need not track  $\text{POT}_1$  uniformly across persistence regimes.

### 9.3 Persistence Images

Persistence images deform the  $\text{POT}_1$  geometry through two distinct mechanisms: kernel-induced saturation and persistence-dependent reweighting. The first effect is already visible at the level of a single Gaussian atom, before any additional weighting is introduced.

Strictly speaking, persistence images are defined by first forming a *persistence surface* on the birth-persistence plane and then integrating that surface over the boxes of a chosen grid, typically on a relevant subdomain. Thus the exact construction involves both truncation and discretization. Since our goal here is only to isolate the underlying geometric mechanism, we work instead on the whole space  $\mathbb{R}^2$ , ignoring boundary and discretization effects. This keeps the computations explicit while still capturing the relevant qualitative behavior, especially when the chosen window is large enough that the Gaussian tails outside it are negligible. See Adams et al. (2017) for the original persistence-surface and persistence-image construction. Let  $g_p^\sigma$  denote the isotropic Gaussian centered at  $p$  with bandwidth  $\sigma$ ,

$$g_p^\sigma(z) = \frac{1}{2\pi\sigma^2} \exp\left(-\frac{\|z - p\|^2}{2\sigma^2}\right), \quad z \in \mathbb{R}^2.$$

For arbitrary  $p, q \in X$ , a direct computation gives

$$\|g_p^\sigma - g_q^\sigma\|_{L^2(\mathbb{R}^2)}^2 = \|g_p^\sigma\|_{L^2}^2 + \|g_q^\sigma\|_{L^2}^2 - 2\langle g_p^\sigma, g_q^\sigma \rangle,$$

with

$$\|g_p^\sigma\|_{L^2(\mathbb{R}^2)}^2 = \frac{1}{4\pi\sigma^2}, \quad \langle g_p^\sigma, g_q^\sigma \rangle = \frac{1}{4\pi\sigma^2} \exp\left(-\frac{\|p-q\|^2}{4\sigma^2}\right).$$

Hence

$$\|g_p^\sigma - g_q^\sigma\|_{L^2(\mathbb{R}^2)}^2 = \frac{1}{2\pi\sigma^2} \left(1 - \exp\left(-\frac{\|p-q\|^2}{4\sigma^2}\right)\right),$$

or equivalently

$$\|g_p^\sigma - g_q^\sigma\|_{L^2(\mathbb{R}^2)} = \frac{1}{\sqrt{2\pi}\sigma} \left(1 - \exp\left(-\frac{\|p-q\|^2}{4\sigma^2}\right)\right)^{1/2}.$$

Thus the image-space distance is an increasing function of  $\|p-q\|$ , but it does not grow indefinitely: once the overlap between the two Gaussians becomes negligible, it saturates at the finite level

$$\frac{1}{\sqrt{2\pi}\sigma}.$$

To relate this to  $\text{POT}_1$ , consider now a moving one-point diagram

$$D_k := \{p_k\}, \quad p_k := p + k v, \quad D' := \{q\}, \quad k \geq 0,$$

where  $v$  is a unit vector compatible with the upper-half-plane constraint. In Figure 3b we take

$$p = (100, 201), \quad q = (100, 200), \quad v = \frac{1}{\sqrt{2}}(1, 1).$$

Applying the formula above with  $p = p_k$  and  $q$  fixed, we see that the persistence-image distance between  $D_k$  and  $D'$  is governed only by Gaussian overlap, and therefore stabilizes at the kernel scale  $(2\pi)^{-1/2}\sigma^{-1}$  as  $k \rightarrow \infty$ .

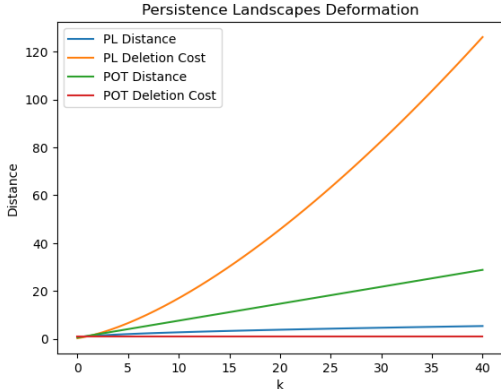
This already produces a characteristic mismatch with  $\text{POT}_1$ . In the one-point setting, the  $\text{POT}_1$  distance between  $D_k$  and  $D'$  grows with  $k$  until deletion to the diagonal becomes preferable, so its natural flattening scale is set by persistence. By contrast, the persistence-image distance flattens at the fixed kernel scale  $(2\pi)^{-1/2}\sigma^{-1}$ , independently of how large the corresponding deletion scale is in  $\text{POT}_1$ . For fixed  $\sigma$ , this discrepancy becomes more pronounced as the points move farther from the diagonal.

An even stronger distortion appears when one compares a point directly with the zero diagram. Without persistence-based weighting, deletion to zero is represented simply by the  $L^2$ -mass of the Gaussian atom:

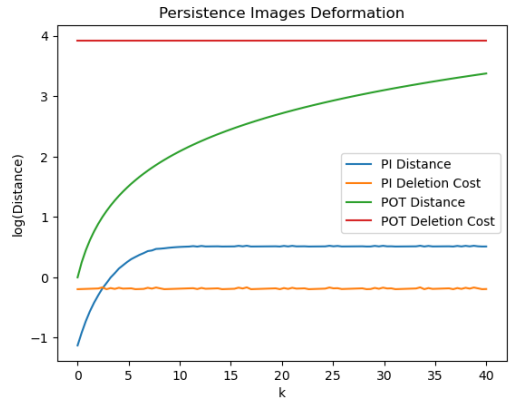
$$\|g_{p_k}^\sigma\|_{L^2(\mathbb{R}^2)} = \frac{1}{2\sqrt{\pi}\sigma},$$

again up to the truncation and discretization effects of the actual image representation. In other words, once the Gaussian is sufficiently far from the diagonal, its deletion cost is essentially set by the kernel normalization alone, rather than by the persistence of the point. This can severely undershoot the true transport cost: high-persistence points are deleted at almost the same image cost as lower-persistence ones.

A persistence-dependent weighting can partially compensate for this effect, but only by introducing a second deformation of the geometry. If one weights each atom by a function of persistence, then high-persistence points receive larger amplitudes, so deletion costs can be made to grow more in line with  $\text{POT}_1$ . But this comes at the price of an explicit persistence bias, analogous in spirit to the high-persistence emphasis observed for persistence landscapes. On the other hand, a weight that stays essentially flat away from



(a) **Persistence landscapes.** One-point toy examples illustrating the deformation induced by landscapes. Moving  $D_k = \{p_k\}$  along the anti-diagonal increases its persistence, and the corresponding landscape contribution grows quadratically in  $k$ . The plot also shows that, for two one-point diagrams  $D_k = \{p_k\}$  and  $D'_k = \{q_k\}$  drifting in the same anti-diagonal direction, the distance between the associated landscapes grows linearly in  $k$ .



(b) **Persistence images.** One-point toy example illustrating the deformation induced by Gaussian persistence images. As  $D_k = \{p_k\}$  moves in the diagonal direction, the  $L^2$  distance between the corresponding Gaussian atom and that of  $D' = \{q\}$  increases at first but then saturates at a kernel-dependent ceiling. Thus, for fixed bandwidth  $\sigma$ , the persistence-image distance stabilizes much earlier than the corresponding  $\text{POT}_1$  scale when the deletion cost is large. The vertical axis, representing the relevant distances, is displayed on a logarithmic scale.

Figure 3: Two elementary mechanisms by which standard topological summaries deform the  $\text{POT}_1$  geometry. Persistence landscapes amplify variability at high persistence, while Gaussian persistence images induce a kernel-dependent saturation of pairwise distances. In the latter case, for fixed bandwidth  $\sigma$ , the discrepancy with  $\text{POT}_1$  becomes more pronounced at high persistence, since the persistence-image distance saturates at a fixed kernel scale whereas the  $\text{POT}_1$  flattening occurs only at the much larger deletion scale determined by the sum of the persistences.

the diagonal avoids that bias, but then the deletion cost remains tied to the Gaussian mass and can dramatically underestimate transport to the diagonal.

Thus the deformation induced by persistence images is not just the saturation of pairwise distances. More fundamentally, the representation struggles to encode deletion costs at the correct scale. Without persistence-based weighting, deletion can be severely underestimated; with such weighting, one recovers a more realistic scale only by imposing a strong persistence bias.

#### 9.4 Take-home message

These examples illustrate a general point: all topological summaries deform the  $\text{POT}_1$  geometry, and each therefore introduces its own geometric bias into downstream analyses. From this viewpoint, having a broader repertoire of summaries is valuable, especially when some of them, as in the case of persistence spheres, come with explicit guarantees on their relation to the original diagram geometry. At the same time, understanding the specific deformation mechanism of each summary helps interpret empirical results, since part of

the observed variability may come not only from the data, but also from the way the chosen representation emphasizes, suppresses, or reshapes different types of variation.

## 10. Unsupervised Simulations

In this section we investigate how the qualitative geometric mechanisms discussed in Section 9 manifest themselves in practice. We focus on unsupervised settings, where the geometry induced by the chosen summary has a more direct impact on the analysis than in supervised tasks, where part of the bias may be absorbed by the downstream learner.

A second point concerns optional preprocessing. Although persistence spheres do not require any parameter to be well defined or stable, one may still reweight or smooth a diagram as a separate preprocessing step, for instance to mitigate noise. More generally, this possibility is available for all measure-based representations, and may be useful in unsupervised settings where there is no predictive model to automatically downweight irrelevant topological information. For this reason, besides comparing the summaries themselves, we also examine how optional reweighting choices affect the resulting unsupervised behavior.

### 10.0.1 FDA

We first consider an unsupervised simulation based on a standard functional data analysis (FDA) generative model (Ramsay and Silverman, 2005), adapted from Pegoraro (2026). The purpose is to construct a regime in which a strong bias toward high-persistence features is actually advantageous: the class signal is primarily carried by the largest oscillations of the underlying smooth functions, while noise mostly produces smaller-scale topological clutter. Representative samples from the two FDA setups are shown in Figure 4.

**Generative model.** We first construct two smooth random functions  $f_1, f_2 : [0, 1] \rightarrow \mathbb{R}$  by cubic-spline interpolation of random values on a regular grid. Let  $0 = t_1 < \dots < t_m = 1$  be a uniform grid with  $m = 40$  points. For each class  $c \in \{1, 2\}$ , we sample independently

$$u_j^{(c)} \sim \text{Unif}([-50, 50]), \quad j = 1, \dots, m,$$

and define  $f_c$  as the cubic spline interpolant of  $\{(t_j, u_j^{(c)})\}_{j=1}^m$ .

Given a noise level  $\sigma \in \{10, 15, 20\}$ , we generate  $N = 50$  noisy realizations from each class as follows. For each replicate  $i = 1, \dots, N$  and class  $c \in \{1, 2\}$ , we first sample an integer

$$n_i^{(c)} \sim \text{Unif}\{200, \dots, 800\},$$

then sample locations

$$X_{i,1}^{(c)}, \dots, X_{i,n_i^{(c)}}^{(c)} \stackrel{\text{i.i.d.}}{\sim} \text{Unif}([0, 1]),$$

and finally observe noisy values

$$Y_{i,\ell}^{(c)} = f_c(X_{i,\ell}^{(c)}) + Z_{i,\ell}^{(c)}, \quad Z_{i,\ell}^{(c)} \stackrel{\text{i.i.d.}}{\sim} \mathcal{N}(0, (\sigma/3)^2), \quad \ell = 1, \dots, n_i^{(c)}.$$

Thus the parameter  $\sigma$  corresponds to a “ $3\sigma$ ” noise amplitude. Each noisy curve is encoded as a 0-dimensional persistence diagram, computed from the sublevel-set filtration of the piecewise-linear interpolation of the sampled points  $\{(X_{i,\ell}^{(c)}, Y_{i,\ell}^{(c)})\}_{\ell=1}^{n_i^{(c)}}$ .

The randomization of the sample size  $n_i^{(c)}$  in the interval  $[200, 800]$  is deliberate. Larger values of  $n_i^{(c)}$  create more spurious local oscillations, so the amount of noise-induced topological clutter becomes highly unbalanced across statistical units. This is particularly

unfavorable to  $\text{POT}_1$  and to summaries that remain sensitive to low-persistence structure. Conversely, summaries with a strong bias toward high persistence may benefit precisely because they suppress this imbalance. Typical realizations are displayed in Figure 4a.

For each method, we compute the pairwise distance matrix between diagrams using  $\text{POT}_1$ , SW, and the distances induced by persistence spheres (PSphs), persistence landscapes (PLs), persistence images (PIs), and persistence splines (PSpls). We then apply hierarchical clustering with average linkage, cut the dendrogram into two clusters, and evaluate the resulting partition via the Rand index. All reported values are means and standard deviations over 100 independent runs.

**Four scenarios.** We consider four FDA simulations.

**(i) Baseline FDA simulation.** We use the generative model above with variable sample size  $n_i^{(c)} \sim \text{Unif}\{200, \dots, 800\}$  and compare the methods in their standard configurations. For persistence images we use persistence as weight; persistence spheres are used without reweighting. This setup is designed to favor summaries that emphasize high-persistence features.

**(ii) FDA simulation with persistence-squared reweighting.** We keep exactly the same generative model, but reweight the diagram measures by  $\text{Pers}(\cdot)^2$  before applying persistence images and persistence spheres. This tests directly whether an even stronger emphasis on high persistence improves performance. If so, it supports the interpretation that the strong results of persistence landscapes in (i) are driven by their bias toward high-persistence variability.

**(iii) FDA simulation with step reweighting.** Again we keep the same generative model, but now use the simple denoising-type weight

$$w(x, y) = \frac{2}{\pi} \arctan\left(\frac{y - x}{\sigma}\right),$$

which vanishes on the diagonal and rapidly saturates to 1 away from it. This is meant to mimic a basic “remove small lifetimes” strategy. Here we deliberately use the true noise scale  $\sigma$  from the generative model, so as not to confound the comparison with the additional problem of estimating a threshold parameter, which is not the point of the present simulation. Comparing (ii) and (iii) helps separate generic near-diagonal denoising from a genuine preference for high-persistence features.

**(iv) FDA simulation against high-persistence bias.** We finally modify the generative model so as to turn the landscape bias against itself. For both classes, when sampling the smooth function, we fix the first four control-point values to

$$(-100, 100, -100, 100),$$

while the remaining control-point values are still sampled uniformly from  $[-50, 50]$ . Hence both classes share two very large oscillations, so the variability introduced by those high-persistence features is no longer discriminative. Moreover, we fix  $n = 200$  for every statistical unit, thereby removing the noise-imbalance confounding factor present in (i)–(iii). This simulation is designed to show that, once very persistent features cease to carry class information, a strong bias toward them can become detrimental. Typical realizations for this modified setup are shown in Figure 4b.

**Parameter choices.** We use  $\text{POT}_1$  without parameters and approximate sliced Wasserstein using 50 random lines, as in the default GUDHI implementation. Persistence spheres are evaluated on a polar grid on  $\mathbb{S}^2$  with  $100 \times 200$  samples (latitude  $\times$  longitude). For

Table 1: **FDA unsupervised simulations (i)–(iii)**. Mean  $\pm$  standard deviation of Rand index over 100 independent runs. Since only persistence images (PI) and persistence spheres (PSph) change across scenarios (i)–(iii), the values of POT<sub>1</sub>, SW, PL, and PSpl are reported only once for each noise level.

$\sigma$	Shared across (i)–(iii)				(i) Baseline		(ii) Pers <sup>2</sup>		(iii) Step	
	POT <sub>1</sub>	SW	PL	PSpl	PI	PSph	PI	PSph	PI	PSph
10	0.760 $\pm$ 0.228	0.527 $\pm$ 0.044	<b>0.984 <math>\pm</math> 0.086</b>	0.964 $\pm$ 0.111	0.783 $\pm$ 0.238	0.530 $\pm$ 0.076	0.958 $\pm$ 0.129	0.762 $\pm$ 0.206	0.933 $\pm$ 0.163	0.672 $\pm$ 0.200
15	0.631 $\pm$ 0.152	0.522 $\pm$ 0.039	<b>0.949 <math>\pm</math> 0.140</b>	0.771 $\pm$ 0.238	0.581 $\pm$ 0.165	0.512 $\pm$ 0.045	0.867 $\pm$ 0.202	0.700 $\pm$ 0.188	0.554 $\pm$ 0.122	0.565 $\pm$ 0.130
20	0.547 $\pm$ 0.068	0.526 $\pm$ 0.048	<b>0.846 <math>\pm</math> 0.218</b>	0.641 $\pm$ 0.215	0.527 $\pm$ 0.053	0.502 $\pm$ 0.010	0.812 $\pm$ 0.214	0.642 $\pm$ 0.163	0.523 $\pm$ 0.050	0.513 $\pm$ 0.027

persistence landscapes, we retain all landscape functions and compute distances exactly in  $L^2$ . For persistence splines, we use a  $20 \times 20$  grid and 100 iterations with stopping tolerance  $10^{-10}$ , in line with Dong et al. (2024). For persistence images, we set the pixel size to  $1/500$  of the minimum side length of the smallest axis-aligned rectangle supporting the diagrams, rounded to the closest power of 10, and take the Gaussian bandwidth equal to 10 times the pixel size. In scenarios (ii) and (iii), the stated reweightings are applied only to persistence images and persistence spheres.

**Results.** The results for scenarios (i)–(iii), which share the same generative process, are reported in Table 1; scenario (iv) is reported separately in Table 2.

In the baseline simulation (i), persistence landscapes clearly dominate at all noise levels, with mean Rand index 0.984, 0.949, and 0.846 for  $\sigma = 10, 15, 20$ , respectively. This strongly suggests that their high-persistence bias is favorable in this regime, where the class signal is carried mainly by the largest oscillations while variable sample size introduces abundant, highly unbalanced low-persistence clutter. Persistence splines also perform well at low noise, while POT<sub>1</sub>, SW, PSph, and PI are substantially less competitive.

Scenario (ii) confirms this interpretation. Reweighting by Pers<sup>2</sup> markedly improves both PI and PSph, especially PI. Thus the success of PL in scenario (i) cannot be explained only by generic robustness to near-diagonal noise: in this FDA regime, a strong emphasis on high persistence is itself beneficial.

Scenario (iii) separates this effect from simple thresholding. The step weight suppresses small lifetimes, but performs clearly worse than Pers<sup>2</sup>-reweighting, especially for moderate and large noise. This shows that removing low-persistence points is not enough: here it is specifically advantageous to bias the geometry toward the largest topological features.

Scenario (iv) reverses the picture. Once the two classes share the largest oscillations and the sample size is fixed at  $n = 200$ , the strong high-persistence bias of PL becomes detrimental, and PL drops to essentially random performance. In contrast, POT<sub>1</sub> becomes the best method overall, with mean Rand index 0.975, 0.907, and 0.888 for  $\sigma = 10, 15, 20$ . PI, still using persistence as weight, remains strong, plausibly because its bias toward high persistence is milder than that of PL and can still help linearize POT<sub>1</sub> while damping part of the lower-persistence noise. PSph also improves relative to scenario (i), consistently with the removal of the sample-size imbalance effect.

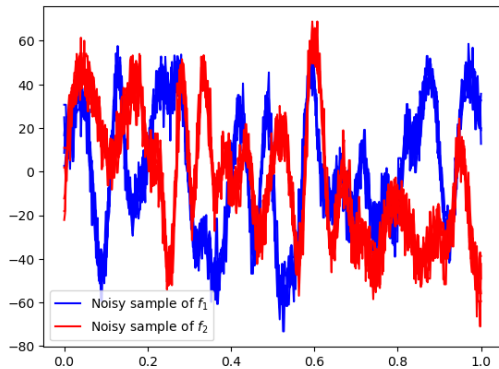
Overall, these simulations show that the geometric bias induced by a topological summary can be highly consequential in unsupervised settings. This makes it important not only to compare empirical performance, but also to understand which persistence scales a given summary tends to emphasize or suppress.

## 10.0.2 POINT PROCESSES

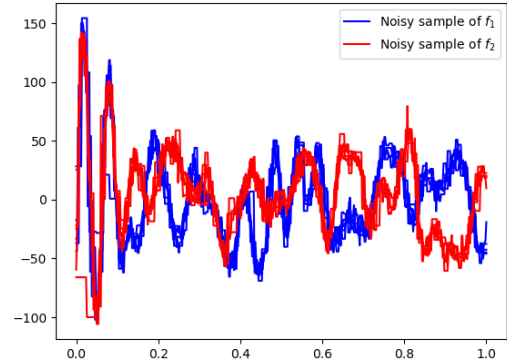
We next turn to a benchmark in which the relevant signal is expected to be much less concentrated at the highest persistence scales. To evaluate whether topological summaries

Table 2: **FDA unsupervised simulation (iv)**. Mean  $\pm$  standard deviation of Rand index over 100 independent runs for scenario (iv), where the two classes share the largest oscillations and the sample size is fixed to  $n = 200$ .

$\sigma$	POT <sub>1</sub>	SW	PSph	PL	PI	PSpl
10	<b>0.975 <math>\pm</math> 0.107</b>	0.616 $\pm$ 0.172	0.641 $\pm$ 0.186	0.515 $\pm$ 0.071	0.795 $\pm$ 0.240	0.496 $\pm$ 0.001
15	<b>0.907 <math>\pm</math> 0.191</b>	0.625 $\pm$ 0.181	0.653 $\pm$ 0.195	0.518 $\pm$ 0.081	0.753 $\pm$ 0.243	0.496 $\pm$ 0.003
20	<b>0.888 <math>\pm</math> 0.205</b>	0.650 $\pm$ 0.191	0.645 $\pm$ 0.190	0.511 $\pm$ 0.054	0.704 $\pm$ 0.240	0.496 $\pm$ 0.002



(a) Noisy functions sampled from the model used in scenarios (i)–(iii).



(b) Noisy functions sampled from the model used in scenario (iv), with the first two large oscillations shared across the classes.

Figure 4: **FDA simulations**. Left: realizations from the baseline generative model used in scenarios (i)–(iii), where the discriminative signal is more likely to be carried by large oscillations while noise induces abundant low-persistence clutter. Right: realizations from scenario (iv), where the largest oscillations are shared across the two classes, so that an excessive bias toward high-persistence features becomes detrimental.

extracted from persistence diagrams can detect differences in spatial interaction structure, we consider four families of planar point processes exhibiting distinct behaviors (complete spatial randomness, mild clustering, inhibition, and regularity) and sample point clouds on a square observation window

$$\mathcal{W} = [0, L]^2 \subset \mathbb{R}^2.$$

For each family we generate 30 independent point clouds and aim to recover the generating process via unsupervised clustering of their topological summaries.

Unlike the FDA simulations above, this setup is not designed to reward a strong bias toward the most persistent topological features. For spatial point processes at comparable density, much of the relevant information is carried by low- and medium-persistence structure, since local interaction patterns first affect short- and intermediate-scale connectivity and loop formation. Accordingly, summaries with too strong a high-persistence bias may become disadvantageous. This motivates, in particular, the persistence-image choices used below: we employ weights that retain sensitivity to lower-persistence features rather than amplifying only the largest lifetimes.

Throughout, we construct for each model a point cloud of common target cardinality  $n$  in  $\mathcal{W}$ , which mitigates the confounding effect of varying sample size in persistence and focuses the comparison on interaction structure. We then compute Vietoris–Rips persistence diagrams in homological degrees 0 and 1, compute pairwise distances using the same

family of methods as above, and cluster the resulting samples using hierarchical clustering with average linkage. Finally, we cut the dendrogram into four clusters and compare the obtained partition to the ground-truth family labels. Background on spatial point processes may be found in Diggle (2013); Illian et al. (2008); Møller and Waagepetersen (2004).

### Point-process families

- (i) **Homogeneous Poisson (CSR).** As a baseline we use complete spatial randomness (CSR): conditional on a fixed sample size  $n$ , this corresponds to i.i.d. points uniformly distributed on  $\mathcal{W}$ . This model has no inter-point interaction and is a canonical null in spatial statistics (Diggle, 2013; Illian et al., 2008).
- (ii) **Thomas (Neyman–Scott) cluster process.** To model mild aggregation we use a Thomas process, a classical Neyman–Scott cluster model (Thomas, 1949; Møller and Waagepetersen, 2004). Parents are sampled uniformly in  $\mathcal{W}$ ; each parent generates a Poisson number of offspring; offspring are displaced from their parent by an isotropic Gaussian perturbation. The resulting pattern exhibits clustering at short-to-intermediate scales while remaining approximately Poisson at larger scales.
- (iii) **Matérn type-II hard-core process.** To represent inhibition, we use a Matérn type-II hard-core process obtained by thinning of a Poisson candidate set in  $\mathcal{W}$ , equipped with i.i.d. *marks* (Matérn, 1960, 1986; Møller and Waagepetersen, 2004). Here a *mark* is an auxiliary random variable attached to each candidate point (in our case  $U \sim \text{Unif}(0, 1)$ ), independent across points and independent of the candidate locations. The parameter  $r_{\text{hc}} > 0$  is the *hard-core distance*: it specifies an exclusion radius enforcing short-range repulsion. Concretely, given a candidate point  $y$  with mark  $U_y$ , we retain  $y$  if its mark is the smallest among all candidates within distance  $r_{\text{hc}}$ , i.e.,

$$U_y = \min\{U_z : z \in Y \cap B(y, r_{\text{hc}})\}.$$

This rule ensures that among any pair of candidates separated by less than  $r_{\text{hc}}$ , at most one can survive.

- (iv) **Jittered lattice.** Finally, we consider a jittered lattice on  $\mathcal{W} = [0, L]^2$ . We partition  $\mathcal{W}$  into a regular  $k \times k$  grid of congruent square cells of side length  $L/k$  (with  $k^2 \geq n$ ), select  $n$  cells uniformly without replacement, and draw one point from each selected cell by applying a bounded random displacement (“jitter”) within the cell. This provides a controlled regularity baseline: the “one point per cell” constraint suppresses extremely small inter-point distances relative to CSR, mimicking a mild repulsive effect while being governed by a single interpretable jitter parameter.

**Sampling schemes.** For CSR and the jittered lattice design the construction yields  $|X| = n$  by definition. For the Thomas and Matérn type-II models, the underlying point process has random cardinality; we therefore apply a simple conditioning procedure to obtain  $n$  points in  $\mathcal{W}$ .

- (i) **CSR.** Sample  $x_1, \dots, x_n \stackrel{\text{i.i.d.}}{\sim} \text{Unif}(\mathcal{W})$ .
- (ii) **Thomas cluster model (parameters:  $n_{\text{par}}, \lambda_{\text{off}}, \sigma$ ).** Sample  $n_{\text{par}}$  parent locations  $p_1, \dots, p_{n_{\text{par}}} \stackrel{\text{i.i.d.}}{\sim} \text{Unif}(\mathcal{W})$ . Initialize an empty offspring set  $X = \emptyset$ . While  $|X| <$

$n$ , choose an index  $J \sim \text{Unif}\{1, \dots, n_{\text{par}}\}$ , draw  $K \sim \text{Poisson}(\lambda_{\text{off}})$ , and generate candidate offspring

$$p_J + \xi_\ell, \quad \ell = 1, \dots, K, \quad \xi_\ell \stackrel{\text{i.i.d.}}{\sim} \mathcal{N}(0, \sigma^2 I_2).$$

Candidates falling outside  $\mathcal{W}$  are discarded, and all remaining points are appended to  $X$ . If the same parent index  $J$  is selected multiple times, multiple independent offspring batches are generated around  $p_J$  and accumulated in  $X$ . Finally, if  $|X| > n$ , we subsample uniformly without replacement to obtain exactly  $n$  points.

- (iii) **Matérn type-II hard-core model (parameters:  $m, r_{\text{hc}}$ ).** Generate a Poisson candidate set  $Y = \{y_1, \dots, y_M\} \subset \mathcal{W}$  with  $M \sim \text{Poisson}(m)$ , and attach i.i.d. marks  $U_{y_i} \stackrel{\text{i.i.d.}}{\sim} \text{Unif}(0, 1)$  independent of  $Y$ . Given a hard-core distance  $r_{\text{hc}} > 0$ , retain a candidate  $y \in Y$  if it has the smallest mark within its  $r_{\text{hc}}$ -neighborhood, i.e.  $U_y = \min\{U_z : z \in Y \cap B(y, r_{\text{hc}})\}$ . Denote by  $Y_{\text{hc}}$  the retained set. If  $|Y_{\text{hc}}| \geq n$  we select  $n$  points uniformly without replacement from  $Y_{\text{hc}}$ . If  $|Y_{\text{hc}}| < n$ , we discard the realization, update  $m \leftarrow 1.5m$ , and resimulate until  $|Y_{\text{hc}}| \geq n$ .
- (iv) **Jittered lattice (parameters:  $k, \rho_{\text{jitt}}$ ).** Choose  $k = \lceil \sqrt{n} \rceil$  and partition  $\mathcal{W}$  into  $k^2$  congruent square cells of side length  $L/k$ . Select  $n$  distinct cells uniformly without replacement. From each selected cell  $C$  draw one point by sampling a bounded random displacement around the cell center  $c(C)$ :

$$x = c(C) + \delta, \quad \delta \sim \text{Unif}\left(\left[-\frac{\rho_{\text{jitt}}}{2} \frac{L}{k}, \frac{\rho_{\text{jitt}}}{2} \frac{L}{k}\right]^2\right),$$

where  $\rho_{\text{jitt}} \in [0, 1]$  controls the jitter amplitude as a portion of the cell. Thus  $\rho_{\text{jitt}} = 0$  yields deterministic cell centers, while  $\rho_{\text{jitt}} = 1$  yields a uniform draw over the entire cell. By construction, this produces a point cloud with one point per selected cell.

**Parameter choices.** Our goal is to construct a challenging clustering case study from degree-0 and degree-1 persistence diagrams, in the sense that separation should not be dominated by extreme aggregation or regularity. To make the interaction effects comparable across models, we scale all length parameters using the typical spacing

$$s := \sqrt{\frac{|\mathcal{W}|}{n}} = \frac{L}{\sqrt{n}},$$

which is the side length of a square of area  $|\mathcal{W}|/n$ . In our experiments we fix  $n = 200$  and  $L = 1000$ . These values strike a practical balance between (i) enough geometric complexity to produce informative topological features, (ii) feasible computational cost for Vietoris–Rips persistence, and (iii) numerical stability, by avoiding extremely small coordinate differences that may amplify floating-point effects.

- (i) **CSR.** No additional parameters are required beyond the target cardinality  $n$  and the window size  $L$ .
- (ii) **Thomas cluster model.** We fix the Gaussian cluster spread to

$$\sigma = 0.9s,$$

so that offspring clouds overlap at the spacing scale and clustering is intentionally mild. This reduces the prevalence of extremely short edges and very early merges

in degree-0 persistent homology compared to strongly clustered regimes ( $\sigma \ll s$ ), thereby making CSR versus clustering less trivial and leaving more discriminative signal to higher-order effects, including loop formation and filling summarized by degree-1 persistent homology. For the remaining Thomas parameters we set

$$n_{\text{par}} = \lceil \sqrt{n} \rceil, \quad \lambda_{\text{off}} = \frac{n}{n_{\text{par}}},$$

so that the expected number of generated offspring before boundary rejection is approximately  $n$  and neither the “few large clusters” nor the “many tiny clusters” regime dominates.

- (iii) **Matérn type-II hard-core model.** We choose the hard-core distance as a moderate fraction of the spacing,

$$r_{\text{hc}} = 0.5 s,$$

so that inhibition is primarily visible through a depletion of very small inter-point distances, without producing near-lattice configurations. For the Poisson candidate mean we set

$$m = 3n,$$

which oversamples candidates to compensate for Matérn-II thinning; if a realization yields fewer than  $n$  retained points, we increase  $m$  geometrically (by a fixed multiplicative factor of 1.5) and resimulate until at least  $n$  points are obtained.

- (iv) **Jittered lattice.** We set

$$k = \lceil \sqrt{n} \rceil, \quad \rho_{\text{jitt}} = 0.75,$$

where  $\rho_{\text{jitt}} \in [0, 1]$  controls the jitter amplitude as a proportion of the cell. The choice  $\rho_{\text{jitt}} = 0.75$  avoids both extremes: nearly deterministic cell centers ( $\rho_{\text{jitt}} \approx 0$ ) and nearly uniform-in-cell sampling ( $\rho_{\text{jitt}} \approx 1$ ). Consequently, the “one point per selected cell” constraint still suppresses the smallest inter-point distances relative to CSR, but the random displacement blurs the grid sufficiently that the resulting persistence summaries overlap substantially with those of CSR and of mild hard-core processes.

Finally, when building the Vietoris–Rips filtration we cap the diameter parameter as  $7.0 s$ . To motivate this choice, note that  $s^2$  is the area available per point in an  $n$ -point configuration on  $\mathcal{W}$ . Equivalently,  $s$  is the grid spacing of the regular  $l \times l$  lattice with  $l^2 = n$  points filling  $\mathcal{W}$ . Thus  $s$  provides a canonical unit for inter-point distances at the given density. In the Vietoris–Rips complex, edges appear at scale  $r$  between pairs of points at Euclidean distance at most  $r$ ; taking  $r$  to be a moderate multiple of  $s$  therefore probes neighborhoods containing a controlled (density-dependent) number of points. In particular, for a homogeneous configuration of intensity  $n/|\mathcal{W}|$ , the expected number of neighbors of a typical point within radius  $r$  is approximately

$$\frac{n}{|\mathcal{W}|} \pi r^2 = \pi \left( \frac{r}{s} \right)^2,$$

ignoring boundary effects. Hence setting  $r = 7s$  yields an expected number of neighbors of about  $\pi \cdot 7^2 \approx 154$  in the underlying proximity graph, amounting to roughly 75% of the sample for  $n = 200$ .

**Distances and topological-summary parameters.** For  $\text{POT}_1$  no parameter is required. For SW, we approximate the metric using 50 random lines, which is the default choice in the GUDHI implementation. PSphs are evaluated on a polar grid on  $\mathbb{S}^2$  with  $100 \times 200$  samples (latitude  $\times$  longitude). For PLs, we retain all landscape functions and compute pairwise distances exactly using the  $L^2$ -norm. For PSpls, we use a  $20 \times 20$  grid and 100 iterations, with a stopping tolerance  $10^{-10}$  for the iterative procedure; these values follow the supervised case studies reported in Dong et al. (2024).

For PIs, we set the pixel size to  $s/100$  and the Gaussian kernel bandwidth to  $s/10$ , where  $s = L/\sqrt{n}$  is the typical spacing of the point clouds. In this PP scenario, where low- and medium-persistence features are expected to be informative, we again a step weight to avoid over-emphasizing the largest persistence values, namely

$$w(x, y) = \frac{2}{\pi} \arctan(y - x).$$

We also tested the linear weight  $w(x, y) = y - x$  and observed similar results. In addition, for  $H_0$  diagrams only, when computing persistence images we add an artificial point on the diagonal at coordinates  $(s/10, s/10)$ , so that the birth coordinates are not all identically equal to 0; otherwise the resulting PI would degenerate to a one-dimensional object rather than a genuine two-dimensional image. These PI parameters were chosen by testing a small set of candidates on smaller datasets generated from the same models and then freezing the configuration for the clustering experiments.

**Results.** Tables 3 and 4 report, respectively, clustering performance on the PP benchmark and the empirical agreement of each distance with  $\text{POT}_1$ .

In terms of Rand index (Table 3),  $\text{POT}_1$ , SW, and PSph perform comparably in  $H_0$ , with means 0.859, 0.859, and 0.858, respectively. In  $H_0$ , however, PI is the clear winner, reaching a mean Rand index of 0.950, well above all other methods. In  $H_1$ , SW attains the best mean performance (0.873), with  $\text{POT}_1$  very close behind (0.872) and with overlapping confidence intervals; PSph remains very competitive (0.861), whereas PL and PSpl are substantially worse in both degrees.

As in the other benchmarks, there is no particular reason to expect SW to outperform  $\text{POT}_1$  systematically; any small advantage is plausibly due to the numerical approximation with 50 random lines together with the downstream clustering pipeline. We also stress that, unlike the linearizations below, SW remains a distance rather than a vectorization.

Among the distances induced by linearized representations, PSph is again the most faithful to  $\text{POT}_1$ ; see Table 4. Its correlation with  $\text{POT}_1$  is 0.935, substantially above PL (0.822), PI (0.886), and PSpl (0.527). This is consistent with the clustering results: PSph stays close to  $\text{POT}_1$  in both  $H_0$  and  $H_1$ , whereas PSpl performs poorly both in clustering and in correlation, suggesting that its induced geometry is much less aligned with that of  $\text{POT}_1$  in this regime.

The behavior of PL and PI is particularly informative when compared with the FDA simulations (i)–(iii). There, summaries with a strong bias toward high persistence, especially PL, were favored because the discriminative signal was largely carried by the largest oscillations. Here the situation is different. Since low- and medium-persistence features carry relevant information about local spatial interaction, summaries with a strong high-persistence bias can discard too much signal. Coherently with this intuition, PL performs poorly in both homological degrees, with mean Rand index around 0.60 in  $H_0$  and 0.63 in  $H_1$ . By contrast, PI performs extremely well in  $H_0$ , plausibly because its milder and tunable bias is better matched to the relevant persistence scales in this regime.

Table 3: **PP unsupervised.** Mean  $\pm$  standard deviation of Rand index over 100 runs. Bold denotes the best mean in each row. A dagger  $\dagger$  marks methods whose 95% confidence interval for the mean (with  $n = 100$  runs) overlaps with that of the best method.

	POT <sub>1</sub>	SW	PSph	PL	PI	PSpl
$H_0$	0.859 $\pm$ 0.010	0.859 $\pm$ 0.010	0.858 $\pm$ 0.010	0.596 $\pm$ 0.052	<b>0.950 <math>\pm</math> 0.058</b>	0.283 $\pm$ 0.015
$H_1$	0.872 $\pm$ 0.006 $\dagger$	<b>0.873 <math>\pm</math> 0.009</b>	0.861 $\pm$ 0.013	0.630 $\pm$ 0.211	0.754 $\pm$ 0.019	0.285 $\pm$ 0.018

Table 4: **PP correlation.** Mean  $\pm$  standard deviation of the per-iteration, per-homological-degree correlation between POT<sub>1</sub> and each competing distance, computed over repeated runs. Since  $H_0$  and  $H_1$  are computed on the same data in each iteration, the two correlations within an iteration are not independent; accordingly, we only report descriptive statistics.

Method	Corr. with POT <sub>1</sub>
SW	0.996 $\pm$ 0.004
PSph	0.935 $\pm$ 0.055
PL	0.822 $\pm$ 0.071
PI	0.886 $\pm$ 0.092
PSpl	0.527 $\pm$ 0.102

Finally, the very high correlation of SW with POT<sub>1</sub> is expected: on persistence diagrams with uniformly bounded cardinality, SW is bi-Lipschitz equivalent to POT<sub>1</sub>, and should therefore track it closely up to multiplicative distortion. More broadly, this PP study complements the FDA one by showing that the usefulness of a given topological summary depends strongly on which persistence scales carry the relevant information.

## 11. Supervised Case Studies

We assess PSph on a collection of supervised regression and classification problems, comparing it with PI, PL, PSpl, SWK, and, whenever the sample size is sufficiently large, PersLay. For PSph, PI, PSpl, and PL we train random-forest classifiers or regressors, whereas SWK is paired with SVMs. Performance is measured through  $R^2$  in regression and accuracy in classification.

All case studies in this section are inherited from Pegoraro (2026), to which we refer for full details of the original benchmark design and implementation. In the present paper, we rerun only the PSph and PI pipelines: PSph is recomputed using the new definition introduced here, while PI is recomputed using improved parameter choices. The remaining baselines are reported unchanged from Pegoraro (2026). This allows for a direct comparison between the original weighted persistence-sphere construction, denoted here by PSph\*, and the new representation PSph.

### 11.0.1 DATASETS

We briefly summarize the supervised benchmarks inherited from Pegoraro (2026). Unless otherwise stated, we use the same train-test splits and cross-validation protocols as in that paper.

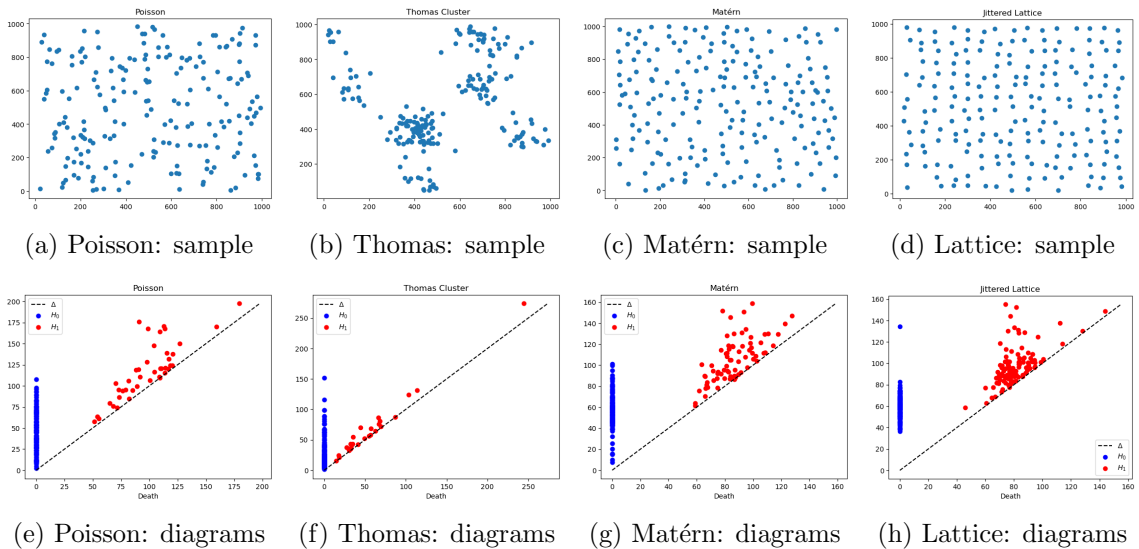


Figure 5: **PP simulation.** Top row: one simulated point pattern for each point process. Bottom row: corresponding persistence diagrams in degrees  $H_0$  (blue) and  $H_1$  (red). Ordering: Poisson, Thomas, Matérn, jittered lattice.

**“Eyeglasses” regression.** This synthetic regression task is built from the `eyeglasses` generator in `scikit-tda` (Saul and Tralie, 2019). One radius is fixed at 20, while the second is sampled from a Gaussian distribution with mean 10 and standard deviation 2.5, and serves as the regression target. We generate 2000 point clouds, compute their one-dimensional Vietoris–Rips persistence diagrams, and evaluate performance over 5 independent repetitions, each using a 70%–30% train–test split and threefold cross-validation on the training set.

**Functional datasets from `scikit-fda`.** We also consider the FDA benchmarks “Tecator”, “NO<sub>x</sub>”, and “Growth”, following the preprocessing used in Pegoraro (2026). In all three cases, zero-dimensional persistence diagrams are extracted from sublevel-set filtrations of the observed curves, and we use a 70%–30% train–test split with threefold cross-validation. For “Tecator”, the task is regression of fat content from derivatives of absorbance curves. For “NO<sub>x</sub>”, the task is to classify weekdays versus weekends from daily emission curves. For “Growth”, the task is to classify sex from derivatives of height trajectories.

**Classification benchmarks from Bandiziol and De Marchi (2024).** The datasets “DYN SYS”, “ENZYMES JACC”, “POWER”, and “SHREC14” are the same diagram-based classification benchmarks used in Pegoraro (2026), originally taken from Bandiziol and De Marchi (2024). We retain the same 70%–30% train–test split and threefold cross-validation protocol. These datasets cover a range of modalities, including point clouds, graphs, time series, and 3D shapes.

**“Human Poses” and “McGill 3D Shapes”.** The final two benchmarks are again inherited from Pegoraro (2026). For “Human Poses”, persistence diagrams are obtained from sublevel sets of the height function; for “McGill 3D Shapes”, they are obtained from an HKS-based filtration. Because each class contains only 10 samples, both datasets are evaluated with a fixed 80%–20% train–test split.

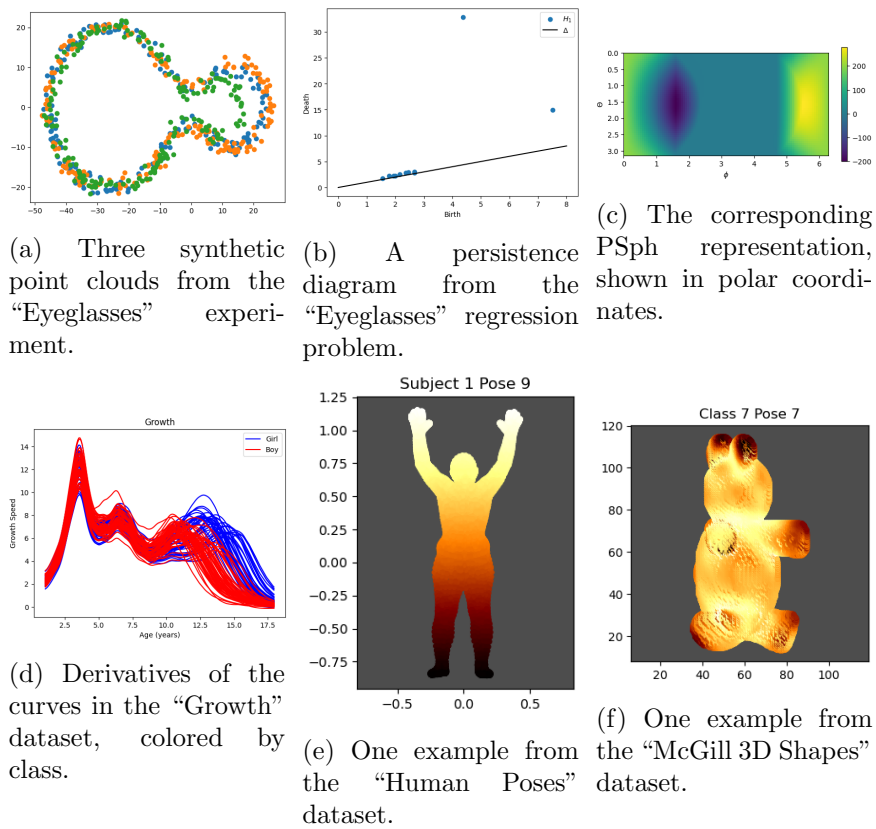


Figure 6: Examples of data, persistence diagrams, and PSph representations appearing in the supervised experiments of Section 11.

### 11.0.2 PARAMETER DETAILS

We summarize here the hyperparameters used for the vectorization and kernel baselines; PersLay architecture details are deferred to Pegoraro (2026).

For SWK we use SVM pipelines with precomputed kernels and regularization parameter

$$C \in \{10^{-3}, 10^{-2}, 10^{-1}, 1, 10, 10^2, 10^3, 10^4\}.$$

For random forests, the number of trees is selected in  $\{100, 200\}$ . All models are implemented with `scikit-learn` (Pedregosa et al., 2011).

**Parameters for topological summaries.** We now detail the hyperparameters used by the different vectorization methods. As in Pegoraro (2026), for PIs, PSpl, and PLs, support or range parameters are determined by inspecting the full dataset, independently of the train–test split. This introduces a mild inconsistency, although in practice it could be avoided by selecting sufficiently conservative bounds from the training sample alone. In contrast, PSphs are defined on a fixed compact domain, so no analogous preprocessing choice is required.

- **PSph:** PSphs are functions on  $\mathbb{S}^2$ , expressed in spherical coordinates and expanded in spherical harmonics (Müller, 2006) using `pyshtools` (Wieczorek and Meschede, 2018). This yields an orthonormal feature representation compatible with `scikit-learn`. Using a Driscoll–Healy grid (Driscoll and Healy, 1994) with  $2N_\theta$  latitudinal and  $4N_\theta$  longitudinal nodes, the resulting feature dimension is  $N_\theta^2/2$ . We cross-validate

$$2N_\theta \in \{30, 40, 50, 60, 70\}.$$

- **PI:** using `persim` from `scikit-tda`, we enclose all diagrams in a birth–persistence rectangle and set `pixel_size` by dividing the shortest side of this rectangle by a prescribed number  $N_{\text{pix}}$  of pixels per side. With the default Gaussian kernel, we set

$$\sigma = \text{pixel\_size}/N_\sigma, \quad N_\sigma \in \{1, 0.5, 0.1, 0.05, 0.01\},$$

so that smaller values of  $N_\sigma$  correspond to broader kernels. We also tune the persistence exponent in `weight_params` over

$$n \in \{1, 2, 4, 8\}.$$

The range of  $N_{\text{pix}}$  depends on the dataset family:

$$N_{\text{pix}} \in \{10, 100, 500\}$$

for the datasets inherited from Bandiziol and De Marchi (2024) and for “Human Poses”,

$$N_{\text{pix}} \in \{10, 100\}$$

for the “Eyeglasses” and the FDA datasets “Tecator”, “Growth”, and “NOx”, and

$$N_{\text{pix}} \in \{10, 50\}$$

for “McGill 3D Shapes”.

- **PL:** persistence landscapes are sampled on a common grid of 5000 points and then concatenated, with no additional hyperparameters.

Table 5: **Supervised case studies.** We report average  $R^2$  for regression and average accuracy for classification, across 5 runs for “Eyeglasses” and 10 runs for the remaining tasks. Values are reported as mean  $\pm$  standard deviation. PSph\* denotes the weighted persistence-sphere construction introduced in Pegoraro (2026). All benchmarks are taken from Pegoraro (2026); in the present paper, only the PSph and PI columns are recomputed, while the remaining columns are reported from that work. Bold entries indicate the best-performing method in each row. A dagger  $\dagger$  marks methods whose 95% confidence interval, computed using the appropriate number of repetitions for the corresponding row, overlaps with that of the best method.

	PSph	PSph*	PI	PL	PSpl	PersLay	SWK
<b>Regression</b>							
Eyeglasses	0.960 $\pm$ 0.004 $\dagger$	0.966 $\pm$ 0.003 $\dagger$	0.969 $\pm$ 0.006 $\dagger$	0.955 $\pm$ 0.018 $\dagger$	<b>0.971 <math>\pm</math> 0.011<math>\dagger</math></b>	0.248 $\pm$ 0.031	<b>0.971 <math>\pm</math> 0.003<math>\dagger</math></b>
Tecator	<b>0.973 <math>\pm</math> 0.007<math>\dagger</math></b>	0.969 $\pm$ 0.009 $\dagger$	0.940 $\pm$ 0.018	0.954 $\pm$ 0.011	<b>0.973 <math>\pm</math> 0.009<math>\dagger</math></b>	0.895 $\pm$ 0.029	0.953 $\pm$ 0.010
<b>Classification</b>							
Growth	<b>0.900 <math>\pm</math> 0.047<math>\dagger</math></b>	0.850 $\pm$ 0.052 $\dagger$	0.836 $\pm$ 0.056	0.768 $\pm$ 0.060	0.836 $\pm$ 0.043	0.807 $\pm$ 0.043	0.768 $\pm$ 0.058
NOx	0.863 $\pm$ 0.044 $\dagger$	<b>0.869 <math>\pm</math> 0.041<math>\dagger</math></b>	0.803 $\pm$ 0.043	0.789 $\pm$ 0.062	0.860 $\pm$ 0.058 $\dagger$	0.717 $\pm$ 0.078	0.840 $\pm$ 0.055 $\dagger$
DYN_SYS	0.809 $\pm$ 0.020	0.829 $\pm$ 0.028 $\dagger$	0.823 $\pm$ 0.028 $\dagger$	<b>0.840 <math>\pm</math> 0.024<math>\dagger</math></b>	0.791 $\pm$ 0.029	0.696 $\pm$ 0.044	0.828 $\pm$ 0.028 $\dagger$
ENZYMES_JACC	<b>0.391 <math>\pm</math> 0.025<math>\dagger</math></b>	0.349 $\pm$ 0.036	0.325 $\pm$ 0.061	0.377 $\pm$ 0.032 $\dagger$	0.362 $\pm$ 0.029 $\dagger$	0.243 $\pm$ 0.023	0.283 $\pm$ 0.055
POWER	<b>0.771 <math>\pm</math> 0.017<math>\dagger</math></b>	0.769 $\pm$ 0.021 $\dagger$	0.740 $\pm$ 0.017	0.756 $\pm$ 0.018 $\dagger$	0.734 $\pm$ 0.021	0.725 $\pm$ 0.038	0.767 $\pm$ 0.150 $\dagger$
SHREC14	0.920 $\pm$ 0.020 $\dagger$	0.931 $\pm$ 0.022 $\dagger$	0.938 $\pm$ 0.019 $\dagger$	<b>0.943 <math>\pm</math> 0.024<math>\dagger</math></b>	0.942 $\pm$ 0.015 $\dagger$	0.879 $\pm$ 0.018	0.886 $\pm$ 0.092 $\dagger$
Human Poses	0.540 $\pm$ 0.073	<b>0.640 <math>\pm</math> 0.077<math>\dagger</math></b>	0.515 $\pm$ 0.084	0.405 $\pm$ 0.106	0.560 $\pm$ 0.094 $\dagger$	-	0.345 $\pm$ 0.082
McGill 3D Shapes	<b>0.689 <math>\pm</math> 0.075<math>\dagger</math></b>	0.544 $\pm$ 0.085	0.667 $\pm$ 0.056 $\dagger$	0.678 $\pm$ 0.102 $\dagger$	0.656 $\pm$ 0.108 $\dagger$	-	0.567 $\pm$ 0.130 $\dagger$

- **PSpl:** following Dong et al. (2024), we use spline grids of size  $h^2$  with

$$h \in \{5, 10, 20, 40, 50\},$$

and otherwise keep the same parameter ranges as in Pegoraro (2026).

- **SWK:** we use the sliced Wasserstein kernel from gudhi (Project, 2025), fixing the number of directions to  $M = 100$  and tuning the kernel bandwidth over

$$\sigma \in \{10^{-5}, 10^{-4}, 10^{-3}, 10^{-2}, 10^{-1}, 1, 10\}.$$

## 11.1 Results

The supervised results in Table 5 show that PSph remains highly competitive across a broad range of tasks. Relative to the weighted construction PSph\* from Pegoraro (2026), performance is mostly consistent and in several datasets slightly improved. In particular, PSph attains the best mean on “Tecator”, “Growth”, “POWER”, and “McGill 3D Shapes”, and remains within overlapping confidence intervals of the best method on several others.

The differences between PSph and PSph\* are dataset-dependent. PSph improves markedly on “McGill 3D Shapes”, and also slightly on “Tecator”, “Growth”, “ENZYMES JACC”, and “POWER”. On the other hand, PSph\* remains stronger on “Human Poses”, and has a mild advantage on “DYN SYS”, “NOx”, and “SHREC14”. A plausible explanation for the gap on “Human Poses” is the very small sample size: in such regimes, explicit reweighting may act as a useful denoising bias before the downstream learning stage. This does not preclude combining reweighted diagrams with the new PSph representation; it only means that such a choice is no longer built into the representation itself.

PI are competitive on several datasets, including “Eyeglasses”, “DYN SYS”, “SHREC14”, and “McGill 3D Shapes”, but are less uniform than PSph-type summaries.

More broadly, the results confirm the main supervised finding already observed in Pegoraro (2026): PSph-type representations are consistently among the strongest performers across tasks. Persistence splines also perform very well in most supervised settings, whereas PersLay was likely penalized by the relatively small sample sizes of many benchmarks. Finally, none of the considered methods is uniformly poor, which reinforces the broader message of the paper: different summaries encode different geometric biases, and their effectiveness depends on the regime in which they are deployed.

## 12. Discussion

In this paper we introduced a refined definition of persistence spheres for integrable measures on the upper half-plane, proved stability with respect to  $\text{POT}_1$ , established continuity of the inverse on the image, and showed how these results extend naturally to a Hilbert-space setting relevant for applications. Conceptually, the key novelty is that the representation incorporates the deletion-to-diagonal mechanism of partial optimal transport directly through signed diagonal augmentation, rather than through ad hoc persistence-dependent reweighting. Empirically, the revised construction also leads to improved performance across the supervised benchmarks considered here.

These results suggest several directions for further work. At a conceptual level, the signed diagonal augmentation used here appears relevant beyond persistence spheres themselves. As discussed in Section 8.1, it provides a general way of reconciling linear summaries of persistence diagrams with the deletion-to-diagonal mechanism of  $\text{POT}_1$ , without imposing ad hoc vanishing weights near the diagonal. A natural question is therefore to understand how far this principle extends: for which classes of integral summaries, kernel embeddings, or smoothed diagram representations can augmentation yield not only stability, but also some form of inverse continuity or local metric faithfulness? In particular, it would be interesting to identify feature families rich enough to replicate, beyond the ReLU ridge setting considered here, the duality-and-approximation mechanism underlying the local inverse bounds of Theorem 3.

A second direction concerns statistical modeling directly on persistence-valued outputs. For instance, one may consider a parametric or nonparametric family of predictors  $h_\theta(x)$  taking values in a class of persistence measures, and estimate  $\theta$  by minimizing an empirical risk of the form

$$\frac{1}{n} \sum_{i=1}^n \ell(S(h_\theta(x_i)), S(\mu_i)),$$

where  $\mu_i$  are observed persistence measures and  $\ell$  is an  $L^2(\mathbb{S}^2)$ , uniform, or kernel-induced discrepancy. Because the representation is stable and bi-continuous on suitable classes, such procedures would allow one to optimize in a linear/Hilbert space while still controlling the induced error in  $\text{POT}_1$  on the underlying persistence objects.

A third direction concerns inversion. Given a function  $f \in C(\mathbb{S}^2)$ , for instance produced by a regression model or by averaging in sphere space, can one recover a persistence measure  $\hat{\mu}$  such that  $S(\hat{\mu}) \approx f$ ? This matters mainly for interpretation: passing back from a learned or averaged sphere representation to a diagram would allow one to read the result again in terms of persistence pairs rather than only as a function on  $\mathbb{S}^2$ . Even in the discrete case this raises nontrivial questions, including uniqueness, stability under approximation error, and effective reconstruction from finitely sampled values of  $f$ .

A natural first approach would be to optimize over discrete candidate measures

$$\hat{\mu} = \sum_{j=1}^m w_j \delta_{p_j},$$

and fit the locations  $p_j$  and weights  $w_j$  so that  $S(\hat{\mu})$  matches the observed function. By definition,

$$S(\hat{\mu})(v) = \sum_{j=1}^m w_j \left[ \text{ReLU}(\langle v, (1, p_j) \rangle) - \text{ReLU}(\langle v, (1, \pi_{\Delta}(p_j)) \rangle) \right],$$

so the inversion problem can be viewed as training a shallow ReLU model with a highly structured architecture, whose parameters are constrained by the geometry of persistence diagrams. This suggests exploiting the large body of optimization methods and software developed for neural networks. In this way, inversion would provide not only a computational tool, but also a concrete mechanism for translating learned or averaged sphere representations back into diagrams.

More broadly, the present work points to a larger problem in topological machine learning: understanding which linearizations of persistence are merely stable, which are geometrically faithful, and which structural modifications, such as diagonal augmentation, can help bridge the gap between the two.

## The Use of Large Language Models

Large Language Models were occasionally employed to refine and polish the writing and doublecheck some calculations.

## Code

At the time of submission, the code associated with this work is not yet ready to be released in the form of a public GitHub repository or a Python package. However, the current implementation is available upon request to the author.

## Acknowledgments

We thank Nicolas Chenavier, Christophe Biscio, and Nicola Rares Franco for the helpful discussions.

## References

- Henry Adams, Tegan Emerson, Michael Kirby, Rachel Neville, Chris Peterson, Patrick Shipman, Sofya Chepushtanova, Eric Hanson, Francis Motta, and Lori Ziegelmeier. Persistence images: A stable vector representation of persistent homology. *Journal of Machine Learning Research*, 18(8):1–35, 2017.
- Aras Asaad, Dashti Ali, Taban Majeed, and Rasber Rashid. Persistent homology for breast tumor classification using mammogram scans. *Mathematics*, 10(21):4039, 2022.
- Cinzia Bandiziol and Stefano De Marchi. Persistence symmetric kernels for classification: A comparative study. *Symmetry*, 16(9):1236, 2024.
- David Bate and Ana Lucía García Pulido. Bi-lipschitz embeddings of the space of unordered  $m$ -tuples with a partial transportation metric. *Mathematische Annalen*, 390(2):3109–3131, 2024.
- Jöran Bergh and Jörgen Löfström. *Interpolation spaces: an introduction*, volume 223. Springer Science & Business Media, 2012.
- Christophe AN Biscio and Jesper Møller. The accumulated persistence function, a new useful functional summary statistic for topological data analysis, with a view to brain artery trees and spatial point process applications. *Journal of Computational and Graphical Statistics*, 28(3):671–681, 2019.
- Peter Bubenik. Statistical topological data analysis using persistence landscapes. *Journal of Machine Learning Research*, 16:77–102, 2015.
- Mathieu Carrière and Ulrich Bauer. On the metric distortion of embedding persistence diagrams into separable hilbert spaces. In *35th International Symposium on Computational Geometry (SoCG 2019)*, pages 21–1. Schloss Dagstuhl–Leibniz-Zentrum für Informatik, 2019.
- Mathieu Carriere, Marco Cuturi, and Steve Oudot. Sliced wasserstein kernel for persistence diagrams. In *International conference on machine learning*, pages 664–673. PMLR, 2017.
- Barbara Di Fabio and Massimo Ferri. Comparing persistence diagrams through complex vectors. In *International conference on image analysis and processing*, pages 294–305. Springer, 2015.
- Peter J. Diggle. *Statistical Analysis of Spatial and Spatio-Temporal Point Patterns*. Chapman & Hall/CRC, 3 edition, 2013. doi: 10.1201/b15326.
- Vincent Divol and Théo Lacombe. Understanding the topology and the geometry of the space of persistence diagrams via optimal partial transport. *Journal of Applied and Computational Topology*, 5:1–53, 2021.
- Zhetong Dong, Hongwei Lin, Chi Zhou, Ben Zhang, and Gengchen Li. Persistence b-spline grids: stable vector representation of persistence diagrams based on data fitting. *Machine Learning*, 113(3):1373–1420, 2024.
- James R Driscoll and Dennis M Healy. Computing fourier transforms and convolutions on the 2-sphere. *Advances in applied mathematics*, 15(2):202–250, 1994.

- Herbert Edelsbrunner and John L Harer. *Computational topology: an introduction*. American Mathematical Society, 2010.
- Lawrence C. Evans. *Partial Differential Equations*, volume 19 of *Graduate Studies in Mathematics*. American Mathematical Society, Providence, RI, 2 edition, 2010. ISBN 978-0-8218-4974-3.
- Vesna Gotovac Dogaš and Marcela Mandarić. Topological data analysis for random sets and its application in detecting outliers and goodness of fit testing. *Statistical Methods & Applications*, pages 1–45, 2025.
- František Hendrych and Stanislav Nagy. A note on the convergence of lift zonoids of measures. *Stat*, 11(1):e453, 2022.
- Janine B. Illian, Antti Penttinen, Helga Stoyan, and Dietrich Stoyan. *Statistical Analysis and Modelling of Spatial Point Patterns*. Statistics in Practice. John Wiley & Sons, 2008. doi: 10.1002/9780470725160.
- Sara Kališnik. Tropical coordinates on the space of persistence barcodes. *Foundations of Computational Mathematics*, 19(1):101–129, 2019.
- Olav Kallenberg. *Foundations of modern probability*. Springer, 1997.
- Gleb Koshevoy and Karl Mosler. Lift zonoids, random convex hulls and the variability of random vectors. *Bernoulli*, 4(3):377–399, 1998.
- Genki Kusano, Kenji Fukumizu, and Yasuaki Hiraoka. Kernel method for persistence diagrams via kernel embedding and weight factor. *Journal of Machine Learning Research*, 18(189):1–41, 2018.
- Tong Mao, Jonathan W Siegel, and Jinchao Xu. Approximation rates for shallow  $\text{relu}^k$  neural networks on sobolev spaces via the radon transform. *arXiv preprint arXiv:2408.10996*, 2024.
- Bertil Matérn. *Spatial Variation*. Statens Skogsforskningsinstitut, 1960.
- Bertil Matérn. *Spatial Variation*. Springer, 2 edition, 1986.
- Edward J. McShane. Extension of range of functions. *Bulletin of the American Mathematical Society*, 40:837–842, 1934.
- Yuriy Mileyko, Sayan Mukherjee, and John Harer. Probability measures on the space of persistence diagrams. *Inverse Problems*, 27(12):124007, 2011.
- Atish Mitra and Žiga Virk. The space of persistence diagrams on  $n$  points coarsely embeds into hilbert space. *Proceedings of the American Mathematical Society*, 149(6):2693–2703, 2021.
- Atish Mitra and Ziga Virk. Geometric embeddings of spaces of persistence diagrams with explicit distortions. *arXiv preprint arXiv:2401.05298*, 2024.
- Jesper Møller and Rasmus P. Waagepetersen. *Statistical Inference and Simulation for Spatial Point Processes*. Chapman & Hall/CRC, 2004. doi: 10.1201/9780203496930.

- Anthea Monod, Sara Kalisnik, Juan Ángel Patino-Galindo, and Lorin Crawford. Tropical sufficient statistics for persistent homology. *SIAM Journal on Applied Algebra and Geometry*, 3(2):337–371, 2019.
- Michael Moor, Max Horn, Bastian Rieck, and Karsten Borgwardt. Topological autoencoders. In *International conference on machine learning*, pages 7045–7054. PMLR, 2020.
- Claus Müller. *Spherical harmonics*, volume 17. Springer, 2006.
- Steve Y Oudot. *Persistence theory: from quiver representations to data analysis*, volume 209. American Mathematical Society Providence, 2015.
- Theodore Papamarkou, Tolga Birdal, Michael M Bronstein, Gunnar E Carlsson, Justin Curry, Yue Gao, Mustafa Hajij, Roland Kwitt, Pietro Lio, Paolo Di Lorenzo, et al. Position: Topological deep learning is the new frontier for relational learning. In *International Conference on Machine Learning*, pages 39529–39555. PMLR, 2024.
- F. Pedregosa, G. Varoquaux, A. Gramfort, V. Michel, B. Thirion, O. Grisel, M. Blondel, P. Prettenhofer, R. Weiss, V. Dubourg, J. Vanderplas, A. Passos, D. Cournapeau, M. Brucher, M. Perrot, and E. Duchesnay. Scikit-learn: Machine learning in Python. *Journal of Machine Learning Research*, 12:2825–2830, 2011.
- Matteo Pegoraro. Persistence spheres: Bi-continuous representations of persistence diagrams. In *The Fourteenth International Conference on Learning Representations*, 2026. URL <https://openreview.net/forum?id=eITU6vjnIa>.
- The GUDHI Project. *GUDHI User and Reference Manual*. GUDHI Editorial Board, 3.11.0 edition, 2025. URL <https://gudhi.inria.fr/doc/3.11.0/>.
- James O. Ramsay and Bernard W. Silverman. *Functional Data Analysis*. Springer, New York, NY, USA, 2005.
- Jan Reininghaus, Stefan Huber, Ulrich Bauer, and Roland Kwitt. A stable multi-scale kernel for topological machine learning. In *Proceedings of the IEEE conference on computer vision and pattern recognition*, pages 4741–4748, 2015.
- R Tyrrell Rockafellar. *Convex Analysis*, volume 28. Princeton University Press, 1997.
- Gabriella Salinetti and Roger J.-B. Wets. On the convergence of sequences of convex sets in finite dimensions. *SIAM Review*, 21(1):18–33, 1979.
- Nathaniel Saul and Chris Tralie. Scikit-tda: Topological data analysis for python, 2019. URL <https://doi.org/10.5281/zenodo.2533369>.
- Jonathan W Siegel. Optimal approximation of zonoids and uniform approximation by shallow neural networks. *Constructive Approximation*, pages 1–29, 2025.
- Primoz Skraba and Katharine Turner. Wasserstein stability for persistence diagrams. *arXiv preprint arXiv:2006.16824*, 2020.
- M. Thomas. A generalization of poisson’s binomial limit for use in ecology. *Biometrika*, 36(1/2):18–25, 1949.
- Jeremy Wayland, Corinna Coupette, and Bastian Rieck. Mapping the multiverse of latent representations. In *International Conference on Machine Learning*. PMLR, 2024.

Mark A Wicczorek and Matthias Meschede. Shtools: Tools for working with spherical harmonics. *Geochemistry, Geophysics, Geosystems*, 19(8):2574–2592, 2018.

Weichen Wu, Jisu Kim, and Alessandro Rinaldo. On the estimation of persistence intensity functions and linear representations of persistence diagrams. In *International Conference on Artificial Intelligence and Statistics*, pages 3610–3618. PMLR, 2024.